EUROPEAN ORGANISATION FOR NUCLEAR RESEARCH (CERN)

Submitted to: JHEP

CERN-EP-2023-252
8th December 2023

Inclusive and differential cross-section measurements of $t\bar{t}Z$ production in pp collisions at $\sqrt{s} = 13$ TeV with the ATLAS detector, including EFT and spin-correlation interpretations

The ATLAS Collaboration

Measurements of both the inclusive and differential production cross sections of a top-quark–top-antiquark pair in association with a Z boson ($t\bar{t}Z$) are presented. Final states with two, three or four isolated leptons (electrons or muons) are targeted. The measurements use the data recorded by the ATLAS detector in pp collisions at $\sqrt{s} = 13$ TeV at the Large Hadron Collider during the years 2015–2018, corresponding to an integrated luminosity of 140 fb^{-1}. The inclusive cross section is measured to be $\sigma_{t\bar{t}Z} = 0.86 \pm 0.04$ (stat.) ± 0.04 (syst.) pb and found to be in agreement with the most advanced Standard Model predictions. The differential measurements are presented as a function of a number of observables that probe the kinematics of the $t\bar{t}Z$ system. Both the absolute and normalised differential cross-section measurements are performed at particle level and parton level for specific fiducial volumes, and are compared with NLO+NNLL theoretical predictions. The results are interpreted in the framework of Standard Model effective field theory and used to set limits on a large number of dimension-6 operators involving the top quark. The first measurement of spin correlations in $t\bar{t}Z$ events is presented: the results are in agreement with the Standard Model expectations, and the null hypothesis of no spin correlations is disfavoured with a significance of 1.8 standard deviations.

Contents

1 Introduction

The production of a top-quark–top-antiquark pair ($t\bar{t}$) in association with a Z boson is, according to the Standard Model (SM), a rare process in proton–proton (pp) collisions at the LHC and a source of various

multilepton final states. Given its high mass of approximately 173 GeV [1], and thus its large Yukawa coupling to the Higgs boson, the top quark plays a special role in electroweak (EW) physics. The coupling of the top quark to the Z boson is not yet well constrained by available data and its value can be significantly altered by 'beyond the Standard Model' (BSM) physics processes [2–7]. Precise measurements of the inclusive and differential cross sections of $t\bar{t}$ production in association with a Z boson, denoted by $t\bar{t}Z$, are thus of particular interest. Furthermore, the $t\bar{t}Z$ process is an irreducible background in other rare-top analyses, such as in four-top production [8, 9], as well as in several searches for BSM phenomena, such as in supersymmetric models [10–13]. Also, measurements of important SM processes, such as $t\bar{t}$ production in association with a Higgs boson [14–16] or single top-quark production in association with a Z boson [17, 18] are affected by $t\bar{t}Z$ background.

The most accurate theoretical prediction of the $t\bar{t}Z$ cross section is at full next-to-leading order (NLO) [19, 20], including EW corrections. Recently, these corrections were supplemented with a resummation of soft gluon corrections carried out at next-to-next-to-leading-logarithm (NNLL) accuracy and matched to the existing NLO results (NLO+NNLL), as reported in Ref. [21]. The predicted value at $\sqrt{s} = 13$ TeV [19] is:

$$\sigma_{t\bar{t}Z} = 0.863\,^{+0.073}_{-0.085}\,(\text{scale}) \pm 0.028\,(\text{PDF} \oplus \alpha_{\text{s}})\,\text{pb}.$$

Predictions of $t\bar{t}Z$ differential cross sections at NLO+NNLL accuracy, including EW corrections, were calculated in Ref. [22] and include those as functions of the rapidity of the top quark, the transverse momenta p_{T} of the top (anti-top) quark and the Z boson, and the invariant masses of the $t\bar{t}$ and $t\bar{t}Z$ systems.

The first differential cross-section measurement in $t\bar{t}Z$ production at the LHC was performed by the CMS Collaboration, using its 2016–2017 dataset from 13 TeV pp collisions, which corresponds to 77.5 fb^{-1}. The cross section was measured as a function of two variables in final states with three or four leptons [23]. Both the absolute and normalised differential cross sections were presented and compared with NLO+NNLL theoretical predictions. In addition, an inclusive cross-section measurement was performed, yielding $\sigma_{t\bar{t}Z} = 0.95 \pm 0.05\,(\text{stat.}) \pm 0.06\,(\text{syst.})$ pb.

In Ref. [24], the ATLAS Collaboration reported the first measurements of $t\bar{t}Z$ differential cross sections using its full dataset from Run 2 of the LHC. The inclusive cross section was also extracted in the three- and four-lepton channels and measured to be $\sigma_{t\bar{t}Z} = 0.99 \pm 0.05\,(\text{stat.}) \pm 0.08\,(\text{syst.})$ pb. The results from the ATLAS and CMS collaborations are compatible with the SM prediction [21], and with each other.

This paper presents an extended and refined measurement of the $t\bar{t}Z$ cross section in the multilepton final states, using the full dataset collected by the ATLAS experiment during Run 2 with the LHC. An additional final state is considered, targeting the all-hadronic decay of the $t\bar{t}$ system. The precision of the cross-section measurements is enhanced by making use of improved calibrations of physics objects and the total integrated luminosity, together with reduced experimental uncertainties, while the estimation of theoretical and modelling uncertainties benefits from recent measurements of key background processes and from more accurate Monte Carlo event generators and fixed-order phenomenological calculations. The cross section for $t\bar{t}Z$ production is extracted by performing a profile-likelihood fit simultaneously in the targeted analysis regions, with the signal normalisation as the parameter of interest. A similar profile-likelihood approach is employed to unfold the data to particle level and parton level, measuring absolute and normalised differential cross sections. The improved treatment of background effects, more detailed models of systematic uncertainties, and unfolding several detector-level selections simultaneously to the same fiducial volume provide a result that is more precise and robust than the one presented in Ref. [24]. The extracted inclusive $t\bar{t}Z$ cross sections and selected normalised differential kinematic

distributions at particle level and parton level are then used to constrain the dimension-6 effective field theory (EFT) operators relevant to the t–Z interaction in the context of the SM effective field theory (SMEFT) [25, 26]. A further interpretation of the experimental results is given in terms of coefficients of the spin density matrix, never before measured for the $t\bar{t}Z$ process [27].

2 ATLAS detector

The ATLAS detector [28] at the LHC covers nearly the entire solid angle around the collision point.[1] It consists of an inner tracking detector surrounded by a thin superconducting solenoid, electromagnetic and hadron calorimeters, and a muon spectrometer incorporating three large superconducting air-core toroidal magnets.

The inner-detector system (ID) is immersed in a 2 T axial magnetic field and provides charged-particle tracking in the range $|\eta| < 2.5$. The high-granularity silicon pixel detector covers the vertex region and typically provides four measurements per track, the first hit normally being in the insertable B-layer installed before Run 2 [29, 30]. It is followed by the silicon microstrip tracker, which usually provides eight measurements per track. These silicon detectors are complemented by the transition radiation tracker (TRT), which enables radially extended track reconstruction up to $|\eta| = 2.0$. The TRT also provides electron identification information based on the fraction of hits (typically 30 in total) above a higher energy-deposit threshold corresponding to transition radiation.

The calorimeter system covers the pseudorapidity range $|\eta| < 4.9$. Within the region $|\eta| < 3.2$, electromagnetic calorimetry is provided by barrel and endcap high-granularity lead/liquid-argon (LAr) calorimeters, with an additional thin LAr presampler covering $|\eta| < 1.8$ to correct for energy loss in material upstream of the calorimeters. Hadron calorimetry is provided by the steel/scintillator-tile calorimeter, segmented into three barrel structures within $|\eta| < 1.7$, and two copper/LAr hadron endcap calorimeters. The solid angle coverage is completed with forward copper/LAr and tungsten/LAr calorimeter modules optimised for electromagnetic and hadronic energy measurements respectively.

The muon spectrometer (MS) comprises separate trigger and high-precision tracking chambers measuring the deflection of muons in a magnetic field generated by the superconducting air-core toroidal magnets. The field integral of the toroids ranges between 2.0 and 6.0 Tm across most of the detector. Three layers of precision chambers, each consisting of layers of monitored drift tubes, cover the region $|\eta| < 2.7$, complemented by cathode-strip chambers in the forward region, where the background is highest. The muon trigger system covers the range $|\eta| < 2.4$ with resistive-plate chambers in the barrel, and thin-gap chambers in the endcap regions.

Interesting events are selected by the first-level trigger system implemented in custom hardware, followed by selections made by algorithms implemented in software in the high-level trigger [31]. The first-level trigger accepts events from the 40 MHz bunch crossings at a rate below 100 kHz, which the high-level trigger reduces in order to record events to disk at about 1 kHz.

[1] ATLAS uses a right-handed coordinate system with its origin at the nominal interaction point (IP) in the centre of the detector and the z-axis along the beam pipe. The x-axis points from the IP to the centre of the LHC ring, and the y-axis points upwards. Cylindrical coordinates (r, ϕ) are used in the transverse plane, ϕ being the azimuthal angle around the z-axis. The pseudorapidity is defined in terms of the polar angle θ as $\eta = -\ln\tan(\theta/2)$. Angular distance is measured in units of $\Delta R \equiv \sqrt{(\Delta\eta)^2 + (\Delta\phi)^2}$.

An extensive software suite [32] is used in data simulation, in the reconstruction and analysis of real and simulated data, in detector operations, and in the trigger and data acquisition systems of the experiment.

3 Data and simulated event samples

This analysis uses the full Run 2 dataset collected by ATLAS in 13 TeV pp collisions during 2015–2018 and corresponding to an integrated luminosity of 140 fb^{-1} [33]. Only events recorded when LHC beams were stable and all ATLAS detector systems were operational are selected. The uncertainty in the total integrated luminosity is 0.83% [33], obtained using the LUCID-2 detector [34] for the primary luminosity measurements, complemented by measurements using the inner detector and calorimeters. The average number of interactions per bunch crossing ranged from 0.5 to around 80, with a mean of 33.7.

The data were collected using a combination of single-electron and single-muon triggers, with requirements on the identification, isolation, and p_{T} of the leptons to maintain high efficiency across the full momentum range while controlling the trigger rates [31, 35, 36]. For electrons the trigger thresholds were p_{T} = 26, 60 and 140 GeV, whereas for muons the thresholds were p_{T} = 26 and 50 GeV.[2] Isolation requirements were applied to the triggers with the lowest p_{T} thresholds of 26 GeV for both electrons and muons [37–39].

Simulated Monte Carlo (MC) samples are used to model the signal and the prompt SM background. The effect of multiple interactions in the same and neighbouring bunch crossings (pile-up) was modelled by overlaying each simulated hard-scattering event with inelastic pp events generated with Pythia 8.186 [40] using the NNPDF2.3lo set of parton distribution functions (PDF) [41] and the A3 set of tuned parameters [42]. Separate MC production campaigns were used to model the different pile-up distributions observed in data during 2015/16, 2017 and 2018. The simulated samples were reweighted to reproduce the observed distribution of the average number of collisions per bunch crossing in each data-taking period.

The simulation of detector effects was performed with either a full ATLAS detector simulation [43] based on the Geant4 [44] framework or a fast simulation (AtlFast II) using a parameterisation of the performance of the electromagnetic and hadronic calorimeters and Geant4 for the other detector components [45, 46]. The full simulation was used for most processes, while the fast simulation was used only for the nominal prediction of the $t\bar{t}H$ process and alternative modelling samples for various other processes.

The associated production of $t\bar{t}$ with a leptonically decaying Z boson was modelled using the MadGraph5_aMC@NLO 2.8.1 [47] generator, which provided matrix elements at NLO in the strong coupling constant α_{s} with the NNPDF3.0nlo [48] PDF set. The $\gamma^* \to \ell^+\ell^-$ contribution and Z/γ^* interference are taken into account, down to 5 GeV in dilepton invariant mass. The functional form of the renormalisation and factorisation scales (μ_{r}, μ_{f}) was set to the default scale $0.5 \times \sum_i \sqrt{m_i^2 + p_{\mathrm{T},i}^2}$, where the sum runs over all the particles generated from the matrix element calculation. Top quarks were decayed at leading order (LO), using MadSpin [49, 50] to preserve all spin correlations. The top-quark mass was set to 172.5 GeV in all MC samples. The events were interfaced with Pythia 8.244 [51] for the simulation of the parton shower, fragmentation, hadronisation, and underlying event, using the A14 set of tuned parameters[3] [52] and the NNPDF2.3lo PDF set. The decays of bottom and charm hadrons were simulated using the EvtGen 1.7.0 program [53].

[2] Lower p_{T} thresholds of 24 GeV and 120 GeV for electrons and 20 GeV for muons were applied for 2015 data.

[3] Tuning refers to the process of optimising the parameters of the MC to produce a reasonable description of measured observables.

To estimate theoretical uncertainties in the signal prediction, several alternative $t\bar{t}Z$ MC samples are considered. These include a sample generated with the same MadGraph5_aMC@NLO version as the nominal sample, but interfaced to Herwig 7.2.1 [54, 55] for the simulation of the parton shower (using the default angle-ordered shower model). Two additional samples with the same settings as the nominal $t\bar{t}Z$ sample, except for upward and downward variations of the Var3c parameter in the A14 tune, are used to evaluate uncertainties associated with the modelling of initial-state radiation (ISR), following an approach similar to the one described in Ref. [56]. The Var3c variation corresponds to a variation of α_s for ISR in the A14 tune.

Alternative samples generated with Sherpa are used for comparisons with the unfolded differential distributions. A $t\bar{t}Z$ sample was produced with the Sherpa 2.2.1 [57] generator at NLO accuracy. Another sample was produced with a newer version of the same generator, Sherpa 2.2.11, together with the MEPS@NLO matching algorithm [58–60], which performed the multi-leg merging of up to three additional partons with the parton shower at LO, with a merging scale of 30 GeV. In both cases, a dynamic renormalisation scale defined similarly to that of the nominal $t\bar{t}Z$ samples was used. These samples also include off-shell effects down to 5 GeV in the invariant mass of the lepton pair. The default Sherpa parton shower was used along with the NNPDF3.0nnlo PDF set.

Events featuring the production of a $t\bar{t}$ pair in association with a SM Higgs boson with a mass of 125 GeV ($t\bar{t}H$) were generated using NLO matrix elements in MadGraph5_aMC@NLO 2.6.0 with the NNPDF3.0nlo PDF set. These events were showered with Pythia 8.230 using the A14 tune.

For $t\bar{t}$ production with a W boson ($t\bar{t}W$), the Sherpa 2.2.10 generator and default parton shower were used at NLO accuracy in QCD, with MEPS@NLO performing multi-leg merging of up to one additional parton at NLO and up to two additional partons at LO, with a merging scale of 30 GeV. Additionally, a LO QCD sample also generated with Sherpa 2.2.10 but for the $t\bar{t}Wj$ final state is used to model additional electroweak corrections to $t\bar{t}W$ production. In both $t\bar{t}W$ samples, the NNPDF3.0nnlo PDF set was used.

The production of single top quarks in association with a Z boson (tZq) was modelled with the MadGraph5_aMC@NLO 2.9.5 generator at NLO, while their production in association with a W boson and Z boson (tWZ) used MadGraph5_aMC@NLO 2.2.2 at NLO, both with the NNPDF3.0nlo PDF set. The tZq events were interfaced with Pythia 8.245, and the tWZ events with Pythia 8.212, using the A14 tune and the NNPDF2.3lo PDF set. The tZq sample was simulated in the four-flavour scheme (thus including an additional b-quark in the final state) and normalised to a cross section obtained in the five-flavour scheme. It also includes off-shell effects down to 5 GeV in dilepton invariant mass.

Uncertainties in modelling the tZq process are estimated similarly to the case of $t\bar{t}Z$: the Var3c parameter of the A14 tune is varied upwards and downwards, and a separate sample is considered in which the generated events are interfaced to the Herwig 7.2.1 parton shower algorithm instead of Pythia 8.245. At NLO in QCD, the Feynman diagrams of the tWZ process include contributions such as $gg \to tWZb$, which may also feature a second intermediate top resonance and thus interfere with the signal $t\bar{t}Z$ process. The nominal tWZ sample follows the 'diagram removal 1' (DR1) scheme described in Ref. [61] and ignores any Feynman diagrams containing two resonant top quarks. An alternative sample was generated within the DR2 scheme, which additionally considers the interference terms (at the level of squared amplitudes) between single- and double-resonant $t\bar{t}$ production. This alternative sample is used to set an uncertainty on the modelling of the tWZ process, as described in Section 7.3.

The production of $t\bar{t}$ background events was modelled with the Powheg Box v2 generator [62] at NLO

with the NNPDF3.0NLO PDF set and the damping factor h_{damp}[4] set to 1.5 times the top-quark mass. The events were interfaced with PYTHIA 8.230, which used the A14 tune and NNPDF2.3LO PDF set. The top-quark decays were modelled at LO, while decays of bottom and charm hadrons were simulated with EVTGEN 1.2.0.

Several alternative samples are used to evaluate theoretical uncertainties in the modelling of the $t\bar{t}$ events. These include a separate sample from the same POWHEG generator version as above but where the h_{damp} parameter was increased to 3.0 times the top-quark mass, a sample where the events generated in POWHEG were interfaced to HERWIG 7.0.4 for parton showering, and a sample from a different matrix element generator, MADGRAPH5_AMC@NLO 2.3.3, interfaced with PYTHIA 8.230.

Diboson processes producing either three charged leptons and one neutrino or four charged leptons (WZ+jets or ZZ+jets, respectively) were simulated using the SHERPA 2.2.2 generator. In this set-up, multiple matrix elements were matched and merged with the SHERPA parton shower based on the Catani–Seymour dipole factorisation scheme [63, 64] using the MEPS@NLO prescription [58–60, 65]. Virtual QCD corrections for NLO-accurate matrix elements were provided by the OPENLOOPS library [66, 67]. Samples were generated using the NNPDF3.0NNLO PDF set, along with the dedicated set of tuned parton shower parameters developed by the SHERPA authors. The WZ/ZZ+jets events with no or one additional parton were simulated at NLO, whereas events with two or three additional partons were simulated at LO precision.

The production of events with a W or Z boson and multiple jets (V+jets) was simulated with the SHERPA 2.2.1 generator using NLO-accurate matrix elements for up to two jets, and LO-accurate ones for up to four jets, calculated with the Comix [63] and OPENLOOPS [66–68] libraries. They were matched with the SHERPA parton shower using the MEPS@NLO prescription. The NNPDF3.0NNLO set of PDFs was used and the samples are normalised to next-to-next-to-leading-order (NNLO) predictions [69].

Events from both the diboson and V+jets processes are separated into light-, b- and c-flavour components, depending on whether the MC event record has a b- or c-hadron in any of the selected jets.

MC samples featuring Higgs boson production in association with a W or Z boson were generated with PYTHIA 8.186 using the A14 tune and the NNPDF2.3LO PDF set. Triple top-quark production ($tt\bar{t}$) and the production of a $t\bar{t}$ pair with two W bosons ($t\bar{t}WW$) were simulated at LO using MADGRAPH 2.2.2 interfaced to PYTHIA 8.186 with the A14 tune and the NNPDF2.3LO PDF set. Four top-quark production ($t\bar{t}t\bar{t}$) was simulated at NLO using MADGRAPH5_AMC@NLO 2.3.3 interfaced to PYTHIA 8.230 with the A14 tune and the NNPDF3.1NLO PDF set; an alternative sample used the HERWIG 7.04 parton shower instead. Processes with three heavy gauge bosons (WWW, WWZ, WZZ and ZZZ) yielding up to six final-state leptons were simulated with SHERPA 2.2.2 and the NNPDF3.0NLO PDF set. Final states with no additional partons were calculated at NLO, whereas final states with one, two or three additional partons were calculated at LO.

The versions of the generator, parton shower and PDF used for each of the nominal MC samples, as well as the reference cross sections used to normalise the samples, are given in Table 1.

For the SMEFT interpretation, additional MC samples were produced at LO in QCD for the $t\bar{t}Z$ and tZq processes, using the MADGRAPH 2.9.3 generator and PYTHIA 8.245 parton shower (with the default A14 tune settings). They rely on the SMEFTsim 3.0 [26] UFO model [80] implemented in MADGRAPH with FeynRules [81], in the m_W electroweak input scheme [82] with the top-flavour restrictions (in the five-flavour scheme). The nominal events were generated according to the SM, and the MADGRAPH reweighting module was used to compute a large number of alternative event weights corresponding to the

[4] The h_{damp} parameter is a resummation damping factor and one of the parameters that controls the matching of POWHEG matrix elements to the parton shower and thus effectively regulates the high-p_{T} radiation against which the $t\bar{t}$ system recoils.

Table 1: Versions of the generator, parton shower and PDF used for the nominal MC samples and reference cross sections used in the analysis. Whenever a reference is not indicated, the cross section is taken directly from the MC set-up described in the text.

Process	Generator	Parton shower	PDF	Reference cross section [fb]
$t\bar{t}Z$	MadGraph5_aMC@NLO 2.8.1	Pythia 8.244	NNPDF3.0nlo	876 [19, 56]
$t\bar{t}H$	MadGraph5_aMC@NLO 2.6.0	Pythia 8.230	NNPDF3.0nlo	507 [19]
$t\bar{t}W/t\bar{t}Wj$	Sherpa 2.2.10	Sherpa 2.2.10	NNPDF3.0nnlo	722 [70]
tZq	MadGraph5_aMC@NLO 2.9.5	Pythia 8.245	NNPDF3.0nlo	38.7
tWZ	MadGraph5_aMC@NLO 2.2.2	Pythia 8.212	NNPDF2.3lo	16.1
$t\bar{t}$	Powheg Box v2	Pythia 8.230	NNPDF3.0nlo	87 700 [71]
WZ+jets/ZZ+jets	Sherpa 2.2.2	Sherpa 2.2.2	NNPDF3.0nnlo	7 330
V+jets	Sherpa 2.2.1	Sherpa 2.2.1	NNPDF3.0nnlo	$6\,250 \times 10^3$ [69]
$t\bar{t}t\bar{t}$	MadGraph5_aMC@NLO 2.3.3	Pythia 8.230	NNPDF3.1nlo	12.0 [72]
$tt\bar{t}$	MadGraph 2.2.2	Pythia 8.186	NNPDF2.3lo	1.64
VH	Pythia 8.186	Pythia 8.186	NNPDF2.3lo	2 250 [73–79]
VVV	Sherpa 2.2.2	Sherpa 2.2.2	NNPDF3.0nlo	13.7

inclusion of dimension-6 EFT vertices and propagators in the production Feynman diagrams. These internal weights can then be used to extract the dependence of various observables (including the cross section) on more than 30 different EFT operators related to $t\bar{t}$ production, the t–Z vertex and the off-shell $t\bar{t}\ell\ell$ vertex, as described in Section 11. Since the EFT couplings cannot run in MadGraph, the renormalisation and factorisation scales are kept fixed at $\mu = \sum_i m_i$ (where i runs over the massive final-state resonances). The EFT samples were passed through the fast detector simulation (using AtlFast II) and the events reconstructed in order to assess their impact on the unfolding (efficiency and acceptance corrections).

4 Object identification and event reconstruction

Electron candidates are reconstructed from clusters of energy deposits in the electromagnetic calorimeter that are matched to a track in the ID. They are required to satisfy $p_{\mathrm{T}} > 7$ GeV, $|\eta| < 2.47$ and a 'Medium' likelihood-based identification requirement [83, 84]. Electron candidates are excluded if their calorimeter clusters lie within the transition region between the barrel and endcaps of the electromagnetic calorimeter, $1.37 < |\eta| < 1.52$, to reduce the contribution from fake electrons. The track associated with the electron must pass the requirements $|z_0 \sin(\theta)| < 0.5$ mm and $|d_0|/\sigma(d_0) < 5$, where z_0 describes the longitudinal impact parameter relative to the reconstructed primary vertex,[5] d_0 is the transverse impact parameter relative to the beam axis, and $\sigma(d_0)$ is the uncertainty in d_0. Furthermore, a requirement on the electron isolation, corresponding to the PLVLoose isolation working point (WP) [14] is applied to identify 'signal' electrons; 'baseline' electrons have no isolation requirement.

Muon candidates are reconstructed from MS tracks matched to ID tracks in the pseudorapidity range of

[5] The primary vertex must have at least two associated tracks with $p_{\mathrm{T}} > 500$ MeV and is defined as the vertex with the highest scalar sum of the squared transverse momenta of such tracks.

$|\eta| < 2.5$. They must satisfy $p_{\mathrm{T}} > 7$ GeV along with the 'Medium' identification requirements defined in Refs. [85, 86]. The latter impose requirements on the number of hits in the different ID and MS subsystems and on the significance of the charge-to-momentum ratio q/p. In addition, the track associated with the muon candidate must have $|z_0 \sin(\theta)| < 0.5$ mm and $|d_0|/\sigma(d_0) < 3$. As is the case for electrons, the baseline muons have no isolation requirements, whereas the muons selected for the analysis must pass the PLVLoose isolation WP. The lepton trigger, reconstruction and selection efficiencies from simulation receive small corrections derived from measurements of $Z \to \ell\ell$ and $J/\psi \to \mu\mu$ events in the data [35, 36, 84, 86].

Jets are reconstructed using the anti-k_t jet algorithm [87] as implemented in the FastJet package [88], with the radius parameter R set to 0.4 and particle-flow objects [89] as input. The jets are calibrated by applying a jet energy scale derived from 13 TeV data and simulation [90]. The jets are kept only if they have $p_{\mathrm{T}} > 25$ GeV and are inside a pseudorapidity range of $|\eta| < 2.5$. The jet-vertex tagger (JVT) [91] algorithm is employed in order to mitigate pile-up effects in jets with $p_{\mathrm{T}} < 60$ GeV, applying the 'Tight' WP.

Jets containing a b-hadron, referred to as b-jets, are identified with the DL1r b-tagging algorithm [92, 93]. A WP corresponding to 85% efficiency[6] is used for most preselections in the analysis. Exclusive bins of b-tagging discriminant values corresponding to different b-jet identification efficiencies are also used, as pseudo-continuous b-tagging (PCBT). This allows different calibrated b-tagging WPs to be used in defining selections targeting specific signal or background processes, referred to as regions.

The missing transverse momentum is defined as the negative vector sum of the transverse momenta of all selected and calibrated physics objects. Low-momentum tracks from the primary vertex that are not associated with any of the reconstructed physics objects described previously are also included as a 'soft term' in the calculation [94]. The magnitude of the missing transverse momentum vector is denoted by $E_{\mathrm{T}}^{\mathrm{miss}}$.

Ambiguities can arise from the independent reconstruction of electron, muon and jet candidates in the detector. A sequential procedure (overlap removal) is applied to resolve these ambiguities and thus prevent double counting of physics objects. It is applied to signal electrons, muons, and jets as follows. If an electron candidate and a muon candidate share a track, the electron candidate is removed. The jet candidate closest to a remaining electron candidate is removed if they are less than a distance $\Delta R_{y,\phi} = \sqrt{(\Delta y)^2 + (\Delta\phi)^2} = 0.2$ apart, where y is the jet's rapidity. If the electron–jet separation is between 0.2 and 0.4, the electron candidate is removed. If the $\Delta R_{y,\phi}$ between any remaining jet and a muon candidate is less than 0.4, the muon candidate is removed if the jet has more than two associated tracks, otherwise the jet is discarded.

In the differential measurements of the $t\bar{t}Z$ cross section, two definitions of particles in the MC generator-level event record are considered: parton level and particle level. While the former leads to a very inclusive phase-space for ease of comparison with fixed-order matrix element calculations, the latter is used to build a fiducial volume much closer to that of the detector-level analysis.

Parton-level objects are obtained from the MC generation history of the $t\bar{t}Z$ system. The top (anti-top) quarks and Z bosons are selected as the last instances of these particles in this 'truth' record, after radiation but immediately before their $t \to Wb$ or $Z \to \ell\ell$ decay, respectively. The leptons originating from W and Z bosons are selected as the first instances, immediately following the decay of the parent boson.

[6] The b-tagging efficiency is determined with respect to generator-level b-jets with $p_{\mathrm{T}} > 20$ GeV and $|\eta| < 2.5$ in $t\bar{t}$ MC simulations.

Particle level refers to a collection of objects which are considered stable in the MC simulation ($\tau \geq 30\,\text{ps}$) but without any simulation of the interaction of these particles with the detector components or any additional pp interactions. Unlike for parton-level objects, the hadronisation of the quarks is included. Particle-level leptons are selected as leptons originating from the decay of a W or Z boson. The four-momentum of an electron or muon is summed with the four-momenta of all radiated photons within a cone of size $\Delta R = 0.1$ around its direction, excluding photons from hadron decays. The parents of the electrons or muons are required not to be a hadron or quark (u,d,s,c,b). The particle-level jets are reconstructed with the anti-k_t algorithm with a radius parameter of $R = 0.4$, using all stable particles except for the selected electrons, muons, and photons used in the definition of the selected leptons, and neutrinos originating from the Z boson or W bosons. A small-R jet is considered a b-jet if it is ghost-matched [92, 95] to a b-hadron with $p_{\text{T}} > 5$ GeV. The particle-level missing transverse momentum is defined as the vector sum of the transverse momenta of all neutrinos found in the simulation history of the event, excluding those originating from hadron decays.

5 Analysis strategy

The signal regions (SRs) used in this analysis are designed to offer the highest possible purity of $t\bar{t}Z$ events, as well as to provide yields sufficient for a differential measurement of the $t\bar{t}Z$ cross section. The analysis is performed in three orthogonal channels, distinguished by lepton multiplicity. A multivariate analysis (MVA) approach is employed in each channel to better discriminate between the signal and background processes. An improvement on the previous measurement [24], the MVA has the largest impact on the dilepton (2ℓ) and trilepton (3ℓ) channels that have large background contributions, whereas the tetralepton (4ℓ) channel only receives a modest enhancement due to its already excellent signal purity at the preselection level. The MVA input variables consist mostly of kinematic variables for individual objects such as jets and leptons, b-tagging information for jets, and kinematics of the reconstructed top quarks and Z boson. The exact list of the variables can be found in the Appendix, in Tables 22, 23 and 24.

Neural networks are used in the three channels, and these are trained using the Keras [96] backend of Tensorflow [97]. In all cases, the Adam optimiser is used for training. In the 3ℓ channel, the categorical cross-entropy loss is minimised. The networks in the 2ℓ and 4ℓ channels employ binary cross-entropy as the loss function. These networks cater to binary classification scenarios, albeit with varying objectives. To ensure optimal performance, the hyperparameters of all networks are tuned using a grid search, which systematically varies the number of layers, activation functions, and regularisation techniques such as batch normalisation and dropout. Additionally, K-folding techniques [98] are employed to enable comprehensive training and evaluation with the entire set of MC simulations. This approach ensures that the networks are trained and tested on statistically independent subsets of the MC simulations.

5.1 Dilepton signal regions

The dilepton channel targets $t\bar{t}Z$ events where the $t\bar{t}$ system decays hadronically, while an opposite-sign same-flavour (OSSF) pair of leptons originates from the Z boson. Events are required to have exactly one pair of OSSF leptons. The invariant mass of the lepton pair is required to be within 10 GeV of the Z-boson mass [99], with the two leptons required to have transverse momenta of at least 30 GeV and 15 GeV respectively.

The 2ℓOS channel generally suffers from a low signal-to-background ratio, with the $t\bar{t}$ and Z+jets processes (both characterised by the presence of two prompt[7] leptons) constituting major backgrounds. Three signal regions are defined, based on jet and b-tagged jet (at 77% b-tagging efficiency) multiplicities (N_{jets} and $N_{b\text{-tagged jets@77\%}}$ respectively). The splitting is motivated by the different background compositions and the fact that it is not possible to fully reconstruct the $t\bar{t}$ system in events with only five jets. SR-2ℓ-5j2b requires exactly five jets, of which at least two must be b-tagged; SR-2ℓ-6j2b SR provides its jet-inclusive complement (at least six jets). SR-2ℓ-6j1b, inclusive in jet multiplicity (at least six jets) but requiring exactly one b-tagged jet, targets events with the appropriate jet multiplicity for tree-level $t\bar{t}Z$ events but with one non-identified b-tagged jet. All dileptonic preselections and SR selections are summarised in Table 2.

To improve the discrimination between the $t\bar{t}$ and Z+jets background processes and the $t\bar{t}Z$ signal, one deep neural network (DNN) is trained for each signal region on events passing the corresponding selection. The categorisation of events into signal regions based on jet and b-tagged-jet multiplicities allows the DNNs to be tuned on different background compositions and signal-to-background ratios, enhancing the overall performance. This is particularly needed here, given the much larger background contributions than in the other two analysis channels. All DNNs are constructed as binary classification networks (with $t\bar{t}Z$ as signal and all other processes as background) and the distributions of the DNN outputs are used directly in the inclusive measurement and are not employed in the definition of the signal regions. Details of the variables used in the training of the DNN are given in Table 22 in the Appendix.

Table 2: Definition of the dilepton signal regions.

Variable	**Preselection**		
N_ℓ $(\ell = e, \mu)$	$= 2$		
	$= 1$ OSSF lepton pair with $\lvert m_{\ell\ell} - m_Z \rvert < 10$ GeV		
p_{T} (ℓ_1, ℓ_2)	$> 30,\ 15$ GeV		
	SR-2ℓ-5j2b	**SR-2ℓ-6j1b**	**SR-2ℓ-6j2b**
N_{jets} $(p_{\text{T}} > 25$ GeV)	$= 5$	≥ 6	≥ 6
$N_{b\text{-tagged jets@77\%}}$	≥ 2	$= 1$	≥ 2

5.2 Trilepton signal regions

A trilepton preselection is defined by requiring exactly three signal leptons, and their transverse momenta must be higher than 27, 20 and 15 GeV. Amongst these three leptons, the OSSF pair with invariant mass closest to the Z-boson mass is considered to originate from the Z-boson decay, and its invariant mass ($m_{\ell\ell}$) has to be within 10 GeV of the Z-boson mass. Furthermore, all OSSF lepton combinations are required to have $m_{\text{OSSF}} > 10$ GeV to remove contributions arising from low-mass resonances, which are not included in the simulation. At least three jets are required, of which at least one has to be b-tagged (with 85% tagging efficiency). All trileptonic preselections and SR selections are summarised in Table 3.

[7] The term 'prompt' refers to leptons which are directly produced by the hard-scatter process or by the decays of heavy resonances such as W, Z or Higgs bosons.

A 3-class DNN is trained to identify $t\bar{t}Z$, tZq and diboson events amongst those kept after the 3ℓ preselection is applied. Table 23 in the Appendix details the variables used in the DNN. The trilepton phase-space after preselection is partitioned into three signal regions labelled SR-3ℓ-ttZ, SR-3ℓ-tZq and SR-3ℓ-WZ, according to the largest output of the three decision nodes. These selections are summarised in Table 3. While the tZq and $WZ + b$ contributions are largest in SR-3ℓ-tZq and SR-3ℓ-WZ, respectively, these regions still contain a non-negligible number of $t\bar{t}Z$ signal events. The three SRs are mutually exclusive by construction and together fill the entire phase-space after preselection. A tighter b-tagging requirement (at least one b-tagged jet at 60% efficiency) is then additionally applied in SR-3ℓ-WZ to efficiently suppress the contributions from the lighter-flavour $WZ + l$[8] and $WZ + c$ backgrounds, retaining only the $WZ + b$ component since it is an important background in the other two SRs also.

Table 3: Definition of the trilepton signal regions.

Variable	**Preselection**		
N_ℓ $(\ell = e, \mu)$	$= 3$		
	≥ 1 OSSF lepton pair with $\lvert m_{\ell\ell} - m_Z \rvert < 10$ GeV		
	for all OSSF combinations: $m_{\text{OSSF}} > 10$ GeV		
p_{T} (ℓ_1, ℓ_2, ℓ_3)	$> 27,\ 20,\ 15$ GeV		
N_{jets} $(p_{\text{T}} > 25$ GeV$)$	≥ 3		
$N_{b\text{-tagged jets}}$	≥ 1@85%		
	SR-3ℓ-ttZ	**SR-3ℓ-tZq**	**SR-3ℓ-WZ**
DNN-tZq output	< 0.40	≥ 0.40	—
DNN-WZ output	< 0.22	< 0.22	≥ 0.22
$N_{b\text{-tagged jets}}$	—	—	≥ 1@60%

5.3 Tetralepton signal regions

The tetralepton channel is defined by the requiring exactly four leptons, of which at least one must have transverse momentum greater than 27 GeV and two must form an OSSF pair with invariant mass within 20 GeV of the Z-boson mass. The sum of the lepton charges is required to be zero. Low-mass dilepton resonances are removed by requiring the invariant mass of all OSSF pairs to be greater than 10 GeV. The OSSF pair with invariant mass closest to the Z-boson mass is taken to be the Z candidate; selected events can then be further categorised according to the flavour of the non-Z lepton pair, into a same-flavour (SF) or different-flavour (DF) signal region. As a result, the ZZ+jets background mostly populates the SF region. Additionally, at least two jets, including at least one b-tagged jet (with 85% tagging efficiency), are required. All tetraleptonic preselections and SR selections are summarised in Table 4.

To achieve better signal sensitivity, a DNN is trained in both signal regions to discriminate between the $t\bar{t}Z$ signal and the background processes, with the input variables listed in Table 24 of the Appendix. Events featuring two pairs of same-flavour leptons are particularly sensitive to contributions from the ZZ+jets

[8] In this context, we refer to the light-flavour quarks u, d, and s by the label l, not to be confused with the label ℓ reserved for leptons.

background process; they can be removed from the SR by applying a selection requirement on the DNN output. The SR definitions are summarised in Table 4.

Table 4: Definition of the tetralepton signal regions.

Variable	**Preselection**	
N_ℓ $(\ell = e, \mu)$	$= 4$	
	≥ 1 OSSF lepton pair with $\lvert m_{\ell\ell} - m_Z \rvert < 20$ GeV	
	for all OSSF combinations: $m_{\text{OSSF}} > 10$ GeV	
p_{T} $(\ell_1, \ell_2, \ell_3, \ell_4)$	$> 27,\ 7,\ 7,\ 7$ GeV	
The sum of lepton charges	$= 0$	
N_{jets} $(p_{\text{T}} > 25$ GeV)	≥ 2	
$N_{b\text{-tagged jets}}$	≥ 1@85%	
	SR-4ℓ-SF	**SR-4ℓ-DF**
$\ell\ell^{\text{non-}Z}$	e^+e^- or $\mu^+\mu^-$	$e^\pm\mu^\mp$
DNN output	≥ 0.4	—

5.4 Particle- & parton-level selections

The particle- and parton-level selections for the 3ℓ and 4ℓ channels used for the differential measurements are summarised in Table 5. The particle-level fiducial regions are constructed to closely follow the detector-level regions, using the particle-level objects defined in Section 4 and with at least one OSSF lepton pair within ±10 GeV of the Z-boson mass. The parton-level fiducial volumes are defined by the $t\bar{t}$ decays: semileptonic (e, μ+jets only) in the 3ℓ channel, and dileptonic ($e^+e^-, e^\pm\mu^\mp, \mu^+\mu^-$ only) in the 4ℓ channel. The Z boson is required to decay dileptonically via $Z \to e^+e^-, \mu^+\mu^-$. Events featuring τ-leptons which originate directly from either the Z boson or the W bosons from the $t\bar{t}$ system are removed from the parton-level fiducial volume and are not considered in the unfolding, regardless of their subsequent decay. The differential variables are reconstructed from the top quarks after final-state radiation, immediately prior to their decays. The invariant mass of the two leptons from the Z-boson decay is required to be within ±15 GeV of the Z-boson mass; this widening of the mass window at parton level diminishes the impact of reconstruction and acceptance efficiency uncertainties on the unfolding procedure.

5.5 Top-quark reconstruction

Several different approaches for the kinematic reconstruction of either the $t\bar{t}$ system or the single (anti-)top quarks are used in this measurement and described in the following, tailored to the characteristics of the various $t\bar{t}Z$ decay channels considered in this analysis. A brief summary for each channel is given in the following.

Table 5: Definition of the fiducial volumes at particle level and parton level. Leptons refer exclusively to electrons and muons; they are dressed with additional photons at particle level, but not at parton level.

Particle-level selection	
3ℓ channel	4ℓ channel
Exactly 3 leptons, with $p_{\mathrm{T}}(\ell_1, \ell_2, \ell_3) > 27, 20, 15$ GeV	Exactly four leptons, with $p_{\mathrm{T}}(\ell_1, \ell_2, \ell_3, \ell_4) > 27, 7, 7, 7$ GeV
The sum of charges is ± 1	The sum of charges is = 0
At least 3 jets, with $p_{\mathrm{T}} > 25$ GeV	At least 2 jets, with $p_{\mathrm{T}} > 25$ GeV
At least 1 b-jet (jet ghost-matched to a b-hadron)	
At least one OSSF lepton pair, with $\lvert m_{\ell\ell} - m_Z \rvert < 10$ GeV	
Parton-level selection	
3ℓ channel	4ℓ channel
$t\bar{t} \to e^{\pm}/\mu^{\pm}$ + jets	$t\bar{t} \to e^{\pm}\mu^{\mp}/e^{\pm}e^{\mp}/\mu^{\pm}\mu^{\mp}$
$Z \to e^{\pm}e^{\mp}/\mu^{\pm}\mu^{\mp}$	
$\lvert m_{\ell\ell} - m_Z \rvert < 15$ GeV	

5.5.1 2ℓOS reconstruction

In the 2ℓOS channel, two methods are employed to reconstruct the $t\bar{t}$ system. The outputs of both of these algorithms are used in the construction of variables that are subsequently used in the training of neural networks since they provide complementary information that can be used to discriminate between the signal and background processes.

The first method, referred to as the *multi-hypothesis hadronic top/W reconstruction method*, targets the fully hadronically decaying $t\bar{t}$ system associated with the signal process, taking into account several hypotheses for the numbers of available and missing top-quark final-state particles. At tree level, six jets from the fully hadronic decay of the $t\bar{t}$ system are part of the 2ℓOS $t\bar{t}Z$ signature; however, due to the jet energy resolution and coverage of the detector, some jets matched to a final-state quark may not be reconstructed. Five different scenarios[9] are considered for the reconstruction procedure, depending on the numbers of hadronically decaying W bosons and top quarks that can be reconstructed, each giving an output weight. For each hypothesis, all jets-to-quarks assignments are tested and the probability of the hypothesis and combination being correct is calculated from known distributions of two-jet or three-jet invariant mass originating from the W bosons or top quarks, respectively. The final weight for each hypothesis is the probability of the most likely jet permutation, and this permutation is considered correct for a given hypothesis.

An alternative approach attempts to reconstruct the all-hadronic $t\bar{t}$ system through the use of SPANet (Symmetry Preserving Attention Network), an attention-based neural network originally designed for the reconstruction of all-hadronic $t\bar{t}$ events [100]. The network was trained for the dilepton $t\bar{t}Z$ topology using both the nominal and alternative $t\bar{t}Z$ sample events, required to pass the 2ℓOS selection from Table 2 and have at least six jets (at least one b-tagged). One or both top quarks have to be correctly matched,

[9] Considered scenarios: jets from one W boson are present, jets from two W bosons are present, jets from one top quark are present, jets one top quark and one W boson are present, and jets both top quarks are present.

where correct jet assignments are found by matching detector-level objects to parton level. Inputs are the kinematic and b-tagging information of all jets present in the event, as well as the correct jet assignments. The network predicts the jet assignments for the top and anti-top quarks. It assigns them correctly in ≈56% of the events where jets from the top quarks are present. The transverse momentum of the reconstructed all-hadronic $t\bar{t}$ system, $p_{\mathrm{T}}^{t\bar{t}}$, is then used as an input to the MVA discriminant in the 2ℓOS channel.

5.5.2 3ℓ reconstruction

The full reconstruction of the $t\bar{t}$ system in 3ℓ events is performed by first reconstructing the leptonic-side top quark[10] and subsequently reconstructing the hadronic-side top quark. For the leptonic-side the $E_{\mathrm{T}}^{\mathrm{miss}}$ is attributed to the neutrino from the associated W-boson decay. The neutrino momentum in the z direction ($p_{\nu z}$) can be determined from a quadratic equation constrained by the SM W-boson mass, resulting in up to two distinct solutions, which are both considered. In the few cases where no real solution exists, the neutrino p_{T} is adjusted such that the quadratic determinant becomes zero and a single solution for $p_{\nu z}$ exists. Each W boson candidate is then paired with the nearest (in ΔR) b-tagged jet. The most likely top-quark candidate is determined from the $p(m_{b\ell\nu})$ probability density distribution obtained from MC $t\bar{t}Z$ simulations.

The hadronic-side reconstruction builds top-quark candidates from jet pairs compatible with a W boson, and a b-tagged jet. Since the b-tagged jet on the leptonic-side has already been determined, the remaining jet with the highest b-tagging score is assigned to the hadronic-side top quark. From all the other jets, the two most compatible with having originated from a W boson are determined via interpolation of m_{jj} with the reference distributions used in the multi-hypothesis reconstruction method.

The exact same top reconstruction algorithms are applied at particle level, using the two highest-p_{T} jets that were ghost-matched to b-hadrons to define the b-candidates.

5.5.3 4ℓ reconstruction

In this channel a full kinematic reconstruction of the $t\bar{t}Z$ system is performed employing the Two Neutrino Scanning Method (2νSM), improving on the previous analysis [24] where it was reconstructed in the transverse plane only. Values of the azimuthal angle and pseudorapidity of either neutrino are tested by systematically scanning the η–ϕ space and, with the set of the respective values at each point in the η–ϕ space of the two neutrinos, the $t\bar{t}$ signature is constructed from the information about the two leptons which are not associated with the Z-boson decay and the two jets which have the highest b-tagging score.

Kinematic constraints from reference distributions are used to create a single output weight, $w_{2\nu\mathrm{SM}}$, for each of the hypotheses and then the combination with the largest weight is selected as the reconstructed dileptonic $t\bar{t}$ system. This output weight shows high discrimination power between $t\bar{t}Z$ and dileptonic $t\bar{t}$ events, and therefore can be used as a discriminating variable for MVA training.

At particle level, a pseudo-top-quark reconstruction algorithm is employed. First, the two leading-p_{T} neutrinos (from the MC truth record) are matched to the two charged leptons left in the event after the Z boson candidate is determined. From the two possible lepton–neutrino pairings, the one that yields an invariant mass closest to the W-boson mass is retained. The two highest-p_{T} jets that are ghost-matched to

[10] The term leptonic-side top quark is taken to mean the top or anti-top quark from the $t\bar{t}$ pair for which the W-boson decays via $W \to \ell\nu$, and similarly $W \to q'\bar{q}$ for the term hadronic-side.

b-hadrons define the b-candidates; when only one such jet exists in the event, the second b-candidate is taken to be the leading-p_{T} jet amongst those left available. As before, both pairings of b- and W-candidates are considered, and the one that yields an invariant mass closest to the MC top-quark mass (172.5 GeV) is used to define the reconstructed top and anti-top quarks.

6 Background estimation

Several processes can lead to background contamination in the signal regions. The contributions from SM processes featuring the production of two, three or four prompt leptons is discussed in Section 6.1, whereas the estimation of backgrounds from processes where at least one of the reconstructed leptons originates from a non-prompt process is explained in Section 6.2.

6.1 Prompt-lepton backgrounds

6.1.1 Prompt backgrounds in 2ℓOS regions

The opposite-sign dilepton channel is dominated by two large, prompt contributions: dileptonic $t\bar{t}$ and Z+jets. The former enters primarily in the regions where the two b-jets can be tagged and reconstructed; it makes up 35% of the total expected event yields in the SR-2ℓ-5j2b and SR-2ℓ-6j2b signal regions, but only 10% in SR-2ℓ-6j1b. The Z+jets process, on the other hand, contributes around 80% of the event yield in the SR-2ℓ-6j1b signal region; this decreases to 55%–60% in the other two regions. Since the modelling of Z+jets in high jet-multiplicity regions can be problematic, especially when involving heavy-flavour jets, it is important to correct the predictions obtained from MC simulations with data: the normalisation of the $Z + b$ and $Z + c$ components are therefore obtained in data, simultaneously with the extraction of the signal strength in the combined inclusive fit described in Section 8.

To better model the $t\bar{t}$ process, a fully data-driven approach which relies on the high $t\bar{t}$ purity of an $e\mu$ selection is preferred instead. Selection criteria are further applied to replicate those of the signal regions, as defined in Table 2, and therefore limit the extrapolation between regions only to the change in lepton flavour to an OS different-flavour (DF) lepton pair ($e^{\pm}\mu^{\mp}$ in the regions used for the data-driven $t\bar{t}$ estimation, and $e^{\pm}e^{\mp}/\mu^{\pm}\mu^{\mp}$ in the SRs). These requirements are summarised in Table 6 below. The estimation of the $t\bar{t}$ background in the signal regions uses the distributions of the DNN output in data in the regions 2ℓ-$e\mu$-6j1b, 2ℓ-$e\mu$-6j2b and 2ℓ-$e\mu$-5j2b.

To be able to use the distribution of the DNN output from data $e\mu$ events in the $\ell\ell$ signal regions, the different acceptances and efficiencies need to be considered, and the non-$t\bar{t}$ background must be taken into account. The MC prediction for all non-$t\bar{t}$ background is first subtracted from the distribution of the DNN output in the $e\mu$ data. Then, the following correction factor is applied to the resulting data $e\mu$ distributions of the DNN output[11]:

$$C_{t\bar{t}} = \frac{N_{t\bar{t}}^{\ell\ell}}{N_{t\bar{t}}^{e\mu}},$$

[11] Since the DNN is not sensitive to the flavour of the leptons (see Table 22), no $e\mu \to \ell\ell$ correction to the shape of the DNN output is needed.

Table 6: Definition of the dilepton regions used for data-driven estimation of the $t\bar{t}$ background.

Variable	**Preselection**		
N_ℓ $(\ell = e, \mu)$	= 2		
	= 1 OSDF lepton pair with $\lvert m_{\ell\ell} - m_Z \rvert < 10$ GeV		
p_{T} (ℓ_1, ℓ_2)	> 30, 15 GeV		
	2ℓ-eμ-5j2b	**2ℓ-eμ-6j1b**	**2ℓ-eμ-6j2b**
N_{jets} $(p_{\mathrm{T}} > 25$ GeV)	= 5	$\geq$ 6	$\geq$ 6
$N_{b\text{-tagged jets@77\%}}$	$\geq$ 2	= 1	$\geq$ 2

where $N_{t\bar{t}}^{\ell\ell}$ and $N_{t\bar{t}}^{e\mu}$ are the numbers of expected $t\bar{t}$ events (from MC predictions) after the $\ell\ell$ selection in the SRs and the $e\mu$ selection in the regions for the data-driven $t\bar{t}$ estimation, respectively. The total uncertainty in this number is derived by including both the MC statistical error and the differences between alternative MC predictions, obtained by comparing the nominal value of the ratio with the values obtained by using a different h_{damp} parameter value, a different showering algorithm (Herwig 7.0.4) and a different matrix element generator (MadGraph5_aMC@NLO 2.3.3). The correction factors obtained in the three regions are found to agree very closely, and therefore an average factor of 0.982 ± 0.009 is used to apply the $e\mu \rightarrow \ell\ell$ correction in all dilepton signal regions. In addition to this uncertainty, both the statistical uncertainty related to the Poisson fluctuations of the data and the statistical uncertainty of the subtracted MC backgrounds are taken into account bin-by-bin for this background in all regions. The distribution of the b-tagged-jet multiplicity in 2ℓ-eμ-6j2b, illustrating the mismodelling of the $t\bar{t}$ background in high jet-multiplicity regions and highlighting the need to use the data-driven approach, is shown in Figure 1(a). The distributions of the DNN output, which are used in the data-driven estimation of the $t\bar{t}$ background in the 2ℓOS signal regions, are shown in Figures 1(b)–1(d).

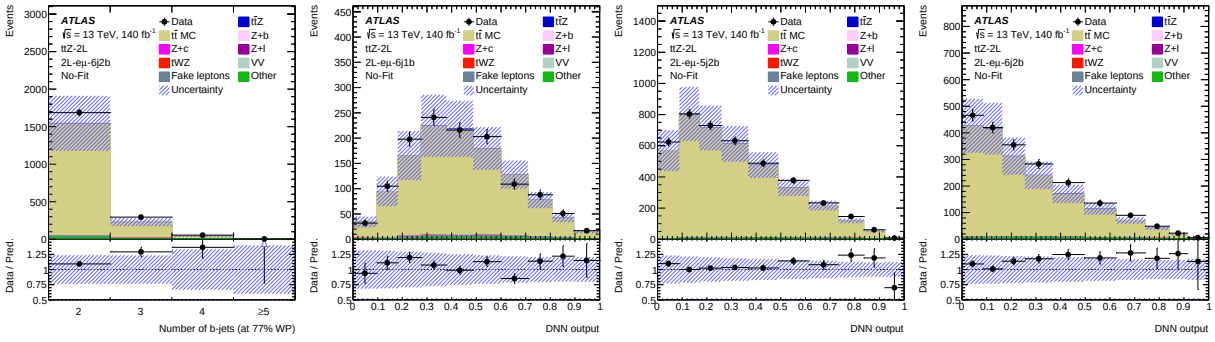

(a) (b) (c) (d)

Figure 1: Distributions of (a) the number of b-tagged jets in 2ℓ-eμ-6j2b, and the DNN output in (b) 2ℓ-eμ-6j1b, (c) 2ℓ-eμ-5j2b and (d) 2ℓ-eμ-6j2b. The shaded band corresponds to the total uncertainty (systematic and statistical) of the total pre-fit SM prediction. The lower panel shows the ratio of the data to the SM prediction. The last bin includes the overflow. These regions are not included in the fit and are only used for the fully data-driven estimation of the $t\bar{t}$ background in the dilepton signal regions.

6.1.2 Prompt backgrounds in 3ℓ regions

The dominant background processes in the trilepton signal regions are WZ+jets (with $WZ \to \ell\ell\ell\nu$) and tZq production. The heavy-flavour components of WZ+jets, in particular $WZ + b$, is most relevant, accounting for ~5% of the predicted event yield in SR-3ℓ-ttZ, ~8% in SR-3ℓ-tZq and ~31% in SR-3ℓ-WZ. The $WZ + c$ and $WZ + l$ contributions are roughly 3 and 20 times smaller, respectively. The tZq background is most relevant in SR-3ℓ-tZq, where it makes up ~22% of the predicted event yield – while the $t\bar{t}Z$ signal process is still twice as large. Since the tZq process cannot be completely separated from $t\bar{t}Z$, it is kept fixed to its best SM prediction and an appropriate set of normalisation and shape uncertainties are considered. The $WZ + b$ background, on the other hand, can be normalised to data because of its large contribution compared to other processes in SR-3ℓ-WZ. Another relevant process is tWZ, an irreducible singly resonant background to $t\bar{t}Z$. Due to its kinematic properties being so close to those of the signal process, no efficient discrimination can be obtained from the neural network used to define the 3ℓ signal regions: the tWZ process is therefore fixed to its SM prediction and yields a uniform 6%–10% contribution across the various DNN discriminant bins.

6.1.3 Prompt backgrounds in 4ℓ regions

The main background in the tetralepton channel is ZZ+jets, with $ZZ \to \ell^+\ell^-\ell'^+\ell'^-$. This background mainly affects the same-flavour signal region, but can also contribute in a minor way to the different-flavour region through $Z \to \tau^+\tau^- \to e^\pm\mu^\mp\nu_{\tau^+}\nu_{\tau^-}\nu_{e^\mp}\nu_{\mu^\pm}$. As in the trilepton channel, the tWZ process is a significant irreducible background, contributing between 8% and 10% of the total event yield in each of the signal regions. Other rare processes, such as VH or $t\bar{t}H$, typically contribute $\lesssim$2%. The contribution from the ZZ+jets process in the same-flavour signal region is about 13%, mostly from the $ZZ + b$ component: it is therefore useful to design a dedicated control region to normalise this component in data. The definition of CR-4ℓ-ZZ is given in Table 7 below. It is similar to that of SR-4ℓ-SF (see Table 4), but relies on an inverted cut on the DNN discriminant to ensure orthogonality. To suppress contributions from the $ZZ + l$ and $ZZ + c$ components in the extraction of the $ZZ + b$ normalisation (each contributing approximately a third of the event yield), the control region is split into two bins based on the PCBT bin value of the b-tagged jet with the highest PCBT value. The first bin contains events for which it is tagged at the 85%, 77% and 70% WPs, while the second bin corresponds to the tightest, i.e. 60%, WP. The second bin is dominated by the $ZZ + b$ background, and there is non-negligible $ZZ + l$ and $ZZ + c$ contamination in the first bin. Apart from the $ZZ + b$ background, all other prompt background processes in the 4ℓ channel are kept fixed to their best SM prediction.

Table 7: Definition of the tetralepton control region.

Variable	**Preselection**
N_ℓ $(\ell = e, \mu)$	$= 4$
	≥ 1 OSSF lepton pair with $\lvert m_{\ell\ell} - m_Z \rvert < 20$ GeV
	for all OSSF combinations: $m_{\text{OSSF}} > 10$ GeV
p_{T} $(\ell_1, \ell_2, \ell_3, \ell_4)$	$> 27,\ 7,\ 7,\ 7$ GeV
The sum of lepton charges	$= 0$
N_{jets} $(p_{\text{T}} > 25$ GeV)	≥ 2
$N_{b\text{-tagged jets}}$	≥ 1@85%
	CR-4ℓ-ZZ
$\ell\ell^{\text{non-}Z}$	e^+e^- or $\mu^+\mu^-$
DNN-SF output	< 0.4

6.2 Background from non-prompt/fake leptons

Fake or non-prompt leptons are objects unintentionally misidentified as prompt leptons. They can originate from various sources including meson decays, photon conversions or light jets accidentally creating lepton-like detector signatures. In the signal regions the typical source of non-prompt leptons[12] is the semileptonic decay of heavy-flavour hadrons, mainly from $t\bar{t}$ and Z+jets processes. While the impact of fake leptons is negligible in the 2ℓOS channel, the contribution can reach 12% (5%) of the expected yield in the 3ℓ (4ℓ) SRs.

Due to the small number of fake leptons in the dilepton channel, the MC estimate of the fake-lepton background is assigned a conservative 50% normalisation uncertainty. To estimate the contribution of fake leptons in the trilepton and tetralepton signal regions, a semi-data-driven method is used, called the 'template fit method'. The template fit method relies on using the data to normalise dedicated MC fake-lepton templates built from MC truth-record information about the origin and flavour of the fake leptons. Four distinct MC templates are defined for the major sources of fakes in this analysis: electrons from heavy-flavour sources ('F-e-HF'), electrons from other sources ('F-e-Other'), muons from heavy-flavour sources ('F-μ-HF'), and any other fake leptons that do not belong to any of the other sets or that come from events containing multiple fake leptons ('F-Other'). Only this last category is not normalised in data, and receives instead a 50% normalisation uncertainty.

To remain as kinematically close as possible to the 3ℓ signal regions, where the fakes contribution is most important, a set of trilepton control regions are designed. These employ the same lepton p_{T}, jet multiplicity and b-tagged jet multiplicity requirements as in the SRs. To ensure orthogonality with the SRs defined in Table 3, exactly one lepton must fail to satisfy the identification and isolation requirements applied to signal leptons – this lepton is said to be 'loose'. The heavy-flavour fake components can be isolated by defining $t\bar{t}$-enriched control regions: any event with an OSSF pair of leptons is vetoed, and the 'loose' lepton is required to be part of the same-sign pair of leptons. The flavour of the 'loose' lepton is then used to categorise events as CR-$t\bar{t}$-e or CR-$t\bar{t}$-μ. On the other hand, the 'F-e-Other' component can be obtained

[12] Hereafter referred to as 'fake leptons' or 'fakes'.

from a Z-like selection (CR-Z-e), requiring exactly three electrons of which two form an OS pair, and vetoing events with $E_{\mathrm{T}}^{\mathrm{miss}}$ greater than 80 GeV. These selection criteria are summarised in Table 8.

Table 8: Definition of the trilepton fakes control regions.

Variable	**Preselection**		
N_ℓ $(\ell = e, \mu)$	= 3 (of which = 1 loose non-tight)		
p_{T} (ℓ_1, ℓ_2, ℓ_3)	> 27, 20, 15 GeV		
Sum of lepton charges	±1		
N_{jets} $(p_{\mathrm{T}} > 25$ GeV)	≥ 3		
$N_{b\text{-tagged jets}}$	≥ 1@85%		
	CR-$t\bar{t}$-e	**CR-$t\bar{t}$-μ**	**CR-Z-e**
Lepton flavours	no OSSF pair (loose lepton is an electron)	no OSSF pair (loose lepton is a muon)	OSSF pair (exactly 3 electrons)
$E_{\mathrm{T}}^{\mathrm{miss}}$	—	—	< 80 GeV

The extraction of the three fake normalisation factors ($\mathcal{N}_{e,\mathrm{HF}}$, $\mathcal{N}_{e,\mathrm{other}}$ and $\mathcal{N}_{\mu,\mathrm{HF}}$) is first performed independently of the inclusive combined fit, in order to determine an additional uncertainty due to non-closure of key kinematic distributions in the fake-lepton CRs. This uncertainty, found to be 20% for fake electrons and 10% for fake muons, is applied to the fake templates in the SRs and later used in the combined fits. In CR-$t\bar{t}$-e and CR-$t\bar{t}$-μ, the overall event yields are used in the template fit, while in CR-Z-e, the distribution of the transverse mass of the W boson is fitted in six bins. These distributions are displayed in Figure 2, with the corresponding event yields shown in Table 9, after the inclusive combined fit to data.

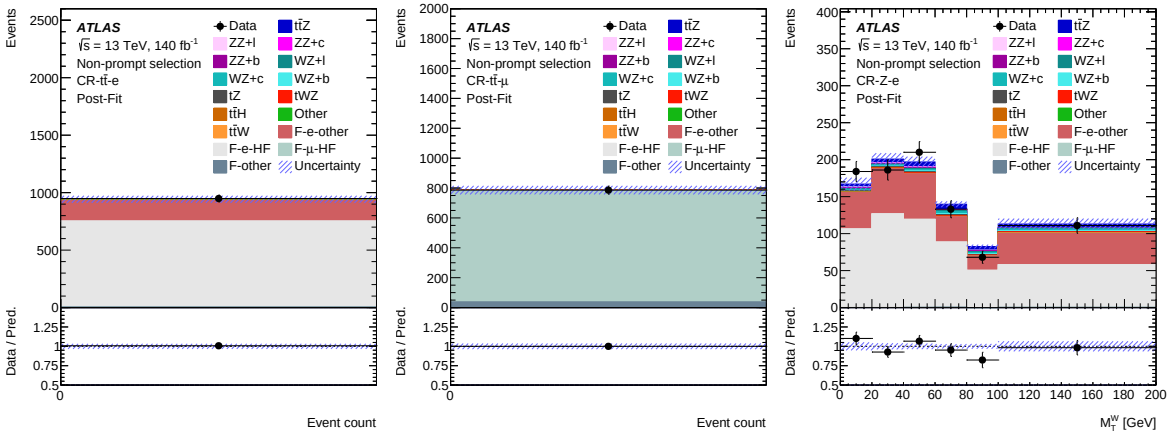

(a) (b) (c)

Figure 2: Post-fit distributions of the overall event yields in (a) CR-$t\bar{t}$-e and (b) CR-$t\bar{t}$-μ, and of (c) the W boson transverse mass in CR-Z-e. The shaded band corresponds to the total uncertainty (systematic and statistical) of the total SM prediction. The lower panel shows the ratio of the data to the SM prediction. The last bin includes the overflow.

Table 9: Observed and expected event yields in the fake-lepton control regions, obtained for an integrated luminosity of 140 fb^{-1} after the combined fit to data. The indicated errors include the Monte Carlo statistical uncertainty as well as all other systematic uncertainties discussed in Section 7. A dash (—) indicates event yields smaller than 0.1.

	CR-$t\bar{t}$-e	CR-$t\bar{t}$-μ	CR-Z-e
$t\bar{t}Z$	2.53 ± 0.21	0.71 ± 0.12	33.5 ± 1.4
$ZZ + l$	—	—	3.8 ± 1.1
$ZZ + c$	—	—	2.99 ± 0.95
$ZZ + b$	—	—	3.5 ± 1.8
$WZ + l$	0.29 ± 0.13	—	7.8 ± 3.1
$WZ + c$	0.36 ± 0.13	—	11.2 ± 4.3
$WZ + b$	0.16 ± 0.10	—	5.8 ± 3.3
tZq	0.21 ± 0.05	—	6.55 ± 0.99
tWZ	0.26 ± 0.04	—	3.81 ± 0.41
$t\bar{t}W$	2.9 ± 1.5	1.50 ± 0.75	1.41 ± 0.71
$t\bar{t}H$	4.46 ± 0.38	2.31 ± 0.20	3.20 ± 0.29
Other	1.2 ± 0.54	0.72 ± 0.32	0.52 ± 0.23
F-e-Other	177 ± 50	—	267 ± 72
F-e-HF	749 ± 70	—	548 ± 56
F-μ-HF	0.25 ± 0.02	744 ± 31	—
F-Other	3.0 ± 1.4	36 ± 16	1.03 ± 0.52
Total	943 ± 30	786 ± 28	901 ± 28
Data	949	786	892

7 Systematic uncertainties

The signal and background predictions are affected by several sources of experimental and theoretical systematic uncertainty. These are considered for both the inclusive and differential measurements presented in Sections 8 and 9. The uncertainties can be classified into the different categories which are described in the following subsections.

7.1 Detector-related uncertainties

The uncertainty in the combined 2015–2018 integrated luminosity is 0.83% [33]. This systematic uncertainty affects all processes determined from MC simulations for which the normalisation is not extracted from data.

The uncertainty in the reweighting of the MC pile-up distribution to match the distribution in data is evaluated by varying the pile-up correction factors and has a small impact on both the inclusive and differential results.

Uncertainties associated with the lepton selection arise from the trigger, reconstruction, identification and isolation efficiencies, and the lepton momentum scale and resolution [83–86]. They are below 1% for the individual sources and have a total impact of 1%–3% on the inclusive measurements.

Uncertainties associated with the jet selection arise from the jet energy scale (JES), the JVT requirement and the jet energy resolution (JER). The JES and its uncertainties are derived by combining information from test-beam data, collision data and simulation [90]. The JER has been measured separately for data and MC simulation using two in situ techniques, and a systematic uncertainty is obtained by defining its square to be the difference of the squares of the jet energy resolution in data and simulation. The uncertainties in the JER and from the JVT requirement increase at lower jet p_{T}.

The efficiency of the flavour-tagging algorithm is measured for each jet flavour using control samples in data and in simulation. From these measurements, correction factors are derived to correct the tagging rates in the simulation. In the case of b-tagged jets, the correction factors and their uncertainties are estimated from dileptonic $t\bar{t}$ events in data [92]. For c-tagged jets, they are derived from jets arising from W boson decays in $t\bar{t}$ events [101]. For light-flavour jets, the correction factors are derived using dijet events [102]. Sources of uncertainty affecting the b-, c- and light-flavour-tagging efficiencies are evaluated as a function of jet p_{T}, including bin-to-bin correlations. An additional uncertainty is assigned to account for the extrapolation of the b-tagging efficiency measurement from the p_{T} region used to determine the correction factors to regions with higher p_{T}. The impact of flavour-tagging uncertainties on the inclusive measurement is 1.7% overall.

Uncertainties are assigned to the scale and resolution of the soft track component of the missing transverse momentum. They are derived from differences seen between data and MC simulation when measuring the p_{T} balance between the hard and soft $E_{\mathrm{T}}^{\mathrm{miss}}$ components [103].

7.2 Signal modelling uncertainties

To estimate the uncertainties related to missing higher-order effects, the renormalisation and factorisation scale parameters μ_{r} and μ_{f} are either both doubled or both halved in the matrix element calculation and the results of the two variations are compared with the nominal predictions. Uncertainties in the PDF are evaluated by following the recommended PDF4LHC prescription [104] and include uncertainties related to the choice of PDF.

The uncertainties associated with the parton showering algorithm and the underlying event model[13] are evaluated by comparing the nominal samples, generated with MadGraph5_aMC@NLO interfaced to Pythia 8, with equivalent samples interfaced to Herwig 7 instead. Uncertainties related to the modelling of initial-state radiation are obtained by varying the Var3c parameter of the Pythia A14 tune in dedicated alternative samples, and their impact is found to largely cover that of final state radiation uncertainties.

The modelling of the $t\bar{t}Z$ signal process is cross-checked by comparing the nominal samples with alternative ones produced with the Sherpa generator, at various levels of precision (see Section 3 for more details). This comparison is not treated as an additional source of systematic uncertainty, as the shape differences between the nominal and Sherpa setups are found to be contained within the uncertainty band corresponding to the Herwig and `A14 Var3c` variations described above.

[13] In the following, it is referred to as the 'parton shower uncertainty'.

7.3 Background modelling uncertainties

Uncertainties in the $WZ \to \ell\ell\ell\nu$ (WZ+jets) and $ZZ \to \ell\ell\ell\ell$ (ZZ+jets) backgrounds related to the CKKW matching scale, QSF parameter (resummation scale) and alternative recoil scheme are estimated through the use of alternative truth-level samples. The renormalisation and factorisation scale uncertainties are evaluated simultaneously in both the matrix element calculation and the parton shower: the values of the scales are varied jointly by a factor of two and the results are compared with the nominal predictions. Uncertainties related to the choice of PDF are evaluated following the recommended PDF4LHC prescription and are derived by comparing the nominal value with those from the CT14 and MMHT2014 PDF sets. Variations of α_s in the nominal PDF are also included. In addition, a normalisation uncertainty of 30% is assigned to the $WZ + l$ and $WZ + c$ components of the WZ+jets background, evaluated from discrepancies found in comparisons between data and MC simulations. Similarly, normalisation uncertainties of 10% and 30% are assigned to the $ZZ + l$ and $ZZ + c$ components of the ZZ+jets background.

A cross-section normalisation uncertainty of 14% is assigned to the tZq process, based on the dedicated ATLAS measurement presented in Ref. [17]. A parton shower uncertainty is obtained by comparing an alternative sample of tZq events generated with MadGraph5_aMC@NLO interfaced to Herwig 7 with the nominal set-up (MadGraph5_aMC@NLO interfaced to Pythia 8). As with $t\bar{t}Z$, variations of the Var3c parameter of the Pythia A14 tune, and of the matrix element factorisation and renormalisation scales, are considered. Uncertainties related to the choice of PDF are evaluated following the PDF4LHC prescriptions.

For the tWZ background process, no parton shower uncertainty is considered, but instead the difference between samples generated with the DR1 and DR2 diagram removal schemes [61] is treated as a modelling uncertainty. Furthermore, both the shape and normalisation components of this systematic uncertainty are considered: in the absence of higher-order theoretical calculations for the tWZ process, a comparison of the cross sections obtained in the five-flavour scheme in the DR1 and DR2 set-ups leads to an overall 10%–15% normalisation uncertainty. PDF and scale uncertainties are also taken into account, in the same way as for the other processes described above.

Only theoretical uncertainties in the normalisation of the cross section of the $t\bar{t}H$ process are considered. Following the NLO QCD+EWK calculation presented in Ref. [19], the scale uncertainty is taken to be $^{+5.8\%}_{-9.2\%}$ and the PDF $\oplus$ α_s uncertainty is $\pm 3.6\%$.

Similarly to the diboson processes, variations of the CKKW matching scale and QSF parameter define independent modelling uncertainties for the Z+jets process. Renormalisation and factorisation scales in both the matrix element calculation and the parton shower are raised and lowered by a factor of two, and PDF uncertainties are evaluated according to the PDF4LHC prescription. The $Z + l$ component, the only one not extracted directly from a fit to data, is assigned a 10% normalisation uncertainty [105].

The dileptonic $t\bar{t}$ background in the 2ℓOS channel is estimated from the data-driven approach described in Section 6.1.1. Modelling uncertainties only enter via the correction factor $C_{t\bar{t}}$. The uncertainties on the final data-driven $t\bar{t}$ template also account for the MC statistical uncertainties of the subtracted MC background templates.

For other minor background processes, such as HV, VVV, $t\bar{t}W$, $t\bar{t}WW$ or multi-top-quark ($tt\bar{t}$, $t\bar{t}t\bar{t}$) production, an overall normalisation uncertainty of 50% is applied. For $t\bar{t}t\bar{t}$, an additional parton shower uncertainty is considered, by comparing samples interfaced to either Pythia 8 or Herwig 7. These background components typically contribute $\lesssim$1% of the event yield in the signal regions. As described in

Section 6.2, the MC template for fake leptons, which cannot be normalised in data as part of the fake-factor method, is assigned a 50% normalisation uncertainty. Non-closure uncertainties are derived for the other fake templates.

A few channel-specific exceptions to the above-mentioned treatment of the theoretical systematic uncertainties of the background are also included. In the 2ℓOS channel, the diboson background is significantly smaller than in the 3ℓ and 4ℓ channels. Splitting it into three flavor components and using all aforementioned mentioned uncertainties would lead to large MC statistical uncertainties in those templates, so all diboson events are treated as one background and are assigned a conservative 50% uncertainty. In the 3ℓ channel, the $ZZ + b$ background is not negligible, but still not large enough to measure its normalisation directly in data, as is done in the 4ℓ channel. A 50% normalisation uncertainty is assigned instead.

8 Results of the inclusive cross-section measurement

The $t\bar{t}Z$ cross section is first measured separately in each channel. The final result is then obtained by simultaneously fitting all three channels.

The fit is based on the profile-likelihood technique [106], with a likelihood function defined as a product of Poisson probability functions given by the observed event yields in the signal and control regions. The signal strength $\mu_{t\bar{t}Z}$, defined as the ratio of the observed $t\bar{t}Z$ cross section to the cross section predicted by the Monte Carlo simulation, and normalisations of some of the backgrounds (specified later in this section) are treated as free parameters of the fit. Systematic uncertainties described in Section 7 are introduced using additional nuisance parameters with Gaussian constraints. None of the uncertainties are found to be significantly constrained or pulled in the fit.

Since the signal MC samples with leptonic decay of the Z boson also contain a contribution from $\gamma^* \rightarrow \ell^+\ell^-$, the total cross section has to be corrected in order to remove the photon contribution. In accordance with the previous ATLAS [24] and CMS [23] measurements, the inclusive cross-section fiducial volume is defined using the requirement that the invariant mass of the fermion pair originating from Z/γ^* must be close to the Z-boson mass: 70 GeV $< m_{f\bar{f}} <$ 110 GeV. The total cross section is thus corrected by the fraction of parton-level events with a fermion-pair mass in this mass window; this fraction is found to be 94.5%, with MC statistical and signal modelling uncertainties well below 0.1%. The cross section, after correcting by the scale factor, is 0.828 pb.

In the dilepton channel, the distributions of the DNN output are fitted in all three SRs. No additional control regions are used. The binning is optimised to achieve the lowest possible $\mu_{t\bar{t}Z}$ uncertainty. The event yields are shown in Table 10 and the post-fit distributions of the DNN output are shown in Figure 3. The free parameters of the dilepton fit are the signal strength and the normalisations of the $Z + c$ and $Z + b$ backgrounds. The $t\bar{t}$ background is fixed to its estimated value obtained from $e\mu$ events in data as described in Section 6.1.1. The fitted value of the cross section can be found in the Table 13.

In the trilepton channel, the distribution of the DNN output, related to the probability of the event being a $t\bar{t}Z$ signal event, is fitted in the SR-3ℓ-ttZ and SR-3ℓ-tZq regions. The total number of events is fitted in the SR-3ℓ-WZ region. The post-fit plots for these distributions are shown in Figure 4. The event yields in the trilepton signal regions are shown in Table 11. In addition to the three trilepton signal regions, the three fake-lepton control regions, shown in Figure 2, are used in the fit to extract the normalisations of the fake-lepton backgrounds. The trilepton fit has five free parameters: the signal strength, normalisation of

Table 10: Post-fit event yields in the dilepton signal regions, obtained for an integrated luminosity of 140 fb^{-1}. The values of the fitted parameters from the combined fit are used. The data-driven approach described in Section 6.1.1 is used to estimate the $t\bar{t}$ background, denoted by $t\bar{t}$ DD. The indicated errors include the Monte Carlo statistical uncertainty as well as all other systematic uncertainties discussed in Section 7. Because of rounding and correlations between systematic uncertainties, the values quoted for the total yield and its uncertainty may differ from the simple sum over all processes.

	SR-2ℓ-5j2b	SR-2ℓ-6j2b	SR-2ℓ-6j1b
$t\bar{t}Z$	297 ± 20	443 ± 27	305 ± 28
$t\bar{t}$ DD	4 001 ± 72	1 913 ± 45	1 161 ± 35
$Z + b$	5 710 ± 170	2 680 ± 110	4 830 ± 280
$Z + c$	349 ± 95	189 ± 47	2 020 ± 480
$Z + l$	59 ± 25	19.6 ± 8.1	1 020 ± 240
tWZ	23.2 ± 0.92	34.4 ± 2.1	40.2 ± 1.9
Diboson	150 ± 80	95 ± 52	340 ± 180
Fake leptons	28 ± 14	18.6 ± 9.2	25 ± 12
Other	55 ± 25	49 ± 22	23 ± 10
Total	10 700 ± 100	5 440 ± 68	9 760 ± 110
Data	10 702	5 435	9 737

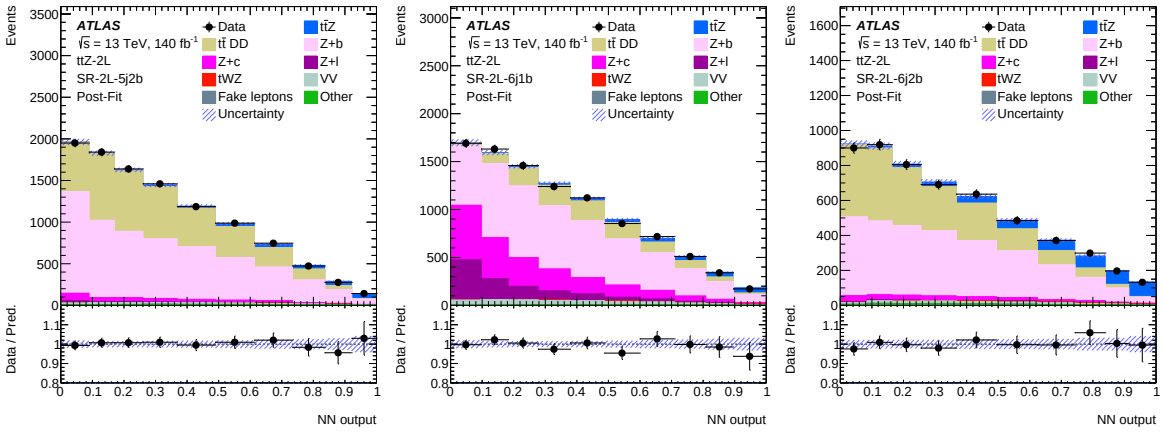

(a) (b) (c)

Figure 3: Distributions of the binary DNN output in the three dilepton signal regions used in the fit: (a) SR-2ℓ-5j2b, (b) SR-2ℓ-6j1b, and (c) SR-2ℓ-6j2b. The data-driven approach described in Section 6.1.1 is used to estimate the $t\bar{t}$ background, denoted by $t\bar{t}$ DD. The fitted values of the signal strength, background normalisations and nuisance parameters were applied to the MC templates in the plots. The shaded band corresponds to the total uncertainty (systematic and statistical) of the total SM prediction. The lower panel shows the ratio of the data to the SM prediction.

the $WZ + b$ background and normalisations of the three fake-lepton backgrounds. The fitted value of the cross section can be found in Table 13.

Table 11: Post-fit event yields in the trilepton signal regions and the tetralepton signal and control regions, obtained for an integrated luminosity of 140 fb^{-1}. The values of the fitted parameters from the combined fit are used. The indicated errors include the Monte Carlo statistical uncertainty as well as all other systematic uncertainties discussed in Section 7. Because of rounding and correlations between systematic uncertainties, the values quoted for the total yield and its uncertainty may differ from the simple sum over all processes. A dash (—) indicates event yields smaller than 0.1.

	SR-3ℓ-ttZ	SR-3ℓ-WZ	SR-3ℓ-tZq	SR-4ℓ-SF	SR-4ℓ-DF	CR-4ℓ-ZZ
$t\bar{t}Z$	441 ± 21	49.0 ± 3.7	151 ± 11	49.4 ± 3.0	51.1 ± 2.9	2.36 ± 0.23
$t\bar{t}W$	4.3 ± 2.2	2.2 ± 1.1	5.3 ± 2.6	—	—	—
$t\bar{t}H$	11.9 ± 1.1	1.43 ± 0.13	6.70 ± 0.57	2.79 ± 0.24	2.82 ± 0.24	0.32 ± 0.04
$WZ + b$	21.1 ± 7.4	47 ± 16	27.1 ± 9.5	—	—	—
$WZ + c$	8.9 ± 3.6	12.2 ± 5.0	11.1 ± 4.6	—	—	—
$WZ + l$	1.19 ± 0.52	1.70 ± 0.76	1.81 ± 0.80	—	—	—
$ZZ + b$	4.3 ± 2.5	6.9 ± 4.0	7.3 ± 4.2	7.5 ± 2.0	0.46 ± 0.12	26.7 ± 6.9
$ZZ + c$	1.23 ± 0.42	1.22 ± 0.43	1.61 ± 0.53	2.13 ± 0.66	0.30 ± 0.09	24.6 ± 7.1
$ZZ + l$	0.42 ± 0.13	0.26 ± 0.09	0.53 ± 0.15	0.83 ± 0.24	0.34 ± 0.09	22.6 ± 5.2
tZq	20.8 ± 4.0	13.2 ± 2.3	99 ± 16	—	—	—
tWZ	40.0 ± 7.6	18.0 ± 4.2	24.2 ± 3.0	6.60 ± 0.82	7.3 ± 1.2	0.69 ± 0.1
$t\bar{t}t\bar{t}$	1.56 ± 0.78	0.13 ± 0.07	0.27 ± 0.14	—	—	—
Other	1.33 ± 0.61	1.40 ± 0.63	0.39 ± 0.19	0.55 ± 0.25	1.12 ± 0.52	0.55 ± 0.25
F-e-HF	4.6 ± 1.0	3.90 ± 0.87	12.0 ± 2.6	0.28 ± 0.07	0.45 ± 0.10	0.11 ± 0.03
F-e-Other	7.8 ± 2.7	7.3 ± 2.6	15.2 ± 5.4	0.39 ± 0.14	0.50 ± 0.18	0.10 ± 0.04
F-μ-HF	6.98 ± 0.86	5.27 ± 0.66	18.2 ± 2.2	0.58 ± 0.07	0.62 ± 0.08	0.16 ± 0.02
F-Other	2.8 ± 1.2	2.7 ± 1.2	4.4 ± 2.0	0.90 ± 0.40	1.66 ± 0.74	0.33 ± 0.15
Total	580 ± 19	174 ± 13	386 ± 15	72.0 ± 3.4	66.7 ± 3.0	78.5 ± 8.0
Data	569	175	388	79	74	81

In the tetralepton channel, the distributions of the two DNN outputs are fitted in the SR-4ℓ-SF and SR-4ℓ-DF regions. The distribution of the b-tagging score of the leading b-tagged jet is fitted in CR-4ℓ-ZZ. The post-fit plots for these distributions are shown in Figure 5. The event yields in the tetralepton signal regions are shown in Table 11. In addition to the two tetralepton signal regions and ZZ control region, the three fake-lepton control regions, shown in Figure 2, are used in the fit to extract the normalisations of the fake-lepton backgrounds. The tetralepton fit has five free parameters: the signal strength, normalisation of the $ZZ + b$ background and normalisations of the three fake-lepton backgrounds. The fitted value of the cross section can be found in the Table 13.

The combined inclusive fit uses all of the aforementioned signal and control regions, i.e. three dilepton signal regions, three trilepton signal regions, two tetralepton signal regions, CR-4ℓ-ZZ and three fake-lepton control regions. The fitted value of the inclusive cross section is found to be 0.86 ± 0.05 pb, in good agreement with the theory prediction [21] and with a relative precision of 6%. For comparison, the previous result [24] achieved a 10% uncertainty for the $t\bar{t}Z$ cross section, using the same dataset. All free floating background normalisations are consistent with the SM predictions within their uncertainties. The

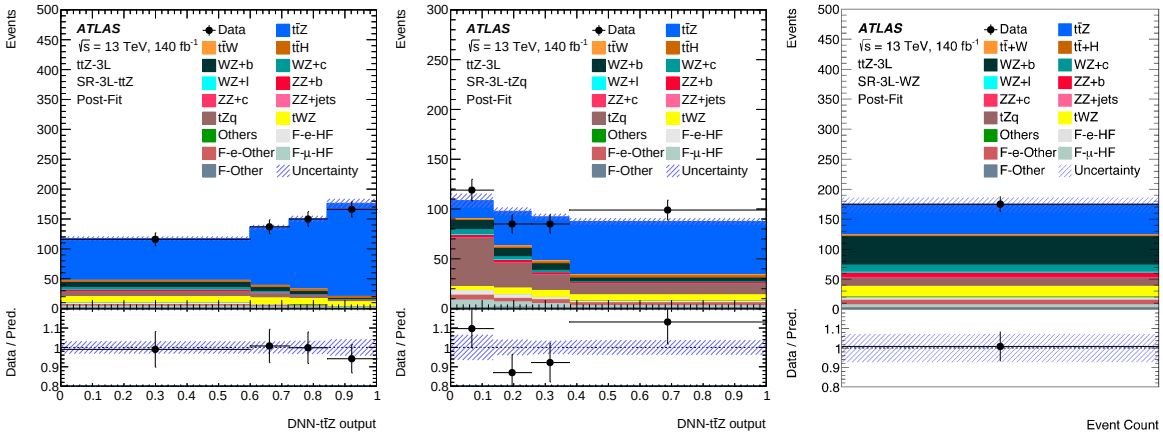

(a) (b) (c)

Figure 4: Distributions of the $t\bar{t}Z$-node of the multi-class DNN output and total event yield in the three trilepton signal regions used in the fit: (a) SR-3ℓ-ttZ, (b) SR-3ℓ-tZq, and (c) SR-3ℓ-WZ. The fitted values of the signal strength, background normalisations and nuisance parameters were applied to the MC templates in the plots. The shaded band corresponds to the total uncertainty (systematic and statistical) of the total SM prediction. The lower panel shows the ratio of the data to the SM prediction.

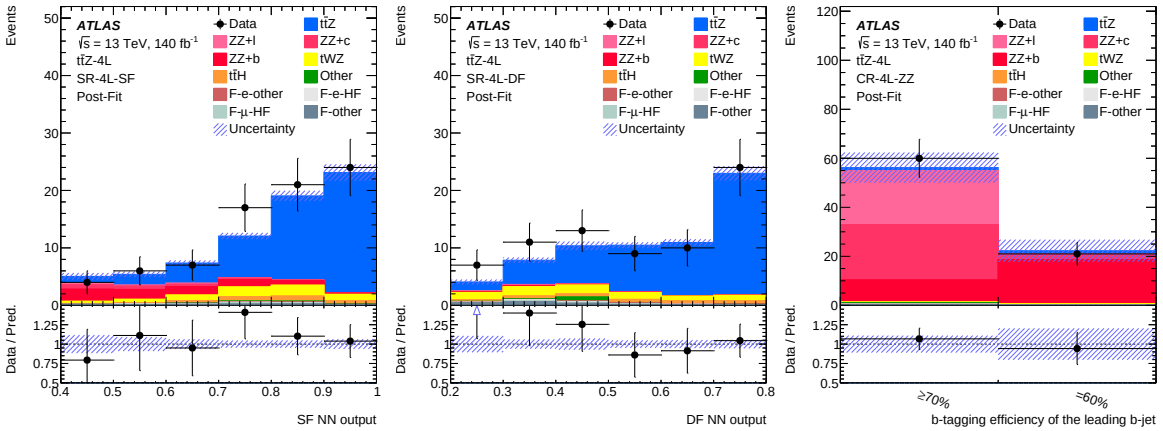

(a) (b) (c)

Figure 5: Distributions of the binary DNN outputs in the two tetralepton signal regions used in the fit, (a) SR-4ℓ-SF and (b) SR-4ℓ-DF, as well as of (c) the b-tagging efficiency of the leading b-tagged jet in the control region CR-4ℓ-ZZ. The fitted values of the signal strength, background normalisations and nuisance parameters were applied to the MC templates in the plots. The shaded band corresponds to the total uncertainty (systematic and statistical) of the total SM prediction. The lower panel shows the ratio of the data to the SM prediction.

breakdown of the combination into the contributing channels can be found in Table 13. A mild upwards fluctuation in the data is observed in the 4ℓ channel. The p-value for compatibility of the cross section measured in the combination and the values fitted individually is 53%, indicating good agreement between the different analysis channels. The values of the background normalisation factors obtained from the inclusive cross-section fit can be found in the Table 12. A deviation from unity is observed only for N_{Z+c}, which compensates for the mismodelling of the $Z+c$ background in SR-2ℓ-6j1b. All other normalisation

factors are consistent with their respective SM predictions. No significant pulls or constraints are observed in the fit, except for the CKKW and QSF scales of the $Z + b$ background, which are pulled by $\approx 1\sigma$. These pulls are caused by the mismodelling of the Z+jets background in SR-2ℓ-5j2b and SR-2ℓ-6j1b. The effects of systematic uncertainties on the result are listed in Table 14. The dominant systematic uncertainties are those in the background normalisations and those related to jets and missing transverse momentum.

Table 12: Values of background normalisation factors measured in the combined inclusive fit. Both statistical and systematic uncertainties are considered.

Norm. factor	Value
$\mathcal{N}_{ZZ+b}$	$1.1^{+0.4}_{-0.4}$
$\mathcal{N}_{WZ+b}$	$0.9^{+0.4}_{-0.4}$
$\mathcal{N}_{Z+b}$	$1.08^{+0.11}_{-0.10}$
$\mathcal{N}_{Z+c}$	$0.61^{+0.23}_{-0.20}$
$\mathcal{N}_{e,\mathrm{HF}}$	$0.89^{+0.09}_{-0.09}$
$\mathcal{N}_{e,\mathrm{other}}$	$1.2^{+0.4}_{-0.4}$
$\mathcal{N}_{\mu,\mathrm{HF}}$	$1.02^{+0.08}_{-0.08}$

Table 13: Measured $t\bar{t}Z$ cross sections obtained from the fits in the signal regions with different lepton multiplicities and corrected to parton level. The uncertainties include those from statistical and systematic sources.

Channel	$\sigma_{t\bar{t}Z}$
Dilepton	0.84 ± 0.11 pb $= 0.84 \pm 0.06$ (stat.) ± 0.09 (syst.) pb
Trilepton	0.84 ± 0.07 pb $= 0.84 \pm 0.05$ (stat.) ± 0.05 (syst.) pb
Tetralepton	$0.97^{+0.13}_{-0.12}$ pb $= 0.97 \pm 0.11$ (stat.) ± 0.05 (syst.) pb
Combination ($2\ell, 3\ell$ & 4ℓ)	0.86 ± 0.05 pb $= 0.86 \pm 0.04$ (stat.) ± 0.04 (syst.) pb

Table 14: Grouped impact of systematic uncertainties in the combined inclusive fit to data. The uncertainties are symmetrised for presentation and grouped into the categories described in the text. The quadrature sum of the individual uncertainties is not equal to the total uncertainty because of correlations introduced by the fit.

Uncertainty Category	$\Delta\sigma_{t\bar{t}Z}/\sigma_{t\bar{t}Z}$ [%]
Background normalisations	2.0
Jets and $E_{\mathrm{T}}^{\mathrm{miss}}$	1.9
b-tagging	1.7
$t\bar{t}Z$ μ_{f} and μ_{r} scales	1.6
Leptons	1.6
Z+jets modelling	1.5
tWZ modelling	1.1
$t\bar{t}Z$ showering	1.0
$t\bar{t}Z$ A14 tune	1.0
Luminosity	1.0
Diboson modelling	0.8
tZq modelling	0.7
PDF (signal & backgrounds)	0.6
MC statistical	0.5
Other backgrounds	0.5
Fake leptons	0.4
Pile-up	0.3
Data-driven $t\bar{t}$	0.1

9 Unfolding and differential cross-section measurements

The differential measurement is performed in the 3ℓ and 4ℓ channels, using definitions of the fiducial volumes described in Section 5.4. The dilepton channel is not used because of its high background contamination. A profile-likelihood unfolding method is used, as described in Section 9.1. The observables that are unfolded and their binning are listed in Sections 9.2 and 9.3, and the results are presented in Section 9.4.

9.1 Profile-likelihood unfolding procedure

A profile-likelihood unfolding (PLU) procedure is used to measure differential cross sections. A likelihood model is built for the detector-level distribution by treating the contribution from each truth-level bin as a subcomponent of the detector-level signal. The likelihood takes the form:

$$L\left(\vec{n}|\vec{\mu},\vec{\theta},\vec{\lambda}\right) = \prod_{r\in\text{reg.}}\prod_{i\in\substack{\text{det.}\\\text{bins}}}\text{Pois}\left(n_{i,r}|L_{\text{int}}\sum_{j\in\substack{\text{gen.}\\\text{bins}}}\mathcal{R}_{ij,r}(\vec{\theta})\mu_j\sigma_j^{\text{MC}}+B_{i,r}(\vec{\theta},\vec{\lambda})\right)\times\prod_{k\in\text{NPs}}\text{Gaus}\left(\theta_k\right)\times R(\vec{\mu}), \quad (1)$$

where i indicates the detector-level bin index, j the truth-level bin index, k the systematic uncertainty index, and the index r runs over all control and signal regions. The number of observed detector-level events in a given bin, $n_{i,r}$, is compared with the prediction obtained by folding the truth-level signal differential cross section σ_j^{MC} through the response matrix $\mathcal{R}_{ij,r}$, appropriately normalised to the integrated luminosity L_{int}, and adding the background contribution $B_{i,r}$, which depends on the background normalisation factors $\vec{\lambda}$. The expected truth-level differential cross section $\vec{\sigma}$ is associated bin-wise with the normalisation factors $\vec{\mu}$, the parameters of interest of PLU. To obtain a normalised differential distribution, the last element of $\vec{\mu}$ is reparameterised in terms of all the other ones and the integrated fiducial cross section.

The response matrix is defined as:

$$\mathcal{R}_{ij} = \frac{1}{\alpha_i}\epsilon_j \mathcal{M}_{ij},$$

where the migration matrix $\mathcal{M}_{ij}$ quantifies the bin-to-bin migrations of events from truth level to detector level due to resolution effects. It is computed as:

$$\mathcal{M}_{ij} = \frac{N_{ij}^{\text{det.}\cap\text{fid.}}}{N_j^{\text{det.}\cap\text{fid.}}}.$$

The superscript det. $\cap$ fid. indicates events that pass both the detector-level event selection and the fiducial selection. The numerator $N_{ij}^{\text{det.}\cap\text{fid.}}$ is the expected number of detector-level events in detector-level bin i and truth-level bin j, while the denominator $N_j^{\text{det.}\cap\text{fid.}}$ is the expected number of detector-level events in truth-level bin j summed over all detector-level bins.

The response matrix then receives acceptance corrections, α_i, which define the fraction of events that satisfy the detector-level selection and originate from configurations outside the truth-level fiducial selection:

$$\alpha_i = \frac{N_i^{\text{det.}\cap\text{fid.}}}{N_i^{\text{det.}}}.$$

Finally, efficiency corrections, ϵ_j, are also applied to account for events that satisfy the fiducial phase-space selection criteria but are not reconstructed in the detector:

$$\epsilon_j = \frac{N_j^{\text{det.}\cap\text{fid.}}}{N_j^{\text{fid.}}}.$$

Here, $N_i^{\text{det.}}$ and $N_j^{\text{fid.}}$ represent the expected number of events in the i^{th} and j^{th} bins of the detector-level and fiducial truth-level histograms, while $N_i^{\text{det.}\cap\text{fid.}}$ is the expected number of detector-level events in detector-level bin i summed over all truth-level bins.

Systematic uncertainties, associated with the nuisance parameters (NPs) $\vec{\theta}$, enter the likelihood in two ways: in the background term $B_{i,r}(\vec{\theta},\vec{\lambda})$, and in the folded signal term via $R_{ij,r}(\vec{\theta})$. Each NP is subject to a Gaussian constraint in the likelihood fit. Those accounting for the statistical uncertainties in each bin due to the limited size of the simulated event samples are assigned Poisson constraints instead, following the Beeston–Barlow 'lite' method [107].

The PLU procedure can be regularised via the additional constraint term $R(\vec{\mu})$ in Eq. (1). Specifically, a discretised second-derivative regularisation, also known as Tikhonov regularisation [108–111], is used:

$$R(\vec{\mu}) = \exp\left[-\frac{\tau^2}{2}\sum_{i=2}^{i+1<N_{\text{bins}}}\left((\mu_i - \mu_{i-1}) - (\mu_{i+1} - \mu_i)\right)^2\right],$$

where the sum runs over the bins of the unfolded distribution and τ is the regularisation parameter. Its value depends on the observable, and is shown in Table 15.

The aim of the regularisation is to suppress strong anti-correlations between the bins of the unfolded distribution, arising from migrations between the bins. Higher values of the regularisation parameter τ lead to lower uncertainties. However, too strong regularisation can lead to biased results and turns anti-correlations between the neighbouring bins into correlations. In order to find a compromise between these two effects, the τ values were scanned with a step size of 0.1, starting from zero. For each τ, a pseudo-dataset generated according to the SM expectation values (so-called 'Asimov dataset') was unfolded and the global correlation factor defined in Eq. (2) was evaluated:

$$\rho = \left\langle \sqrt{1 - (C_{ii}C_{ii}^{-1})^{-1}} \right\rangle, \tag{2}$$

where C_{ij} is the correlation matrix, C_{ij}^{-1} its inverse, and the brackets represent the mean value. The τ value where the global correlation reaches its minimum was chosen as the optimal value.

In order to verify that the unfolding is able to recover an alternative truth-level distribution, a number of stress tests are performed. Motivated by the potential impact of EFT effects on the high-p_{T} tail of the p_{T}^Z distribution, this observable's distribution is linearly reweighted, with slopes ranging from −0.25 to 1.00, between 0 and 1 TeV. The corresponding event-wise correction factor, which is 1.0 at $p_{\text{T}}^Z = 0$ TeV and ranges from 0.75 to 2.0 at $p_{\text{T}}^Z = 1$ TeV, is used to reweight all of the other observables in this pseudo-EFT-effect stress test. Additionally, data-driven stress tests are performed, where the histogram of the ratio of observed to expected signal in the unfolded variable at detector level is fitted with a quadratic function and the value of the function is then used to apply the weight. Another kind of stress test uses a histogram of the ratio of observed to expected signal as a function of the scalar sum of lepton transverse momenta, H_{T}^{ℓ}, which was found to be the most poorly modelled variable (lowest p-value at detector level), and the value of the ratio is used to apply the weight. All the stress tests show that the unfolding is quite able to recover an alternative distribution, with an average χ^2/ndf well below 0.05.

9.2 Differential observables

The optimal choice of unfolded observables was based on their physics importance and sensitivity to EFT operators. A list of the observables used in the differential measurement can be found in Table 15.

The observables are unfolded either in one of the channels, or in their combination, taken as the union of the fiducial volumes defined in Section 5.4. The observables relying on a particular decay mode of the $t\bar{t}$ system are unfolded only in the corresponding channel. Two observables, N_{jets} and H_{T}^{ℓ}, were unfolded separately in each of the two channels, as their distributions are expected to differ between the channels. The observables not requiring a particular decay of the $t\bar{t}$ system are unfolded in the combined 3ℓ and 4ℓ channels. Each of the observables is unfolded to both particle level and parton level, except for N_{jets}, which

is unfolded only to particle level. For observables requiring hadronic top reconstruction, the migration matrices are somewhat non-diagonal (~40%–70% on diagonal, compared to purely leptonic observables with >90% on the diagonal). In these cases, unregularised unfolding would yield large fluctuations, so Tikhonov regularisation is applied.

Table 15: Summary of the variables used for the differential measurement, and the values of the regularisation parameter τ for particle level and parton level for the relevant variables.

	Variable	Regularisation	τ^{particle}	τ^{parton}	Definition
$3\ell + 4\ell$	p_{T}^{Z}	No	-	-	Transverse momentum of the Z boson
	$\lvert y^{Z}\rvert$	No	-	-	Absolute rapidity of the Z boson
	$\cos\theta^{*}_{Z}$	No	-	-	Angle between the direction of the Z boson in the detector reference frame and the direction of the negatively charged lepton in the rest frame of the Z boson
	p_{T}^{t}	Yes	1.5	1.4	Transverse momentum of the top quark
	$p_{\text{T}}^{t\bar{t}}$	Yes	1.6	1.5	Transverse momentum of the $t\bar{t}$ system
	$\lvert\Delta\Phi(t\bar{t}, Z)\rvert/\pi$	Yes	2.4	2.1	Absolute azimuthal separation between the Z boson and the $t\bar{t}$ system
	$m^{t\bar{t}Z}$	Yes	1.5	1.6	Invariant mass of the $t\bar{t}Z$ system
	$m^{t\bar{t}}$	Yes	1.5	1.4	Invariant mass of the $t\bar{t}$ system
	$\lvert y^{t\bar{t}Z}\rvert$	Yes	1.5	1.5	Absolute rapidity of the $t\bar{t}Z$ system
3ℓ	H_{T}^{ℓ}	No	-	-	Sum of the transverse momenta of all the signal leptons
	$\lvert\Delta\Phi(Z, t_{\text{lep}})\rvert/\pi$	No	-	-	Absolute azimuthal separation between the Z boson and the top (anti-top) quark featuring the $W \to \ell\nu$ decay
	$\lvert\Delta y(Z, t_{\text{lep}})\rvert$	No	-	-	Absolute rapidity difference between the Z boson and the top (anti-top) quark featuring the $W \to \ell\nu$ decay
	$p_{\text{T}}^{\ell,\text{non-}Z}$	No	-	-	Transverse momentum of the lepton that is not associated with the Z boson
	N_{jets}	No	-	-	Number of selected jets with $p_{\text{T}} > 25\,\text{GeV}$ and $\lvert\eta\rvert < 2.5$
4ℓ	H_{T}^{ℓ}	No	-	-	Sum of the transverse momenta of all the signal leptons
	$\lvert\Delta\Phi(\ell_{t}^{+}, \ell_{\bar{t}}^{-})\rvert/\pi$	No	-	-	Absolute azimuthal separation between the two leptons from the $t\bar{t}$ system
	N_{jets}	No	-	-	Number of selected jets with $p_{\text{T}} > 25\,\text{GeV}$ and $\lvert\eta\rvert < 2.5$

9.3 Choice of binning

The binning for all the observables is summarised in Table 25 in the Appendix. The binning is optimised, starting from the requirement that the statistical uncertainty in all unfolded bins be lower than 35% for variables unfolded in the 4ℓ channel only, and lower than 25% for the 3ℓ and 3ℓ+4ℓ variables. Furthermore, diagonal elements of the migration matrix (MM) must exceed a chosen threshold (starting from a high value and iteratively decreasing it). The first bin of the distribution is chosen to have the smallest possible range for which these two requirements are satisfied (narrow bins lead to large migrations and high statistical uncertainties; widening the bin decreases the uncertainty and increases the diagonal elements of the

migration matrix). Once the range of the first bin is chosen, the next bin is optimised. Given the two requirements, only a limited number of bins can be chosen. The requirement on the minimum value of MM diagonal elements is gradually decreased to obtain binning for a higher number of bins. The binning is optimised for a number of bins ranging from two to ten, using only the predicted statistical uncertainties and unfolding to particle level. Then stress tests are performed for each choice of binning: the one with the largest number of bins that still passes all stress tests is selected. The same binning is used for both particle level and parton level.

9.4 Unfolded cross-section measurements

The full set of unfolded results for the transverse momentum of the Z boson are presented in this section. For brevity, only the absolute differential cross sections unfolded to particle level are shown for other observables. All other differential results (including normalised distributions, and unfolding to parton level) are available in the Appendix.

Figure 6 shows the distribution of detector-level p_{T}^{Z} in 3ℓ signal regions, as well as the migration matrices, acceptances and efficiencies. The acceptance is the fraction of the signal in a given bin of the detector-level distribution which passes the truth-level fiducial volume cuts. The efficiency is defined as the fraction of the events from a given bin of the truth-level distribution passing the selection in the given detector-level region. Figure 7 shows similar plots for 4ℓ signal regions. The unfolded distributions in the combination of the 3ℓ and 4ℓ channels, as well as the nominal truth-level MC prediction, and alternative generator predictions are shown in Figure 8. The uncertainties of the unfolded distributions range approximately from 15% to 40%. In general, small uncertainties are observed for the variables that are reconstructed only from leptons and unfolded in the combined 3ℓ and 4ℓ channels. A large number of data events and small migrations between the bins lead to the small uncertainties. On the other hand, the variables unfolded only in the 4ℓ channel suffer from a low number of events, which results in relatively high statistical uncertainties. The unfolding to particle level has lower uncertainties than unfolding to parton level, because of the more diagonal migration matrices, and normalised unfolded distributions are also more precise than the absolute distributions, because the normalisation significantly reduces the uncertainties. The statistical uncertainty of the data is the dominant source of uncertainty in all distributions and bins. Compared to the statistical uncertainty, the systematic uncertainties have a significantly smaller effect.

The compatibility of the unfolded distributions and the predictions was assessed by calculating χ^2 values, using the uncertainties of the unfolded distribution and their correlations. The corresponding p-values can be found in the Appendix, in Table 26 for absolute unfolded distributions and in Table 27 for normalised distributions. The p-values indicate good agreement between the unfolded data and the prediction for most of the variables. The lowest p-values, around 2%, are observed for H_{T}^{ℓ}; this is expected because this variable was seen to be the most poorly modelled one (with the lowest p-values) at detector level.

The absolute differential cross sections unfolded to particle level for observables defined in the 3ℓ and 4ℓ channels separately are shown in Figures 9 and 10, while Figures 11 and 12 present those defined in the combination of the two channels. All other results are available in the Appendix: Figures 16 and 17 for the unregularised observables in the combined 3ℓ and 4ℓ channels, Figures 18–23 for the regularised ones, Figures 24–28 for those defined in the 3ℓ channel only, and Figures 29–31 for those defined in the 4ℓ channel only.

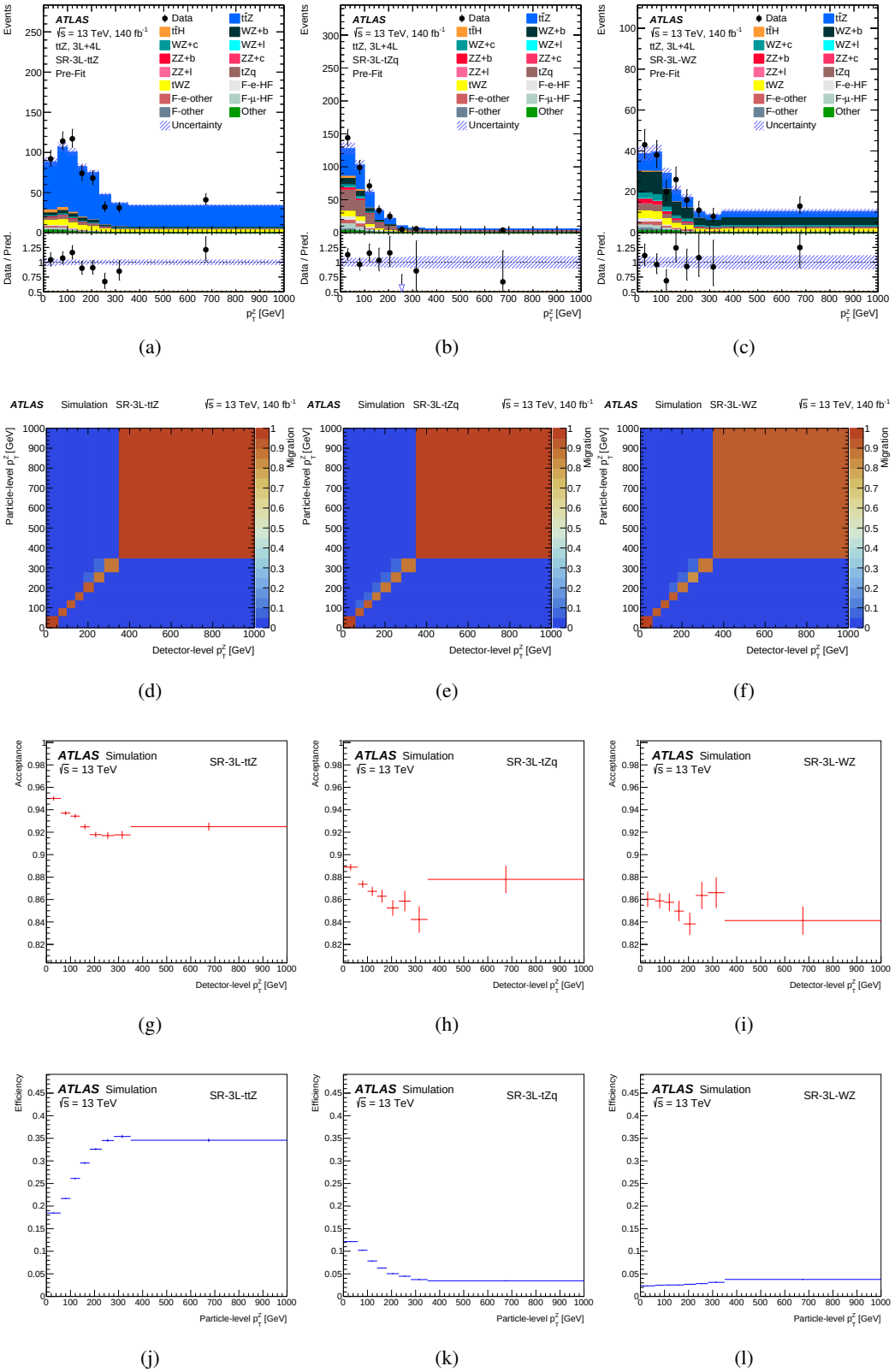

Figure 6: Detector-level distributions (a,b,c), together with migration matrices (d,e,f) and acceptance (g,h,i) and efficiency (j,k,l) histograms for the p_{T}^{Z} observable in the trilepton channel regions: SR-3ℓ-ttZ (a,d,g,j), SR-3ℓ-tZq (b,e,h,k) and SR-3ℓ-WZ (c,f,i,l). Migration matrices and corrections apply to the particle level.

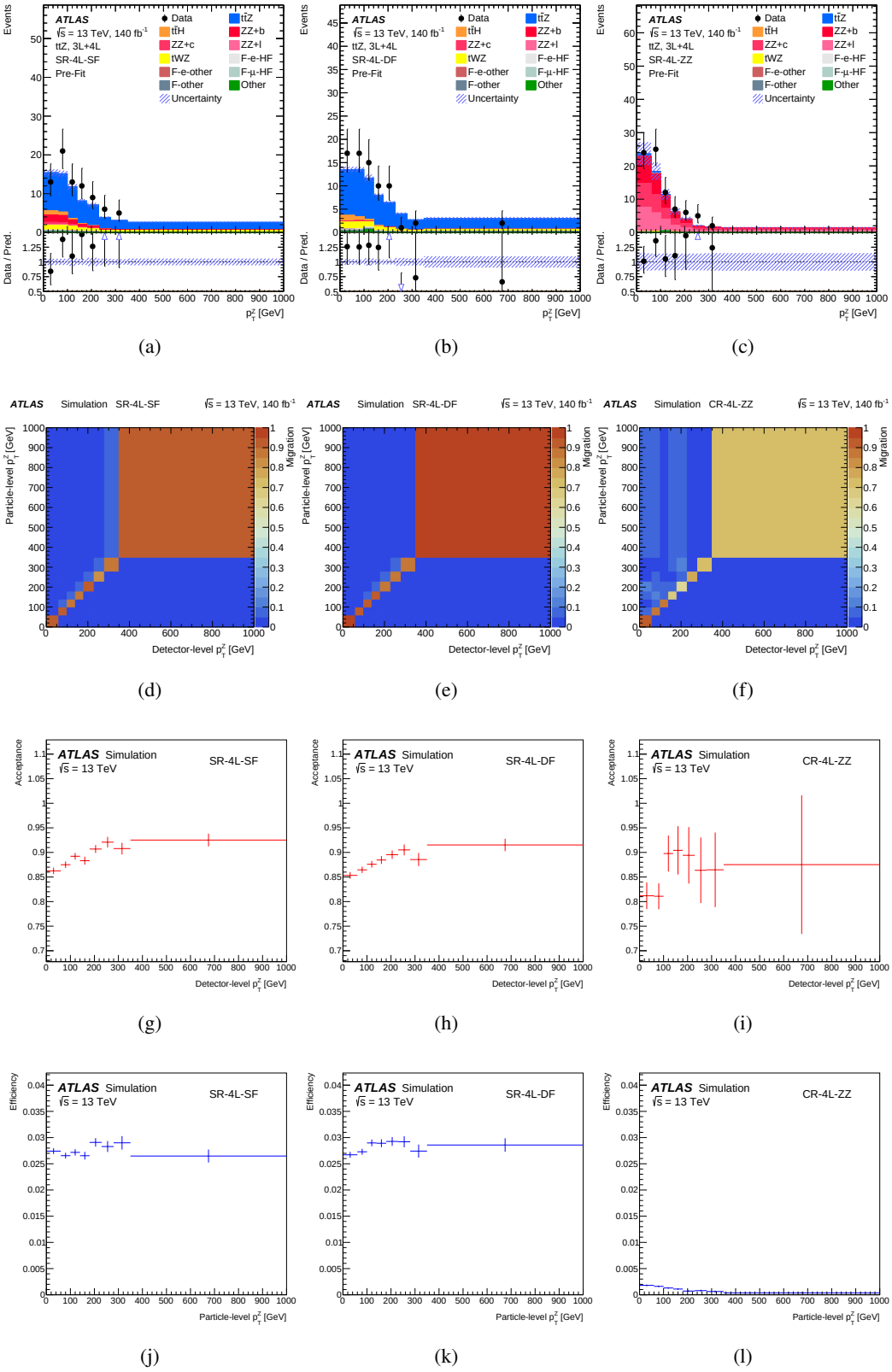

Figure 7: Detector-level distributions (a,b,c), together with migration matrices (d,e,f) and acceptance (g,h,i) and efficiency (j,k,l) histograms for the p_{T}^{Z} observable in the tetralepton channel regions: SR-4ℓ-SF (a,d,g,j), SR-4ℓ-DF (b,e,h,k) and CR-4ℓ-ZZ (c,f,i,l). Migration matrices and corrections apply to the particle level.

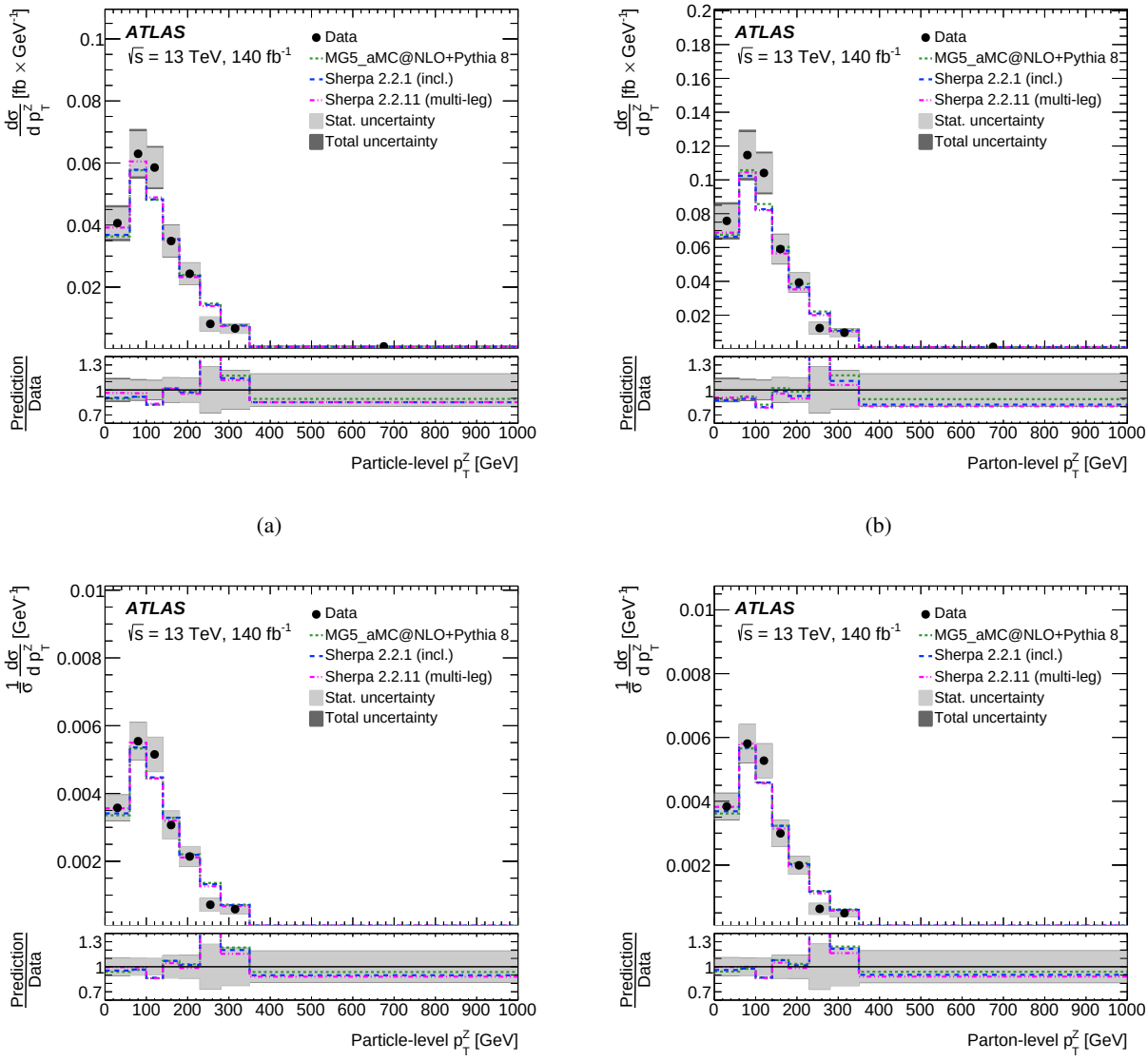

Figure 8: Differential cross-section measurements as a function of p_{T}^{Z} observable in the combined 3ℓ and 4ℓ channels, (a,b) absolute and (c,d) normalised, unfolded to (a,c) particle level and (b,d) parton level. The dark grey band corresponds to the total uncertainty of the measurement; in some cases, it is almost fully covered by the light grey band, representing the dominant statistical uncertainty. Alternative generator predictions are overlaid as additional coloured lines.

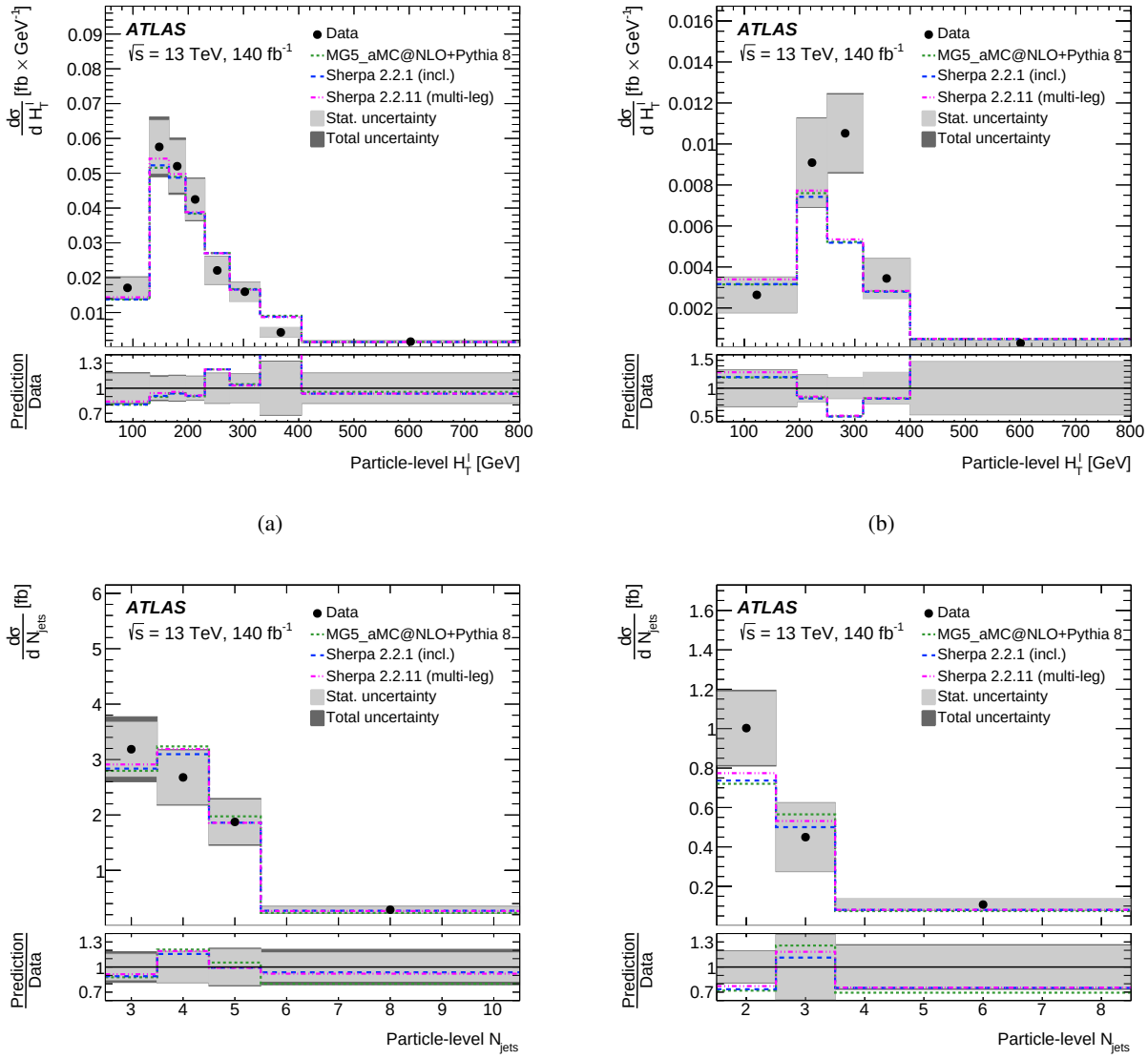

Figure 9: Absolute differential cross-section measurements, unfolded to particle level, as a function of H_{T}^{ℓ} in the (a) 3ℓ and (b) 4ℓ channels, and N_{jets} in the (c) 3ℓ and (d) 4ℓ channels. The dark grey band corresponds to the total uncertainty of the measurement; in some cases, it is almost fully covered by the light grey band, representing the dominant statistical uncertainty. Alternative generator predictions are overlaid as additional coloured lines.

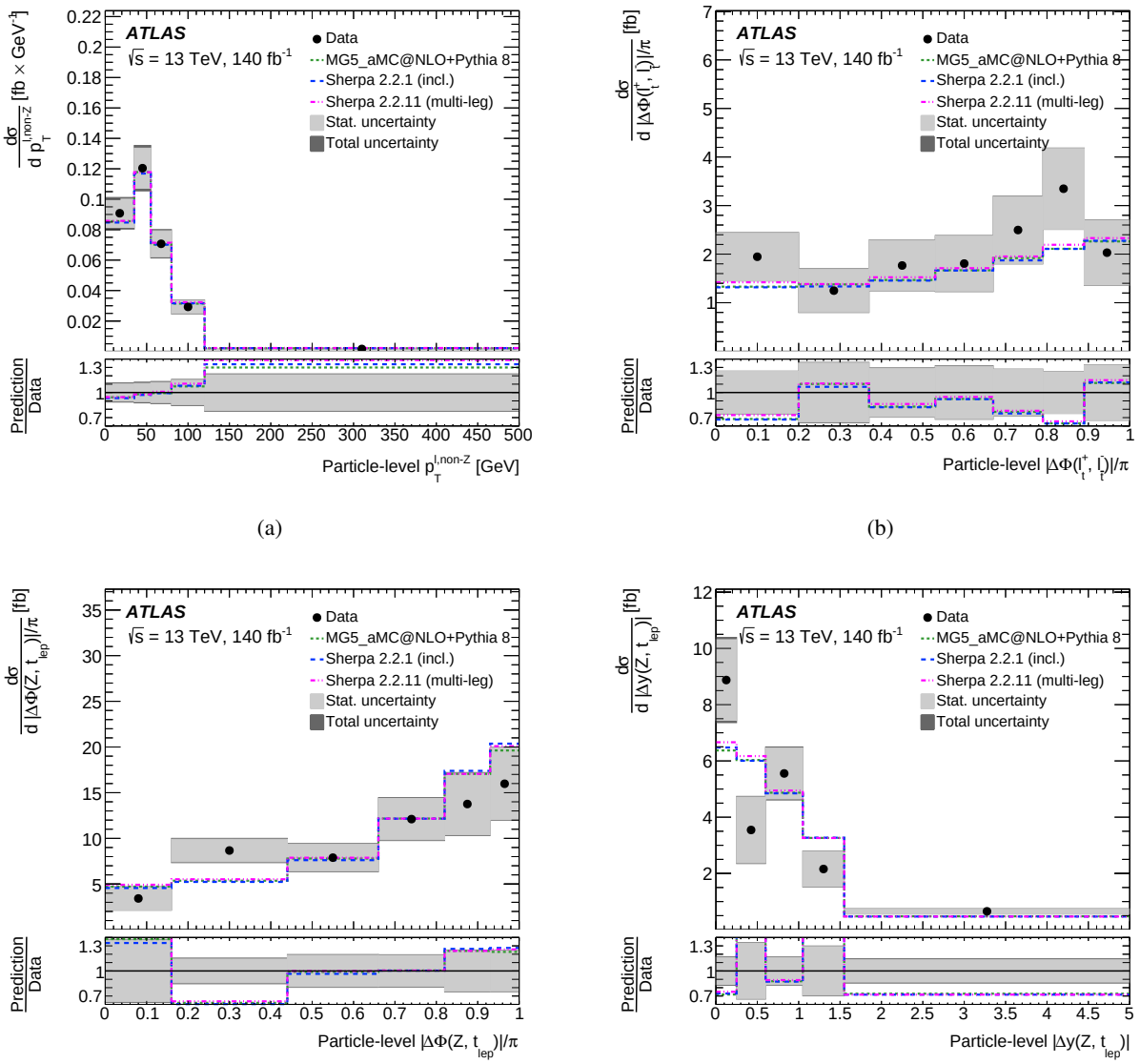

(a) (b)

(c) (d)

Figure 10: Absolute differential cross-section measurements, unfolded to particle level, as a function of (a) $p_{\mathrm{T}}^{\ell,\mathrm{non}\text{-}Z}$ in the 3ℓ channel, (b) $|\Delta\Phi(\ell_t^+, \ell_{\bar{t}}^-)|$ in the 4ℓ channel, (c) $|\Delta\Phi(Z, t_{\mathrm{lep}})|/\pi$ and (d) $|\Delta y(Z, t_{\mathrm{lep}})|$ in the 3ℓ channel. The dark grey band corresponds to the total uncertainty of the measurement; in some cases, it is almost fully covered by the light grey band, representing the dominant statistical uncertainty. Alternative generator predictions are overlaid as additional coloured lines.

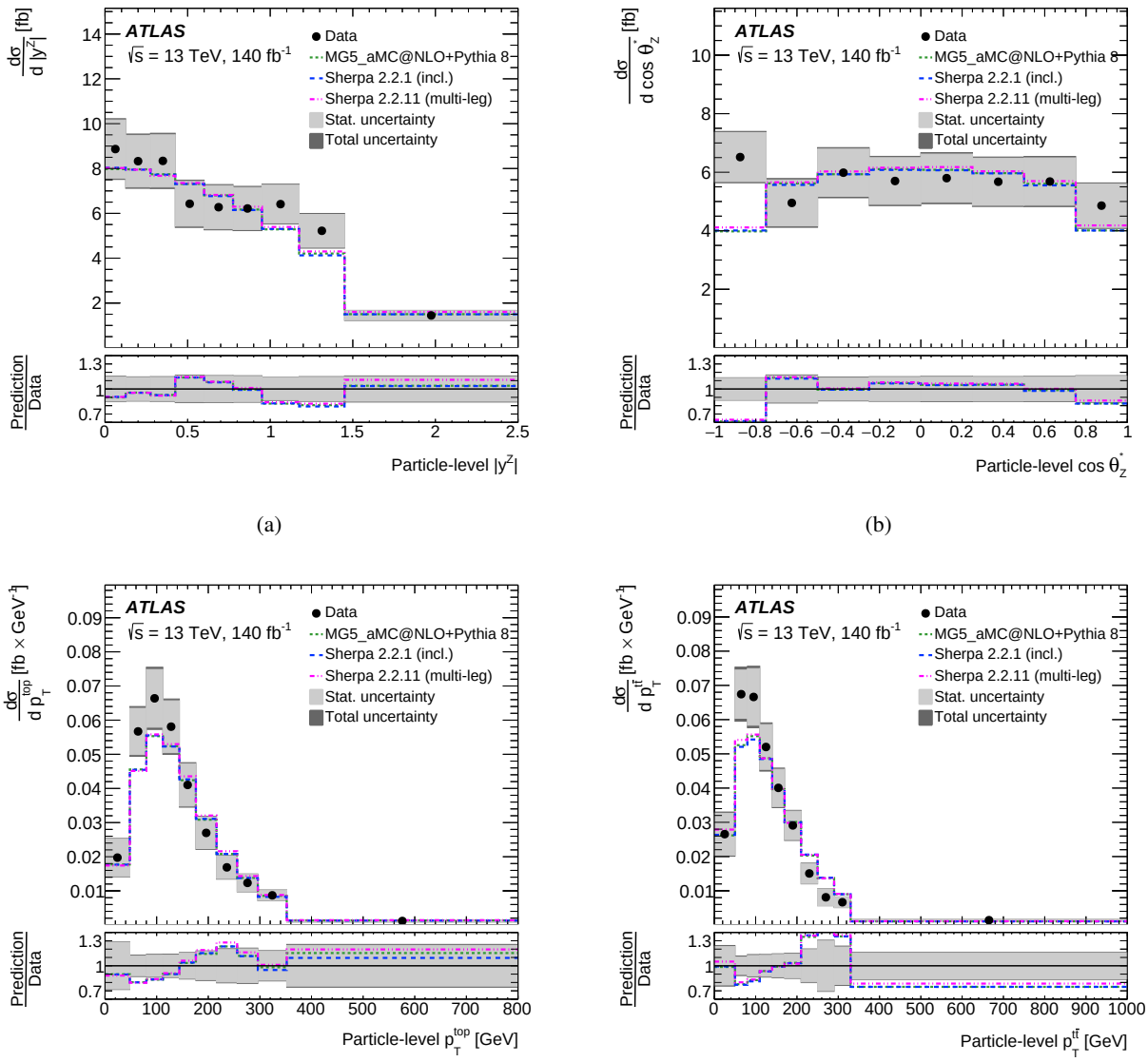

Figure 11: Absolute differential cross-section measurements, unfolded to particle level in the combined 3ℓ and 4ℓ channels, as a function of (a) $|y^Z|$, (b) $\cos\theta^*_Z$, (c) p^t_{T}, and (d) $p^{t\bar{t}}_{\mathrm{T}}$. The dark grey band corresponds to the total uncertainty of the measurement; in some cases, it is almost fully covered by the light grey band, representing the dominant statistical uncertainty. Alternative generator predictions are overlaid as additional coloured lines.

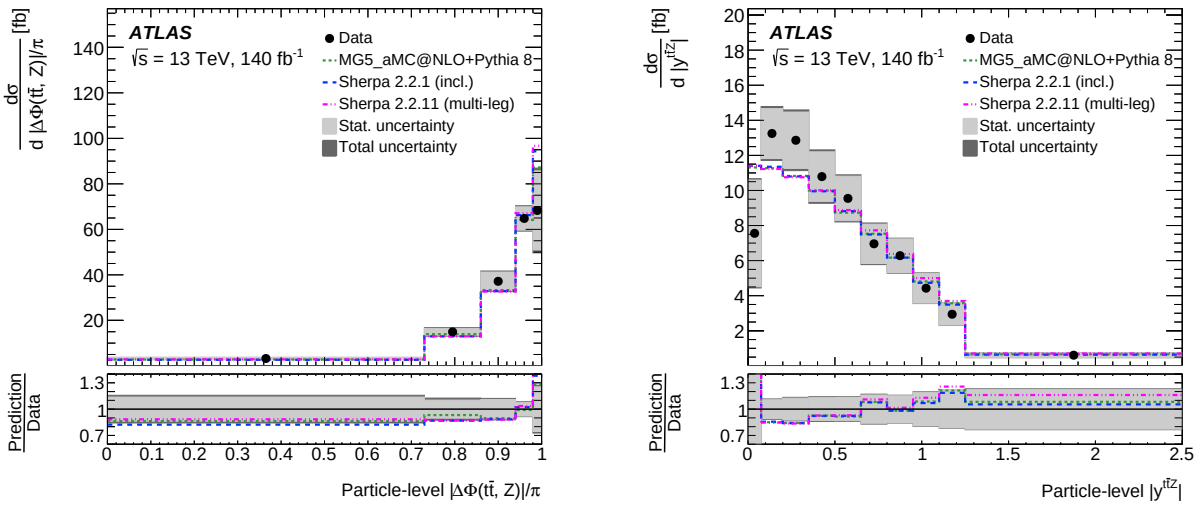

Figure 12: Absolute differential cross-section measurements, unfolded to particle level in the combined 3ℓ and 4ℓ channels, as a function of (a) $|\Delta\Phi(t\bar{t}, Z)|/\pi$, (b) $|y^{t\bar{t}Z}|$, (c) $m^{t\bar{t}Z}$, and (d) $m^{t\bar{t}}$. The dark grey band corresponds to the total uncertainty of the measurement; in some cases, it is almost fully covered by the light grey band, representing the dominant statistical uncertainty. Alternative generator predictions are overlaid as additional coloured lines.

10 Spin-correlation interpretation

The first search for top-quark spin correlations in $t\bar{t}Z$ events is presented, using detector-level distributions. Following the work in Ref. [27], the helicity (k) axis, transverse (n) axis and r axis in the $t\bar{t}$ rest frame are defined, and the polar angle of the charged lepton or down-type quark from the (anti-)top decay with respect to one of these axes, in the rest frame of its parent (anti-)top quark, is considered as a measure of (anti-)top polarisations and $t\bar{t}$ spin correlations. Six independent observables can thus be defined:

$$\cos\theta_k^+, \quad \cos\theta_k^-, \quad \cos\theta_n^+, \quad \cos\theta_n^-, \quad \cos\theta_r^+, \quad \cos\theta_r^-, \tag{3}$$

where the $\pm$ superscript indicates the sign of the charge of the lepton/quark. As shown in Ref. [27], the coefficients of the spin density matrix can be extracted from the averages of the angular distributions corresponding to the observables listed in Eq. (3). These relations are summarised in Table 16; the c_{ii} components are hereafter referred to as 'spin correlations', the $c_{ij}(i \neq j)$ and c_i components as 'spin cross-correlations', and the $b_i^{\pm}$ components as 'polarisations'. The $t\bar{t}Z$ process, differing from $t\bar{t}$ production not only by the emission of an additional Z boson but also by different fractions of $q\bar{q}$- and qg-initiated production, leads to a different picture of top-quark spin correlations: the three coefficients c_{rr}, c_{kk} and c_{nn} adopt negative values and different magnitudes as in the $t\bar{t}$ case, and a small longitudinal polarisation is induced by the emission of the Z boson, resulting in non-zero $b_r^{\pm}$ and $b_k^{\pm}$ coefficients [27]. Future measurements of the full spin density matrix in $t\bar{t}Z$ production will be able to probe possible CP-violation effects and four-fermion interactions, with sensitivity complementary to $t\bar{t}$ production [112].

Table 16: Coefficients of the spin density matrix and their expressions as averages of angular distributions.

Coefficient	Expression
c_{rr}	$-9\langle\cos\theta_r^+ \cdot \cos\theta_r^-\rangle$
c_{kk}	$-9\langle\cos\theta_k^+ \cdot \cos\theta_k^-\rangle$
c_{nn}	$-9\langle\cos\theta_n^+ \cdot \cos\theta_n^-\rangle$
c_{rk}	$-9\langle\cos\theta_r^+ \cdot \cos\theta_k^- + \cos\theta_r^- \cdot \cos\theta_k^+\rangle$
c_{kn}	$-9\langle\cos\theta_k^+ \cdot \cos\theta_n^- + \cos\theta_k^- \cdot \cos\theta_n^+\rangle$
c_{rn}	$-9\langle\cos\theta_r^+ \cdot \cos\theta_n^- + \cos\theta_r^- \cdot \cos\theta_n^+\rangle$
c_r	$-9\langle\cos\theta_k^+ \cdot \cos\theta_n^- - \cos\theta_k^- \cdot \cos\theta_n^+\rangle$
c_k	$-9\langle\cos\theta_n^+ \cdot \cos\theta_r^- - \cos\theta_n^- \cdot \cos\theta_r^+\rangle$
c_n	$-9\langle\cos\theta_r^+ \cdot \cos\theta_k^- - \cos\theta_r^- \cdot \cos\theta_k^+\rangle$
b_r^+	$3\langle\cos\theta_r^+\rangle$
b_r^-	$3\langle\cos\theta_r^-\rangle$
b_k^+	$3\langle\cos\theta_k^+\rangle$
b_k^-	$3\langle\cos\theta_k^-\rangle$
b_n^+	$3\langle\cos\theta_n^+\rangle$
b_n^-	$3\langle\cos\theta_n^-\rangle$

In the 4ℓ channel, all these observables can be defined in terms of leptons from the $t\bar{t}$ system, while in the 3ℓ channel there is only one lepton that can be used to the define the polarisation observables. In order to access the spin correlations in semileptonic $t\bar{t}$ events, the down-type quark from the hadronic W boson decay must be used. Relying on the ~50% branching ratio of hadronic W boson decays into $c\bar{s}/\bar{c}s$, s-candidates are selected by simultaneously applying b-tagging and b-vetoing to the jets selected by the top reconstruction algorithm as belonging to that W boson: if the jet is b-tagged at least at the 85% WP but

not at the 60% WP, it is considered to be c-tagged, and its companion jet from the W boson is the resulting s-jet. The 3ℓ events where the s-jet cannot be identified in this way are rejected.

A final observable of interest can be constructed in both the 3ℓ and 4ℓ channels: the opening angle between the two charged leptons (charged lepton and s-jet) from the dileptonic (semileptonic) $t\bar{t}$ decay system, where each decay product is first boosted to the rest frame of its respective parent (anti-)top quark. This angle φ is particularly sensitive to spin correlations, and the following three relations hold [27]:

$$\frac{1}{\sigma}\frac{\mathrm{d}\sigma}{\mathrm{d}\cos\varphi} = \frac{1}{2}\left(1 - D\cos\varphi\right), \quad D = -\frac{c_{rr} + c_{kk} + c_{nn}}{3}, \quad D = -3\langle\cos\varphi\rangle.$$

Since the angular observables listed in Table 16 suffer from a small number of events in the 4ℓ channel and, in general, highly non-diagonal migration matrices (since all the observables rely on the precise reconstruction of the top quarks), unfolding these distributions using the profile-likelihood method defined in Section 9 is not possible without a large amount of regularisation. Instead, a detector-level template fit is preferred, comparing two 'spin scenarios':

$$O = f_{\mathrm{SM}} \cdot O_{\text{spin-on}} + (1 - f_{\mathrm{SM}}) \cdot O_{\text{spin-off}}.$$

Each observable O (the 15 coefficients of the spin density matrix and the $\cos\varphi$ distribution) is thus fitted to a linear combination of a 'SM' template (taken from the nominal $t\bar{t}Z$ MC predictions) and a template whose values are those predicted in the absence of any spin correlation or top polarisation. The latter predictions are identically zero for all spin coefficients, and therefore lead to a flat distribution of the $\cos\varphi$ observable. These 'spin-off' predictions at parton level are forward-folded through a migration matrix built from the nominal MC samples to produce corresponding detector-level templates, and are assigned the same uncertainties as the nominal templates. The single parameter of interest, f_{SM}, has a value of 0 in the absence of spin correlations and 1 in case of perfect agreement of the unfolded data with the SM.

Since some parameters of the $t\bar{t}Z$ spin correlation matrix are zero within theoretical uncertainties [27], they are excluded from the combined fit in order to improve its stability. The only coefficients predicted to be significantly non-zero in the SM are the three spin correlations (c_{rr}, c_{kk} and c_{nn}), one of the cross-correlations (c_{rk}), four of the polarisations ($b_r^{\pm}$ and $b_k^{\pm}$), and D. Each observable is defined and measured in the combined 3ℓ and 4ℓ channels. The strategy outlined above results in the extraction of nine different values of f_{SM} at detector level, which are then combined in a profiled χ^2-fit. The fit fully takes into account the statistical overlap in the data, as well as the correlations between the NPs from the different measurements of f_{SM}.

The expected and observed values of f_{SM} for each individual detector-level template fit to a single angular distribution are given in Table 17. For each individual measurement, it is checked that the fit does not exhibit any strong pull or constraint on the nuisance parameters, compared to the inclusive cross-section measurement presented in Section 8, and the values are found to be consistent with the SM within uncertainties.

Using the covariance matrices, impacts and correlations of all NPs from each fit, these extracted values of f_{SM} are combined following the statistical prescriptions described above, and yield:

$$f_{\mathrm{SM}}^{\text{obs.}} = 1.20 \pm 0.63\ (\text{stat.}) \pm 0.25\ (\text{syst.}) = 1.20 \pm 0.68\ (\text{tot.}).$$

The measured value agrees with the SM expectation, disfavouring the no-spin hypothesis with a significance of 1.8σ, and is dominated by the statistical uncertainty. The main systematic uncertainties arise from the

signal and background modelling, as well as the impact of $E_{\mathrm{T}}^{\mathrm{miss}}$ and flavour-tagging uncertainties on the reconstruction of the full $t\bar{t}$ system.

Table 17: Values of the f_{SM} parameter extracted from the detector-level template fits to the angular distributions listed in Table 16. The 'observed' values refer to measurements in data, whereas the 'expected' values are obtained from an Asimov dataset (with $f_{\mathrm{SM}} = 1$). The total errors quoted for each measurement include both the statistical uncertainty and the systematic uncertainties from all sources.

Distribution	Channel	Expected values	Observed values
$\cos\varphi$	$3\ell + 4\ell$	$1^{+1.39}_{-1.38}$	$-0.09^{+1.34}_{-1.28}$
$\cos\theta_r^+ \cdot \cos\theta_r^-$	$3\ell + 4\ell$	$1^{+1.83}_{-1.82}$	$1.17^{+1.80}_{-1.76}$
$\cos\theta_k^+ \cdot \cos\theta_k^-$	$3\ell + 4\ell$	$1^{+1.78}_{-1.78}$	$1.39^{+1.72}_{-1.73}$
$\cos\theta_n^+ \cdot \cos\theta_n^-$	$3\ell + 4\ell$	$1^{+1.87}_{-1.86}$	$-1.05^{+2.06}_{-1.96}$
$\cos\theta_r^+ \cdot \cos\theta_k^- + \cos\theta_r^- \cdot \cos\theta_k^+$	$3\ell + 4\ell$	$1^{+1.93}_{-1.93}$	$0.36^{+1.99}_{-1.93}$
$\cos\theta_r^+$	$3\ell + 4\ell$	$1^{+1.81}_{-1.80}$	$1.56^{+1.86}_{-1.98}$
$\cos\theta_r^-$	$3\ell + 4\ell$	$1^{+1.82}_{-1.78}$	$1.81^{+1.63}_{-1.68}$
$\cos\theta_k^+$	$3\ell + 4\ell$	$1^{+1.69}_{-1.67}$	$2.00^{+1.65}_{-1.70}$
$\cos\theta_k^-$	$3\ell + 4\ell$	$1^{+1.68}_{-1.68}$	$2.31^{+1.68}_{-1.68}$

11 SMEFT interpretation

The Standard Model effective field theory (SMEFT) [25, 26] provides a complete phenomenological extension of the SM beyond dimension-4 terms in the Lagrangian. By employing the degrees of freedom and gauge symmetries of the SM, the SMEFT builds an infinite series of operators sorted by canonical dimension. New physics effects from BSM theories characterised by a mass scale higher than the energies probed in a typical LHC collision can therefore be related to a set of operators $\{Q\}$, together with their Wilson coefficients $\{C\}$. Observed deviations from the SM can then be expressed in terms of $\{C\}$, without specifying a particular BSM model. Similarly, LHC data found to be in agreement with the SM lead to constraints in the phenomenological space spanned by the Wilson coefficients $\{C\}$, which in turn can be translated into exclusions of various BSM scenarios. The Lagrangian of the SMEFT thus reads:

$$\mathcal{L}_{\mathrm{SMEFT}} = \mathcal{L}_{\mathrm{SM}} + \sum_{d>4} \mathcal{L}^{(d)}, \quad \mathcal{L}^{(d)} = \sum_{i=1}^{n_d} \frac{C_i^{(d)}}{\Lambda^{d-4}} Q_i^{(d)},$$

where Λ is a suitable cut-off scale, chosen as the conventional $\Lambda = 1$ TeV in this analysis. The number of such operators $Q^{(d)}$, n_d, is known up to $d = 8$, but current computational tools only allow the study of SMEFT effects up to $d = 6$ where generation of LHC-like collision events is required. Operators contributing to $\mathcal{L}^{(5)}$ are known to include baryon- and lepton-number violating terms, and are therefore ignored in this analysis; similarly, higher-order operators are Λ-suppressed, so only $\mathcal{L}^{(6)}$ is considered in the following.

Using the EFT Monte Carlo samples described in Section 3 (produced with the SMEFTsim 3.0 UFO model [26]), the dependence of a generic observable O (e.g. an inclusive or differential cross section) on a set of Wilson coefficients $\{C\}$ can be parameterised as:

$$O = O_{\text{SM}} + \sum_i C_i A_i + \sum_{i,j} C_i C_j B_{ij}. \tag{4}$$

The reweighting approach taken in the generation of these MC samples probes multiple values of the individual Wilson coefficients per event, as well as pairs of coefficients. A simple quadratic fit to any observable of interest therefore yields the linear term A_i, which represents the interference between the SM and the SMEFT, and the quadratic term B_{ij}, which represents a pure SMEFT contribution.[14]

In order to remove possible discrepancies between the SMEFT prediction of the SM term O_{SM}, obtained at LO in QCD ($O_{\text{SM}}^{\text{LO}}$), and the observed $t\bar{t}Z$ data, the SMEFT predictions for the observables are scaled by a factor $O_{\text{SM}}^{\text{NLO}}/O_{\text{SM}}^{\text{LO}}$, where $O_{\text{SM}}^{\text{NLO}}$ is instead obtained from the modelling of the nominal MadGraph5_aMC@NLO+Pythia 8 $t\bar{t}Z$ sample.

The SMEFT predictions rely on the top-flavour structure of the SMEFTsim 3.0 model, which is defined by the following assumptions:

- quarks of the first two generations and quarks of the third are described by independent fields, denoted by (q, u, d) and (Q, t, b) respectively;
- a symmetry $U(2)^3 = U(2)_q \times U(2)_u \times U(2)_d$ is imposed on the Lagrangian, under which only the light quarks transform (e.g. $q \mapsto \Omega_q q$, but $t \mapsto t$);
- mixing effects in the quark sector are neglected (the CKM matrix is unity);
- a symmetry $U(1)^3_{l+e} = U(1)_e \times U(1)_\mu \times U(1)_\tau$ is imposed on the Lagrangian, which corresponds to simple flavour diagonality in the lepton sector.

In this analysis, 20 dimension-6 SMEFT operators are considered, corresponding to 23 degrees of freedom (3 Wilson coefficients have a distinct imaginary part). They are defined in Table 18, and broadly fall into two classes: top–boson operators (classes 5 and 6 in the notation of Ref. [26]) and four-quark operators (classes 8a-c). The $t\bar{t}Z$ vertex is sensitive to particular combinations of some operators, which are made explicit in other models (such as dim6top [113]):

$$\begin{aligned} c_{tZ} &= -\sin\theta_W C_{tB} + \cos\theta_W C_{tW}, \\ c^-_{\varphi Q} &= C^{(1)}_{HQ} - C^{(3)}_{HQ}, \end{aligned} \tag{5}$$

where the operators on the left-hand side are in the notation of Ref. [113], and θ_W is the Weinberg angle. It is shown in the following that the above relations can be recovered by identifiying the directions in the EFT phase-space that are probed by this measurement.

[14] In what follows, the 'pure quadratic' and 'cross' terms may be referred to, meaning B_{ii} and $B_{ij,i\neq j}$ respectively.

Table 18: Definitions of the relevant dimension-6 SMEFT operators. For the three top–boson operators indicated with a ($\star$) the real and imaginary parts of the corresponding Wilson coefficients are considered separately.

	Operator	Definition	
top–boson	O_{tW}	$(\bar{Q}\sigma^{\mu\nu}t)\sigma^i\tilde{H}W^i_{\mu\nu}$	($\star$)
	O_{tB}	$(\bar{Q}\sigma^{\mu\nu}t)\tilde{H}B_{\mu\nu}$	($\star$)
	O_{tG}	$(\bar{Q}\sigma^{\mu\nu}T^a t)\tilde{H}G^a_{\mu\nu}$	($\star$)
	$O^{(1)}_{HQ}$	$(H^\dagger i\overleftrightarrow{D}_\mu H)(\bar{Q}\gamma^\mu Q)$	
	$O^{(3)}_{HQ}$	$(H^\dagger i\overleftrightarrow{D}^i_\mu H)(\bar{Q}\sigma^i\gamma^\mu Q)$	
	O_{Ht}	$(H^\dagger i\overleftrightarrow{D}_\mu H)(\bar{t}\gamma^\mu t)$	
four-quark	$O^{(1)}_{tu}$	$(\bar{t}\gamma_\mu t)(\bar{u}\gamma^\mu u)$	
	$O^{(8)}_{tu}$	$(\bar{t}T^a\gamma_\mu t)(\bar{u}T^a\gamma^\mu u)$	
	$O^{(1)}_{td}$	$(\bar{t}\gamma_\mu t)(\bar{d}\gamma^\mu d)$	
	$O^{(8)}_{td}$	$(\bar{t}T^a\gamma_\mu t)(\bar{d}T^a\gamma^\mu d)$	
	$O^{(1)}_{qt}$	$(\bar{q}\gamma_\mu q)(\bar{t}\gamma^\mu t)$	
	$O^{(8)}_{qt}$	$(\bar{q}T^a\gamma_\mu q)(\bar{t}T^a\gamma^\mu t)$	
	$O^{(1)}_{Qu}$	$(\bar{Q}\gamma_\mu Q)(\bar{u}\gamma^\mu u)$	
	$O^{(8)}_{Qu}$	$(\bar{Q}T^a\gamma_\mu Q)(\bar{u}T^a\gamma^\mu u)$	
	$O^{(1)}_{Qd}$	$(\bar{Q}\gamma_\mu Q)(\bar{d}\gamma^\mu d)$	
	$O^{(8)}_{Qd}$	$(\bar{Q}T^a\gamma_\mu Q)(\bar{d}T^a\gamma^\mu d)$	
	$O^{(1,1)}_{Qq}$	$(\bar{Q}\gamma_\mu Q)(\bar{q}\gamma^\mu q)$	
	$O^{(3,1)}_{Qq}$	$(\bar{Q}\sigma^i\gamma_\mu Q)(\bar{q}\sigma^i\gamma^\mu q)$	
	$O^{(1,8)}_{Qq}$	$(\bar{Q}T^a\gamma_\mu Q)(\bar{q}T^a\gamma^\mu q)$	
	$O^{(3,8)}_{Qq}$	$(\bar{Q}\sigma^i T^a\gamma_\mu Q)(\bar{q}\sigma^i T^a\gamma^\mu q)$	

Several different fitting scenarios are employed to extract as much information from the data as possible, in a self-consistent way. Each fit is performed in the on-shell $t\bar{t}Z$ fiducial region (combination of the 3ℓ and 4ℓ channels), separately for the top–boson and four-quark operators of Table 18. The differential distributions unfolded to particle level in Section 9.4 are parameterised in terms of these EFT operators, and taken as joint input measurements for the EFT interpretation. This detailed analysis of a single process provides a self-contained alternative to simultaneously fitting multiple $t\bar{t}+X$ processes, such as recently reported by CMS [114].

For both the top–boson and four-quark categories of operators, a nominal full quadratic fit using both the linear and pure quadratic terms as well as the cross terms of the parameterisation shown in Eq. (4) is performed for all operators simultaneously. Secondly, a fit where only the linear terms are present

provides an approximate measure of the importance of the interference terms when compared with the full quadratic fit. Full quadratic fits are also performed for each operator individually, where only a single Wilson coefficient is probed while all others are fixed to zero, in order to provide results which can be compared with those of other analyses.

Finally, following the work in Ref. [115], the inverse covariance matrix of the unfolded measurements is rotated into the space of the Wilson coefficients $\{C\}$ (top–boson and four-quark operators together), considering only the linear SM/EFT interferences. The resulting matrix provides a lower bound on the Fisher information matrix. Its eigenvectors correspond to the directions in the space of Wilson coefficients probed by the measurements, with the corresponding eigenvalues providing a measure of the sensitivity achieved along these directions. The inverse of the square root of an eigenvalue can be understood as a predictor of the limit that would be obtained when fitting the linear combination of operators defined by the eigenvector, rather than the individual operators themselves. Only the eigenvectors whose eigenvalues are greater than 0.1 are considered, corresponding to a truncation of expected limits greater than $\sim\pi$, beyond the natural range of the Wilson coefficients of $O(1)$ and the range of validity of the linear approximation.

A multimodal Gaussian likelihood function is implemented with the EFTfitter tool [116], relying on the BAT.jl package [117], to perform the EFT interpretation in a Bayesian statistical framework. The overlap in data between the different measurements is suitably taken into account via correlation matrices. The results of the various EFT fits described above are presented in Figure 13 for the two scenarios with either only top–boson operators or only four-quark operators, taking as input measurements the fiducial $t\bar{t}Z$ cross section and the following normalised differential distributions defined in the combined 3ℓ and 4ℓ channels at particle level: p_{T}^{Z}, $|y^{Z}|$, $\cos\theta_{Z}^{*}$, p_{T}^{t}, $|\Delta\Phi(t\bar{t},Z)|$ and $|y^{t\bar{t}Z}|$. Of these, p_{T}^{Z} is typically the most sensitive to top–Z operators, whereas p_{T}^{t} is particularly relevant for constraining four-quark operators. The corresponding numerical values are reported in Tables 19 and 20. A uniform prior in the range $[-10, 10]$ is used in every case. The independent fits, where all Wilson coefficients other than the one considered are set to zero, offer the tightest constraints, typically $|C|/\Lambda^2 \lesssim 0.5$ TeV^{-2} in 95% credible intervals.

The quadratic fits, capturing the full EFT picture at dimension 6, also show competitive constraints in the range $|C|/\Lambda^2 \lesssim 0.5{-}1$ TeV^{-2} for 95% credible intervals. Some of the operators are observed to feature slightly asymmetric limits or non-zero global modes (but are still compatible with the SM within their 1σ range); this pattern is a consequence of the interplay between the different operators in the global fit, as they do not all represent directions in the EFT space that can be individually probed by the various input measurements.

This pattern is also present in the linearised global fit, which can be used to gauge the relative importance of the SM/EFT interference terms. For some operators (e.g. the imaginary and CP-violating parts of C_{tG}, C_{tW} and C_{tB}, or most of the colour-singlet four-quark operators), the results of the linear fits are not quoted since the corresponding interference term vanishes at LO in QCD. As expected, $\Re[C_{tG}]$ and the top–Z operators $C_{HQ}^{(1)}$, $C_{HQ}^{(3)}$ and C_{Ht} have strong linear contributions; the inclusion of their pure EFT contributions in the quadratic fit, however, leads to constraints that are tighter by a factor of 2–4. The real parts of the C_{tW} and C_{tB} operators, giving rise to weak dipole moments in the top quark, have comparatively smaller linear terms: the typically soft Z-boson emission produces a momentum suppression, and there is an accidental cancellation between the $q\bar{q}$- and gg-initiated channels [118]. On the other hand, while four-quark operators can interfere with SM $t\bar{t}Z$ diagrams, the predominance of the $gg \to t\bar{t}Z$ production channel at the LHC drastically reduces the linearised limits when introducing pure EFT contributions in the quadratic fit: e.g. for $C_{Qq}^{(3,1)}$ and $C_{Qq}^{(3,8)}$, these effects produce improvements by factors of 6–30.

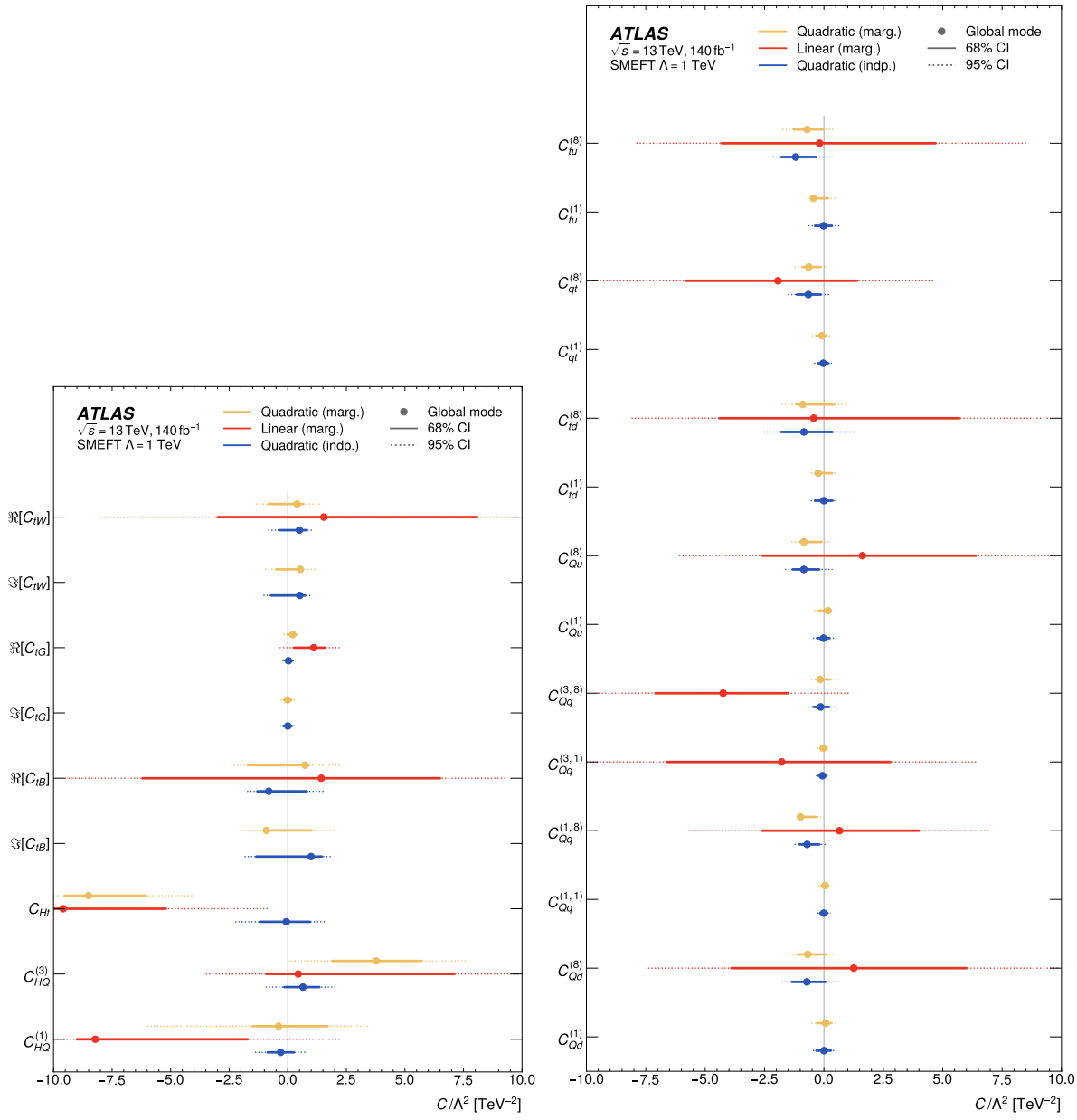

(a) (b)

Figure 13: Comparison of the 68% and 95% credible intervals obtained in the (a) top–boson scenario and (b) four-quark scenario for the marginalised linear and quadratic fits, as well as the independent quadratic fit. The imaginary (CP-violating) part of the C_{tW} and C_{tB} operators, as well as the colour-singlet four-quark operator, have no interference with the SM at leading order: no linear fit (red) is performed. Also shown are the best-fit values (global mode) for each operator.

Table 19: Observed and expected 68% and 95% credible intervals for the top–boson operators, comparing the results obtained from the marginalised linear and quadratic fits, as well as the independent quadratic fit. Also shown are the best-fit values (global mode) for each operator.

Wilson coefficient		68% CI (exp.)	95% CI (exp.)	68% CI (obs.)	95% CI (obs.)	Best-fit
$C_{HQ}^{(1)}$	$O(\Lambda^{-2})$ (marg.)	$[-5.1, 5.4]$	$[-8.9, 8.7]$	$[-9.0, -1.7]$	$[-10, 2.3]$	-8
	$O(\Lambda^{-4})$ (marg.)	$[-1.2, 1.8]$	$[-3.1, 4.7]$	$[-1.5, 1.7]$	$[-6.0, 3.5]$	-0.4
	$O(\Lambda^{-4})$ (indep.)	$[-0.58, 0.56]$	$[-1.1, 1.1]$	$[-0.86, 0.26]$	$[-1.4, 0.84]$	-0.3
$C_{HQ}^{(3)}$	$O(\Lambda^{-2})$ (marg.)	$[-4.7, 4.7]$	$[-8.5, 8.4]$	$[-0.90, 7.1]$	$[-3.5, 9.9]$	0.5
	$O(\Lambda^{-4})$ (marg.)	$[-1.1, 2.6]$	$[-2.8, 4.4]$	$[1.9, 5.7]$	$[0, 7.7]$	4
	$O(\Lambda^{-4})$ (indep.)	$[-0.85, 0.75]$	$[-1.6, 1.4]$	$[-0.15, 1.3]$	$[-0.95, 2.0]$	0.7
C_{Ht}	$O(\Lambda^{-2})$ (marg.)	$[-4.3, 4.2]$	$[-7.9, 8.1]$	$[-10, -5.2]$	$[-10, -0.80]$	-10
	$O(\Lambda^{-4})$ (marg.)	$[-4.0, 0.90]$	$[-6.1, 3.5]$	$[-9.5, -6.0]$	$[-10, -4.0]$	-9
	$O(\Lambda^{-4})$ (indep.)	$[-1.0, 0.95]$	$[-2.0, 1.7]$	$[-1.2, 0.95]$	$[-2.2, 1.6]$	-0.06
$\Im[C_{tB}]$	$O(\Lambda^{-2})$ (marg.)	—	—	—	—	—
	$O(\Lambda^{-4})$ (marg.)	$[-0.84, 1.0]$	$[-1.6, 1.7]$	$[-0.80, 1.0]$	$[-2.0, 2.0]$	-0.9
	$O(\Lambda^{-4})$ (indep.)	$[-1.0, 1.0]$	$[-1.6, 1.6]$	$[-1.4, 1.5]$	$[-1.9, 1.9]$	1
$\Re[C_{tB}]$	$O(\Lambda^{-2})$ (marg.)	$[-6.7, 6.7]$	$[-9.3, 9.7]$	$[-6.2, 6.5]$	$[-9.5, 9.3]$	1
	$O(\Lambda^{-4})$ (marg.)	$[-1.3, 0.90]$	$[-2.3, 2.0]$	$[-1.7, 0.90]$	$[-2.5, 2.3]$	0.7
	$O(\Lambda^{-4})$ (indep.)	$[-1.0, 0.92]$	$[-1.6, 1.6]$	$[-1.3, 0.82]$	$[-1.7, 1.6]$	-0.8
$\Im[C_{tG}]$	$O(\Lambda^{-2})$ (marg.)	—	—	—	—	—
	$O(\Lambda^{-4})$ (marg.)	$[-0.19, 0.17]$	$[-0.32, 0.32]$	$[-0.16, 0.16]$	$[-0.30, 0.31]$	-0.01
	$O(\Lambda^{-4})$ (indep.)	$[-0.22, 0.22]$	$[-0.36, 0.36]$	$[-0.19, 0.18]$	$[-0.32, 0.33]$	0
$\Re[C_{tG}]$	$O(\Lambda^{-2})$ (marg.)	$[-0.70, 0.70]$	$[-1.4, 1.3]$	$[0.25, 1.6]$	$[-0.35, 2.2]$	1
	$O(\Lambda^{-4})$ (marg.)	$[-0.11, 0.23]$	$[-0.27, 0.38]$	$[-0.015, 0.32]$	$[-0.18, 0.43]$	0.2
	$O(\Lambda^{-4})$ (indep.)	$[-0.14, 0.21]$	$[-0.26, 0.36]$	$[-0.11, 0.20]$	$[-0.23, 0.34]$	0.03
$\Im[C_{tW}]$	$O(\Lambda^{-2})$ (marg.)	—	—	—	—	—
	$O(\Lambda^{-4})$ (marg.)	$[-0.56, 0.56]$	$[-1.1, 1.1]$	$[-0.48, 0.62]$	$[-0.98, 1.2]$	0.5
	$O(\Lambda^{-4})$ (indep.)	$[-0.56, 0.56]$	$[-0.92, 0.92]$	$[-0.72, 0.74]$	$[-1.0, 1.0]$	0.5
$\Re[C_{tW}]$	$O(\Lambda^{-2})$ (marg.)	$[-5.8, 5.9]$	$[-9.4, 9.7]$	$[-3.0, 8.1]$	$[-8.0, 9.9]$	2
	$O(\Lambda^{-4})$ (marg.)	$[-0.72, 0.60]$	$[-1.3, 1.3]$	$[-0.82, 0.66]$	$[-1.3, 1.5]$	0.4
	$O(\Lambda^{-4})$ (indep.)	$[-0.52, 0.60]$	$[-0.88, 0.92]$	$[-0.38, 0.80]$	$[-0.84, 1.0]$	0.5

Table 20: Observed and expected 68% and 95% credible intervals for the four-quark operators, comparing the results obtained from the marginalised linear and quadratic fits, as well as the independent quadratic fit. Also shown are the best-fit values (global mode) for each operator.

Wilson coefficient		68% CI (exp.)	95% CI (exp.)	68% CI (obs.)	95% CI (obs.)	Best-fit
$C_{Qd}^{(1)}$	$\mathcal{O}(\Lambda^{-2})$ (marg.)	—	—	—	—	—
	$\mathcal{O}(\Lambda^{-4})$ (marg.)	$[-0.31, 0.32]$	$[-0.54, 0.55]$	$[-0.28, 0.29]$	$[-0.52, 0.53]$	0.07
	$\mathcal{O}(\Lambda^{-4})$ (indep.)	$[-0.39, 0.37]$	$[-0.56, 0.56]$	$[-0.32, 0.29]$	$[-0.47, 0.46]$	0
$C_{Qd}^{(8)}$	$\mathcal{O}(\Lambda^{-2})$ (marg.)	$[-4.8, 5.0]$	$[-8.7, 8.6]$	$[-3.9, 6.0]$	$[-7.4, 9.9]$	1
	$\mathcal{O}(\Lambda^{-4})$ (marg.)	$[-0.90, 0.34]$	$[-1.5, 0.82]$	$[-1.1, 0.060]$	$[-1.5, 0.46]$	-0.7
	$\mathcal{O}(\Lambda^{-4})$ (indep.)	$[-1.4, 0.50]$	$[-2.0, 1.1]$	$[-1.4, 0.060]$	$[-1.8, 0.62]$	-0.7
$C_{Qq}^{(1,1)}$	$\mathcal{O}(\Lambda^{-2})$ (marg.)	—	—	—	—	—
	$\mathcal{O}(\Lambda^{-4})$ (marg.)	$[-0.14, 0.17]$	$[-0.29, 0.30]$	$[-0.11, 0.17]$	$[-0.24, 0.30]$	0.05
	$\mathcal{O}(\Lambda^{-4})$ (indep.)	$[-0.21, 0.21]$	$[-0.34, 0.34]$	$[-0.17, 0.16]$	$[-0.29, 0.29]$	-0.01
$C_{Qq}^{(1,8)}$	$\mathcal{O}(\Lambda^{-2})$ (marg.)	$[-3.3, 3.3]$	$[-6.6, 6.5]$	$[-2.6, 4.0]$	$[-5.7, 7.0]$	0.7
	$\mathcal{O}(\Lambda^{-4})$ (marg.)	$[-0.72, -0.090]$	$[-1.0, 0.19]$	$[-0.89, -0.29]$	$[-1.1, -0.030]$	-1
	$\mathcal{O}(\Lambda^{-4})$ (indep.)	$[-0.76, 0.28]$	$[-1.3, 0.40]$	$[-1.0, -0.19]$	$[-1.2, 0.080]$	-0.7
$C_{Qq}^{(3,1)}$	$\mathcal{O}(\Lambda^{-2})$ (marg.)	$[-4.9, 5.0]$	$[-8.6, 8.8]$	$[-6.6, 2.8]$	$[-10, 6.5]$	-2
	$\mathcal{O}(\Lambda^{-4})$ (marg.)	$[-0.18, 0.13]$	$[-0.32, 0.26]$	$[-0.17, 0.12]$	$[-0.29, 0.24]$	-0.03
	$\mathcal{O}(\Lambda^{-4})$ (indep.)	$[-0.26, 0.18]$	$[-0.41, 0.31]$	$[-0.23, 0.11]$	$[-0.34, 0.23]$	-0.06
$C_{Qq}^{(3,8)}$	$\mathcal{O}(\Lambda^{-2})$ (marg.)	$[-2.9, 2.9]$	$[-5.7, 5.8]$	$[-7.1, -1.5]$	$[-9.5, 1.1]$	-4
	$\mathcal{O}(\Lambda^{-4})$ (marg.)	$[-0.31, 0.29]$	$[-0.57, 0.55]$	$[-0.29, 0.25]$	$[-0.54, 0.48]$	-0.2
	$\mathcal{O}(\Lambda^{-4})$ (indep.)	$[-0.42, 0.48]$	$[-0.74, 0.76]$	$[-0.44, 0.22]$	$[-0.68, 0.54]$	-0.1
$C_{Qu}^{(1)}$	$\mathcal{O}(\Lambda^{-2})$ (marg.)	—	—	—	—	—
	$\mathcal{O}(\Lambda^{-4})$ (marg.)	$[-0.26, 0.24]$	$[-0.46, 0.44]$	$[-0.22, 0.24]$	$[-0.42, 0.43]$	0.2
	$\mathcal{O}(\Lambda^{-4})$ (indep.)	$[-0.37, 0.35]$	$[-0.59, 0.56]$	$[-0.29, 0.24]$	$[-0.47, 0.43]$	-0.02
$C_{Qu}^{(8)}$	$\mathcal{O}(\Lambda^{-2})$ (marg.)	$[-4.7, 4.6]$	$[-8.4, 8.5]$	$[-2.6, 6.4]$	$[-6.1, 9.9]$	2
	$\mathcal{O}(\Lambda^{-4})$ (marg.)	$[-0.82, 0.18]$	$[-1.3, 0.60]$	$[-1.0, -0.10]$	$[-1.4, 0.27]$	-0.8
	$\mathcal{O}(\Lambda^{-4})$ (indep.)	$[-1.2, 0.34]$	$[-1.7, 0.80]$	$[-1.3, -0.20]$	$[-1.6, 0.36]$	-0.8
$C_{qt}^{(1)}$	$\mathcal{O}(\Lambda^{-2})$ (marg.)	—	—	—	—	—
	$\mathcal{O}(\Lambda^{-4})$ (marg.)	$[-0.28, 0.16]$	$[-0.47, 0.34]$	$[-0.32, 0.080]$	$[-0.51, 0.27]$	-0.08
	$\mathcal{O}(\Lambda^{-4})$ (indep.)	$[-0.31, 0.27]$	$[-0.50, 0.45]$	$[-0.24, 0.19]$	$[-0.42, 0.36]$	-0.03
$C_{qt}^{(8)}$	$\mathcal{O}(\Lambda^{-2})$ (marg.)	$[-3.6, 3.6]$	$[-7.1, 7.1]$	$[-5.8, 1.4]$	$[-10, 4.6]$	-2
	$\mathcal{O}(\Lambda^{-4})$ (marg.)	$[-0.68, 0.080]$	$[-1.1, 0.36]$	$[-0.88, -0.15]$	$[-1.2, 0.12]$	-0.6
	$\mathcal{O}(\Lambda^{-4})$ (indep.)	$[-0.90, 0.36]$	$[-1.6, 0.54]$	$[-1.1, -0.14]$	$[-1.5, 0.22]$	-0.7
$C_{td}^{(1)}$	$\mathcal{O}(\Lambda^{-2})$ (marg.)	—	—	—	—	—
	$\mathcal{O}(\Lambda^{-4})$ (marg.)	$[-0.32, 0.38]$	$[-0.53, 0.57]$	$[-0.35, 0.34]$	$[-0.56, 0.54]$	-0.2
	$\mathcal{O}(\Lambda^{-4})$ (indep.)	$[-0.62, 0.64]$	$[-1.0, 1.0]$	$[-0.38, 0.36]$	$[-0.56, 0.56]$	0
$C_{td}^{(8)}$	$\mathcal{O}(\Lambda^{-2})$ (marg.)	$[-5.0, 5.1]$	$[-8.9, 8.8]$	$[-4.4, 5.7]$	$[-8.1, 9.5]$	-0.4
	$\mathcal{O}(\Lambda^{-4})$ (marg.)	$[-1.0, 0.68]$	$[-1.8, 1.3]$	$[-1.1, 0.42]$	$[-1.8, 0.94]$	-0.9
	$\mathcal{O}(\Lambda^{-4})$ (indep.)	$[-1.8, 0.85]$	$[-2.8, 1.7]$	$[-1.8, 0.35]$	$[-2.5, 1.2]$	-0.8
$C_{tu}^{(1)}$	$\mathcal{O}(\Lambda^{-2})$ (marg.)	—	—	—	—	—
	$\mathcal{O}(\Lambda^{-4})$ (marg.)	$[-0.31, 0.34]$	$[-0.59, 0.63]$	$[-0.44, 0.17]$	$[-0.70, 0.47]$	-0.4
	$\mathcal{O}(\Lambda^{-4})$ (indep.)	$[-0.46, 0.46]$	$[-0.76, 0.76]$	$[-0.38, 0.34]$	$[-0.66, 0.64]$	-0.01
$C_{tu}^{(8)}$	$\mathcal{O}(\Lambda^{-2})$ (marg.)	$[-4.6, 4.4]$	$[-8.4, 8.2]$	$[-4.3, 4.7]$	$[-7.9, 8.6]$	-0.2
	$\mathcal{O}(\Lambda^{-4})$ (marg.)	$[-1.0, 0.32]$	$[-1.6, 0.90]$	$[-1.3, -0.040]$	$[-1.8, 0.46]$	-0.7
	$\mathcal{O}(\Lambda^{-4})$ (indep.)	$[-1.6, 0.50]$	$[-2.2, 1.2]$	$[-1.8, -0.32]$	$[-2.2, 0.38]$	-1

The covariance matrix obtained in the linear fit is inverted to yield a lower bound on the underlying Fisher information matrix, and a new linear fit in the rotated EFT directions of sensitivity, as previously described, is performed. The following eigenvectors are extracted, corresponding to eigenvalues larger than 0.1:

$$
\begin{aligned}
\lambda_1 = 40,\ \mathcal{F}_1 : &+ 0.75 \cdot \Re[C_{tG}] + 0.01 \cdot \Re[C_{tW}] + 0.23 \cdot C_{HQ}^{(1)} - 0.15 \cdot C_{HQ}^{(3)} - 0.13 \cdot C_{Ht} - 0.10 \cdot C_{Qd}^{(8)} \\
&- 0.42 \cdot C_{Qq}^{(1,8)} - 0.15 \cdot C_{Qq}^{(3,1)} + 0.06 \cdot C_{Qq}^{(3,8)} - 0.13 \cdot C_{Qu}^{(8)} - 0.05 \cdot C_{td}^{(8)} - 0.33 \cdot C_{qt}^{(8)} - 0.08 \cdot C_{tu}^{(8)}, \\
\lambda_2 = 8,\ \mathcal{F}_2 : &- 0.41 \cdot \Re[C_{tG}] + 0.04 \cdot \Re[C_{tW}] - 0.02 \cdot \Re[C_{tB}] - 0.34 \cdot C_{HQ}^{(1)} + 0.27 \cdot C_{HQ}^{(3)} + 0.18 \cdot C_{Ht} \\
&- 0.12 \cdot C_{Qd}^{(8)} - 0.57 \cdot C_{Qq}^{(1,8)} - 0.22 \cdot C_{Qq}^{(3,1)} - 0.05 \cdot C_{Qq}^{(3,8)} - 0.22 \cdot C_{Qu}^{(8)} - 0.05 \cdot C_{td}^{(8)} - 0.39 \cdot C_{qt}^{(8)} \\
&- 0.12 \cdot C_{tu}^{(8)}, \\
\lambda_3 = 0.5,\ \mathcal{F}_3 : &- 0.07 \cdot \Re[C_{tG}] + 0.06 \cdot \Re[C_{tW}] - 0.01 \cdot \Re[C_{tB}] + 0.18 \cdot C_{HQ}^{(1)} + 0.04 \cdot C_{HQ}^{(3)} - 0.33 \cdot C_{Ht} \\
&- 0.07 \cdot C_{Qd}^{(8)} + 0.13 \cdot C_{Qq}^{(1,8)} + 0.04 \cdot C_{Qq}^{(3,1)} - 0.68 \cdot C_{Qq}^{(3,8)} - 0.42 \cdot C_{Qu}^{(8)} - 0.11 \cdot C_{td}^{(8)} + 0.08 \cdot C_{qt}^{(8)} \\
&- 0.41 \cdot C_{tu}^{(8)}.
\end{aligned}
$$

These relations are also visualised in Figure 14. Of particular interest is the combination $\mathcal{F}_1$, which clearly emerges as the most important direction of SMEFT constraints in the linear fit. It features most prominently the $\Re[C_{tG}]$ operator together with the two four-quark operators $C_{Qq}^{(1,8)}$ and $C_{qt}^{(8)}$ that couple the top-quark field to left-handed light-quark fields, but also involves a non-trivial combination of most of the other operators. From the inverse square root of the eigenvalue λ_1, limits on $\mathcal{F}_1$ are expected to be set at $\sim$0.15 TeV^{-2}.

While no clear picture of the four-quark sector appears, some of the expected relations between top–boson operators are recovered (see Eq. (5)). The effective impact of $\Re[C_{tG}]$ in the linear combination $\mathcal{F}_1$ was gauged by separating it from the four-quark operators: it is much more constrained than the top–Z operators, but surprisingly its constraints are similar to those of the leading combination of four-quark operators. In other words, while the $t\bar{t}Z$ process is mostly gluon-initiated and therefore sensitive to modifications of the top–gluon vertex by the operator $\Re[C_{tG}]$, it is also highly affected by any non-SM structure in the quark-initated channel. The linear combinations in the subspace of four-quark operators should be compared with those found elsewhere for the $t\bar{t}$ process: the possibility of radiating the Z boson in $t\bar{t}Z$ production from an initial-state quark should provide novel directions of sensitivity.

The results of the linearised Fisher-rotated fit are presented in Figure 15 and Table 21. The limit on $\mathcal{F}_1$ expected by construction is indeed recovered.

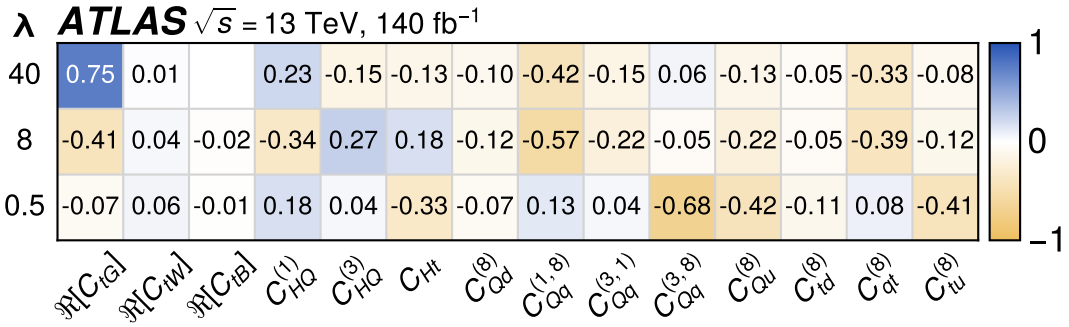

Figure 14: Eigenvector decomposition of the Fisher information matrix obtained from the linear global EFT fit. Each row represents a Fisher-rotated direction $\mathcal{F}$, for which the corresponding eigenvalue satisfies $\lambda > 0.1$, expressed in terms of the underlying Wilson coefficients in the Warsaw basis (columns).

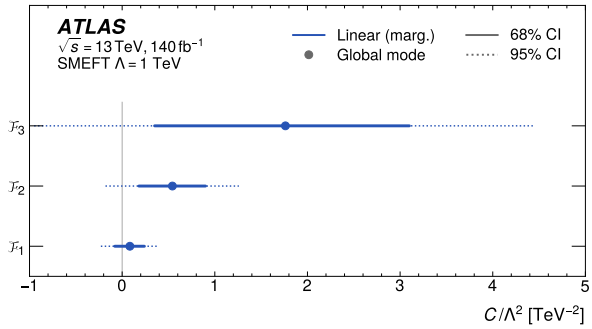

Figure 15: Comparison of the 68% and 95% credible intervals obtained for the Fisher-rotated linear fit. Also shown are the best-fit values (global mode) for each linear combination.

Table 21: Observed and expected 68% and 95% credible intervals for the main EFT directions of sensitivity, showing the results obtained from the Fisher-rotated linear fit. Also shown are the best-fit values (global mode) for each linear combination.

Wilson coefficient		68% CI (exp.)	95% CI (exp.)	68% CI (obs.)	95% CI (obs.)	Best-fit
$\mathcal{F}_1$	$O(\Lambda^{-2})$ (marg.)	$[-0.15, 0.16]$	$[-0.30, 0.31]$	$[-0.080, 0.24]$	$[-0.23, 0.39]$	0.08
$\mathcal{F}_2$	$O(\Lambda^{-2})$ (marg.)	$[-0.36, 0.36]$	$[-0.72, 0.70]$	$[0.18, 0.90]$	$[-0.18, 1.3]$	0.5
$\mathcal{F}_3$	$O(\Lambda^{-2})$ (marg.)	$[-1.4, 1.3]$	$[-2.7, 2.7]$	$[0.35, 3.1]$	$[-0.95, 4.5]$	2

12 Conclusion

This paper presents measurements of the inclusive and differential cross sections for production of a top-quark–top-antiquark pair in association with a Z boson ($t\bar{t}Z$) in 13 TeV proton–proton collisions. The full Run 2 dataset collected with the ATLAS experiment at the LHC between 2015 and 2018, amounting

to an integrated luminosity of 140 fb^{-1}, was used for this analysis. The targeted final states feature two, three or four leptons, focusing on the decay of the Z boson into a pair of electrons or muons but remaining inclusive in the decays of the $t\bar{t}$ system. This analysis supersedes, and largely improves upon, the previous Run 2 ATLAS result.

The inclusive $t\bar{t}Z$ cross section corresponding to the on-shell Z phase-space region for difermion masses of $70 < m_{f\bar{f}} < 110$ GeV is measured to be $\sigma_{t\bar{t}Z} = 0.86 \pm 0.06$ pb $= 0.86 \pm 0.04(\text{stat.}) \pm 0.04(\text{syst.})$ pb. The observed result is in agreement with the SM prediction $\sigma_{t\bar{t}Z}^{\text{NLO+NNLL}} = 0.86^{+0.08}_{-0.09}$ pb and other calculations at NLO QCD and electroweak accuracy. The result is limited by the systematic uncertainties associated with the modelling of background processes (Z+jets, non-prompt leptons), the renormalisation and factorisation scales of the signal process, and the determination of the integrated luminosity. The total uncertainty in the $t\bar{t}Z$ cross section is reduced by 38% (a factor of two for the systematic uncertainties alone) compared to the previous analysis. The improvements stem mainly from the multivariate techniques used throughout the analysis, and better modelling of both the signal and background processes, including data-driven approaches.

Detector-level observables sensitive to polarisation and spin correlations of the top quarks are statistically combined to search for such effects, for the first time in $t\bar{t}Z$ production. Templates from simulated $t\bar{t}Z$ events, generated with and without the SM spin density matrix, are used to extract a fraction $f_{\text{SM}} = 1.20 \pm 0.68$ reflecting the strength of spin correlations like those in the SM in $t\bar{t}Z$ data events, with the uncertainty largely dominated by its statistical component. This result is in agreement with the SM, and represents a 1.8σ departure from the null hypothesis of no spin correlations.

Furthermore, measurements of absolute and normalised differential production cross sections for the $t\bar{t}Z$ process are presented, in a large number of observables sensitive to MC modelling and potential BSM effects. Distributions at particle level and parton level, unfolded to specific fiducial volumes, are compared with simulations from various $t\bar{t}Z$ MC generators and with fixed-order theoretical predictions. Since the difference between the MC generators considered in this analysis is usually significantly smaller than the uncertainty of the measurement, it is not possible to decide which generator best describes the data.

Finally, the unfolded particle-level distributions are used to constrain potential BSM effects from dimension-6 operators in the framework of the SMEFT. Various fitting scenarios are considered, in order to give a complete picture of EFT effects in $t\bar{t}Z$ production. A large number of operators are considered, affecting both the top–Z coupling and $t\bar{t}$ production, and also including four-quark operators. The three most sensitive directions in the EFT space are identified through the Fisher information matrix of the measurements and lead to the tightest constraints. Compared to recent EFT searches by CMS covering large regions of phase-space and including multiple $t\bar{t} + X$ processes, the results presented in this paper leverage more information from the measurement of a single process. Overall, no significant deviation from the SM is observed, and exclusion limits are placed on several top–electroweak and four-quark SMEFT operators.

Acknowledgements

We thank CERN for the very successful operation of the LHC, as well as the support staff from our institutions without whom ATLAS could not be operated efficiently.

We acknowledge the support of ANPCyT, Argentina; YerPhI, Armenia; ARC, Australia; BMWFW and FWF, Austria; ANAS, Azerbaijan; CNPq and FAPESP, Brazil; NSERC, NRC and CFI, Canada; CERN;

ANID, Chile; CAS, MOST and NSFC, China; Minciencias, Colombia; MEYS CR, Czech Republic; DNRF and DNSRC, Denmark; IN2P3-CNRS and CEA-DRF/IRFU, France; SRNSFG, Georgia; BMBF, HGF and MPG, Germany; GSRI, Greece; RGC and Hong Kong SAR, China; ISF and Benoziyo Center, Israel; INFN, Italy; MEXT and JSPS, Japan; CNRST, Morocco; NWO, Netherlands; RCN, Norway; MEiN, Poland; FCT, Portugal; MNE/IFA, Romania; MESTD, Serbia; MSSR, Slovakia; ARRS and MIZŠ, Slovenia; DSI/NRF, South Africa; MICINN, Spain; SRC and Wallenberg Foundation, Sweden; SERI, SNSF and Cantons of Bern and Geneva, Switzerland; MOST, Taiwan; TENMAK, Türkiye; STFC, United Kingdom; DOE and NSF, United States of America. In addition, individual groups and members have received support from BCKDF, CANARIE, Compute Canada and CRC, Canada; PRIMUS 21/SCI/017 and UNCE SCI/013, Czech Republic; COST, ERC, ERDF, Horizon 2020, ICSC-NextGenerationEU and Marie Skłodowska-Curie Actions, European Union; Investissements d'Avenir Labex, Investissements d'Avenir Idex and ANR, France; DFG and AvH Foundation, Germany; Herakleitos, Thales and Aristeia programmes co-financed by EU-ESF and the Greek NSRF, Greece; BSF-NSF and MINERVA, Israel; Norwegian Financial Mechanism 2014-2021, Norway; NCN and NAWA, Poland; La Caixa Banking Foundation, CERCA Programme Generalitat de Catalunya and PROMETEO and GenT Programmes Generalitat Valenciana, Spain; Göran Gustafssons Stiftelse, Sweden; The Royal Society and Leverhulme Trust, United Kingdom.

The crucial computing support from all WLCG partners is acknowledged gratefully, in particular from CERN, the ATLAS Tier-1 facilities at TRIUMF (Canada), NDGF (Denmark, Norway, Sweden), CC-IN2P3 (France), KIT/GridKA (Germany), INFN-CNAF (Italy), NL-T1 (Netherlands), PIC (Spain), ASGC (Taiwan), RAL (UK) and BNL (USA), the Tier-2 facilities worldwide and large non-WLCG resource providers. Major contributors of computing resources are listed in Ref. [119].

Appendix

This Appendix provides additional information about the MVA approaches used to measure the inclusive $t\bar{t}Z$ cross section, as well as the full set of differential cross sections (absolute and normalised, unfolded to particle level and parton level) and further details of the unfolding procedure.

Tables 22, 23 and 24 list the kinematic quantities used as inputs to the training of the DNNs in the 2ℓ, 3ℓ and 4ℓ channels respectively. Table 25 collects the specific binning used for each differential cross-section measurement; the same binning is used whether unfolding to particle level or parton level.

Figures 16 to 23 present the differential cross sections for observables defined in the combination of the 3ℓ and 4ℓ fiducial volumes. Each figure contains four distributions: unfolded to particle level or parton level, absolute or normalised cross sections. Figures 24 to 28 similarly correspond to observables defined in the 3ℓ channel, and Figures 29 to 31 to those defined in the 4ℓ channel.

Finally, Tables 26 and 27 summarise tests of the compatibility of the unfolded data and predictions from various MC generators, for the absolute and normalised differential spectra respectively.

Table 22: Definition of the DNN input variables used in 2ℓOS signal regions. Jets and leptons are ordered by their p_{T} starting with the largest. To suppress the effect of mismodelling in events with high jet multiplicity, only the first eight jets ordered by p_{T} are considered when calculating DNN input variables if an event has more than eight jets, otherwise all jets in the event are considered.

Variable	**Definition**
H_{T}	Sum of p_{T} of all objects (jets and leptons) in the event.
$H_{\mathrm{T}}^{\mathrm{jets}}$	Sum of p_{T} of all jets in the event.
$p_{\mathrm{T}}^{X.\mathrm{jet}}$	p_{T} of the X'th jet, where only the first eight jets are considered.
$p_{\mathrm{T}}^{X.\mathrm{lep}}$	p_{T} of the X'th lepton.
W_{1t1W}	Weight for one-top hypothesis and $1W$ from multi-hypothesis hadronic t/W reconstruction. It is the probability that the event contains all three jets from one of the top quarks and two light jets from the decay of the other top quark. More details are provided in Section 5.5.
W_{1t}	Weight for one-top hypothesis from multi-hypothesis hadronic t/W reconstruction. The same as W_{1t1W}, with one top quark only.
$Centr_{\mathrm{jets}}$	scalar sum of p_{T} divided by sum of E for all jets.
$\Delta R(b_1, b_2)$	ΔR between two jets with highest b-tagging working point. The jets with the same working point are ordered by p_{T}.
H_1^{jets}	First Fox–Wolfram moment built from jets only. The first Fox–Wolfram moment is defined as $H_1 = \sum_{i,j} \frac{\vec{p}_i \cdot \vec{p}_j}{E_{\mathrm{vis}}^2}$, where $\vec{p}_i$ and $\vec{p}_j$ are 3-momenta of i'th and j'th objects (jet or lepton) and E_{vis} is all visible energy in the event.
$N_{jj}^{m<50\mathrm{GeV}}$	Number of jet–jet combinations with mass lower than 50 GeV.
m_Z, y^Z, p_{T}^Z	Mass, rapidity and transverse momentum of the Z boson.
$\min\left(M_{jj}^{\mathrm{ave}}\right)$	Average (over the number of jets in event) minimum invariant mass of jet pairs. For each jet, the other jet which results in the minimum dijet invariant mass is found. The observable is the average of these masses over all jets in the event.
$\Delta R(\ell, \ell)$	ΔR between two leptons.
PCBT_{Xj}	Discretised b-tagging efficiency (100–85–77–70–60%) of the X-th jet.
$N_{\mathrm{lep}}^{\mathrm{top}}$	Number of leptonic top candidates.
$N_{\mathrm{had}}^{\mathrm{top}}$	Number of hadronic top candidates.
N_{had}^{W}	Number of hadronic W candidates.
$E_{\mathrm{T}}^{\mathrm{miss}}$	Missing transverse momentum in the event.
H_1	First Fox–Wolfram momentent built from jets and leptons.
$p_{\mathrm{T}}^{t\bar{t},\mathrm{spanet}}$	Transverse momentum of the $t\bar{t}$ system reconstructed from jets predicted by SPANet.

Table 23: Definition of the DNN input variables used in 3ℓ signal regions. Jets and leptons are ordered by their p_{T} starting with the largest.

Variable	**Definition**
PCBT_{b1}	Highest discretised b-tagging efficiency (100–85–77–70–60%) of all jets in the event.
PCBT_{b2}	Second-highest discretised b-tagging efficiency of all jets in the event.
Jet $p_{\mathrm{T},i}$	Transverse momentum of the i'th jet in the event where $i \in [1, 4]$.
$E_{\mathrm{T}}^{\mathrm{miss}}$	Missing transverse momentum in the event.
Lepton $p_{\mathrm{T},i}$	Transverse momentum of the i'th lepton in the event where $i \in [1, 3]$.
m_t^{lep}	Reconstructed mass of the leptonically decaying top quark.
m_t^{had}	Reconstructed mass of the hadronically decaying top quark.
N_{jets}	Jet multiplicity in the event.
Leading b-tagged jet p_{T}	Transverse momentum of the jet with the highest discretised b-tagging efficiency. If two have the same bin the leading-p_{T} jet of the two is used.
$H_{\mathrm{T}}^{\mathrm{jets}}$	Sum of the transverse momentum of all jets in the event.
$\Delta R(\ell_i, b_1)$	Distance in ΔR between the i'th lepton and the b-tagged jet tagged with the highest working point in the event where $i \in [1, 3]$.
$p_{\mathrm{T},i}^{Z}$	Transverse momentum of the first and second lepton ($i \in [1, 2]$) assigned to the Z boson based on their invariant mass being closest to the Z mass.
η_i^Z	Pseudorapidity of the first and second lepton ($i \in [1, 2]$) assigned to the Z boson based on their invariant mass being closest to the Z mass.
Lepton $p_{\mathrm{T}}^{\text{non-}Z}$	Transverse momentum of the remaining lepton not assigned to the Z boson.

Table 24: Definition of the DNN input variables used in 4ℓ signal regions for the same-flavour (SF) and different-flavour (DF) trainings. Jets and leptons are ordered by their p_{T} starting with the largest.

Variable	**Definition**	**SF**	**DF**
$E_{\mathrm{T}}^{\mathrm{miss}}$	Missing transverse momentum in the event.	✓	—
$m^{\ell\ell,\text{non-}Z}$	Invariant mass of two leptons which were not reconstructed as originating from the Z boson.	✓	✓
2νSM weight	Output of the *Two neutrino scanning method* for the event.	✓	✓
p_{T}^{Z}	Transverse momentum of the OSSF lepton pair identified as Z decay (invariant mass of lepton pair closest to Z mass).	✓	✓
$m_t^{\ell b}$	Invariant mass of lepton and b-tagged jet reconstructed as originating from the top quark by the *Two neutrino scanning method*.	✓	✓
$m_{\bar{t}}^{\ell b}$	Invariant mass of lepton and b-tagged jet reconstructed as originating from anti-top quark by *Two neutrino scanning method*.	✓	✓
PCBT_{b1}	Highest discretised b-tagging efficiency (100–85–77–70–60%) of all jets in the event.	✓	—
$p_{\mathrm{T}}^{\mathrm{lep}_1}$	Transverse momentum of the leading lepton.	✓	✓
$p_{\mathrm{T}}^{\mathrm{jet}_2}$	Transverse momentum of the sub-leading jet.	✓	✓
PCBT_{b2}	Second-highest discretised b-tagging efficiency of all jets in the event.		
N_{jets}	Jet multiplicity in the event.	—	✓
$N_{b\text{-tagged jets}}$	b-tagged (85% efficiency) jet multiplicity in the event.	—	✓

Table 25: Bin ranges for the differential observables defined in Table 15. The bin ranges are identical for particle- and parton-level measurements.

Observable	Channels	Bins	Bin Ranges
p_{T}^{Z} [GeV]	$3\ell + 4\ell$	8	[0, 60, 100, 140, 180, 230, 280, 350, 1000]
$\lvert y^{Z}\rvert$	$3\ell + 4\ell$	9	[0, 0.125, 0.275, 0.425, 0.6, 0.775, 0.95, 1.175, 1.45, 2.5]
$p_{\mathrm{T}}^{\ell,\text{non-}Z}$ [GeV]	3ℓ	5	[0, 35, 55, 80, 120, 500]
$\lvert\Delta y(Z, t_{\mathrm{lep}})\rvert$	3ℓ	5	[0, 0.25, 0.6, 1.05, 1.55, 5]
$\lvert\Delta\Phi(Z, t_{\mathrm{lep}})\rvert/\pi$	3ℓ	6	[0, 0.16, 0.44, 0.66, 0.82, 0.93, 1]
$\lvert\Delta\Phi(\ell_t^+, \ell_{\bar{t}}^-)\rvert/\pi$	4ℓ	7	[0, 0.2, 0.37, 0.53, 0.67, 0.79, 0.89, 1]
H_{T}^{ℓ} [GeV]	3ℓ	8	[50, 130, 165, 195, 230, 275, 330, 405, 800]
H_{T}^{ℓ} [GeV]	4ℓ	5	[50, 195, 250, 315, 400, 800]
N_{jets}	3ℓ	4	[2.5, 3.5, 4.5, 5.5, 10.5]
N_{jets}	4ℓ	3	[1.5, 2.5, 3.5, 8.5]
p_{T}^{t} [GeV]	$3\ell + 4\ell$	10	[0, 48, 80, 112, 144, 176, 216, 256, 296, 352, 800]
$p_{\mathrm{T}}^{t\bar{t}}$ [GeV]	$3\ell + 4\ell$	10	[0, 50, 80, 110, 140, 170, 210, 250, 290, 330, 1000]
$\lvert\Delta\Phi(t\bar{t}, Z)\rvert/\pi$	$3\ell + 4\ell$	5	[0, 0.73, 0.86, 0.94, 0.98, 1]
$m^{t\bar{t}}$ [GeV]	$3\ell + 4\ell$	10	[0, 370, 420, 470, 530, 600, 680, 780, 890, 1010, 2000]
$m^{t\bar{t}Z}$ [GeV]	$3\ell + 4\ell$	10	[400, 580, 650, 720, 800, 890, 990, 1100, 1220, 1350, 2000]
$\lvert y^{t\bar{t}Z}\rvert$	$3\ell + 4\ell$	10	[0, 0.075, 0.2, 0.35, 0.5, 0.65, 0.8, 0.95, 1.1, 1.25, 2.5]
$\cos\theta_Z^*$	$3\ell + 4\ell$	8	[−1, −0.75, −0.5, −0.25, 0, 0.25, 0.5, 0.75, 1]

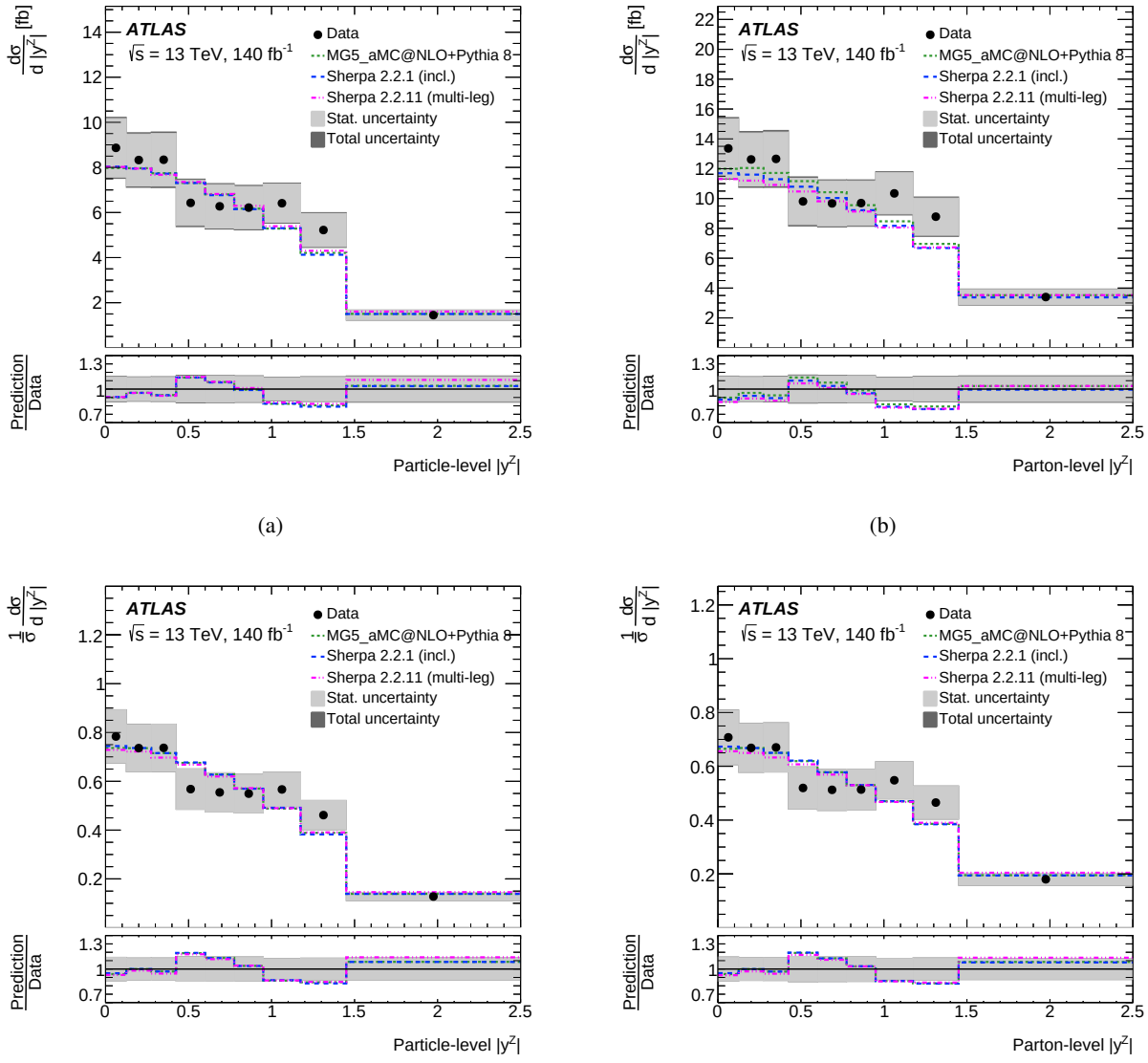

Figure 16: Cross-section measurement of the $|y^Z|$ observable in the combination of the 3ℓ and 4ℓ channels, absolute and normalised, unfolded to particle level (a,c) and parton level (b,d).

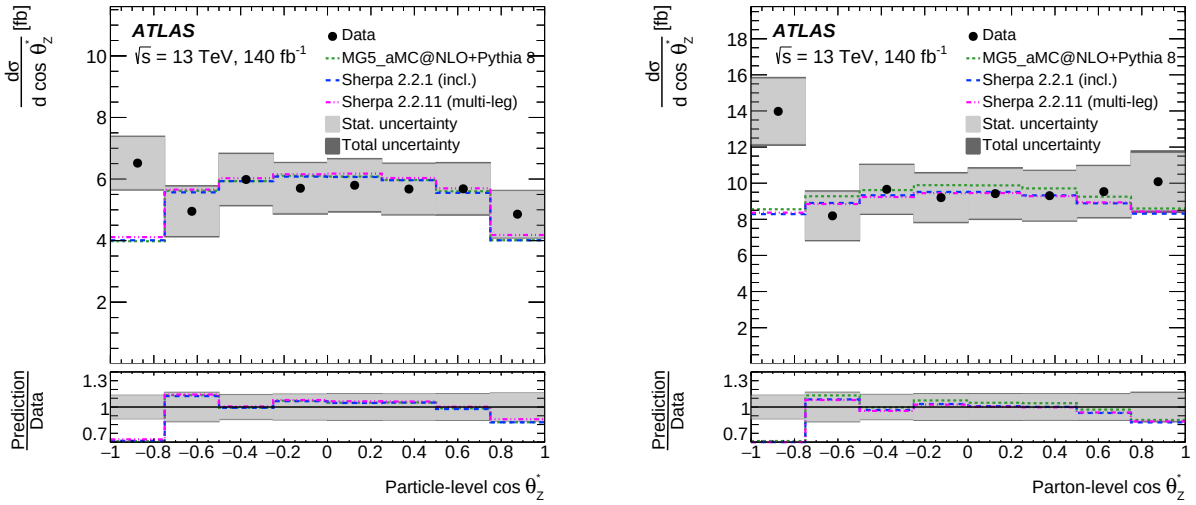

(a) (b)

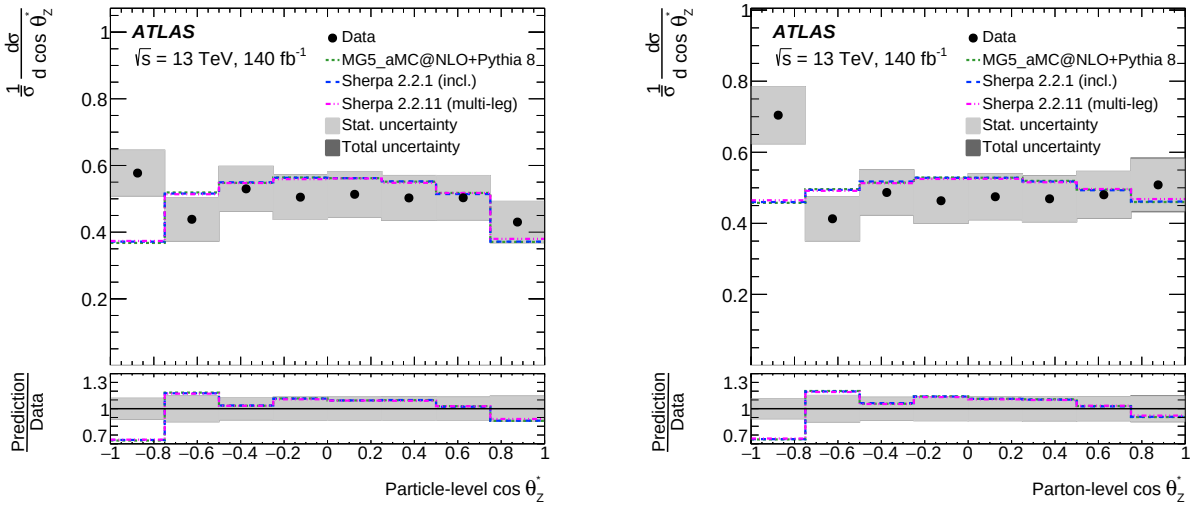

(c) (d)

Figure 17: Cross-section measurement of the $\cos\theta^*_Z$ observable in the combination of the 3ℓ and 4ℓ channels, absolute and normalised, unfolded to particle level (a,c) and parton level (b,d).

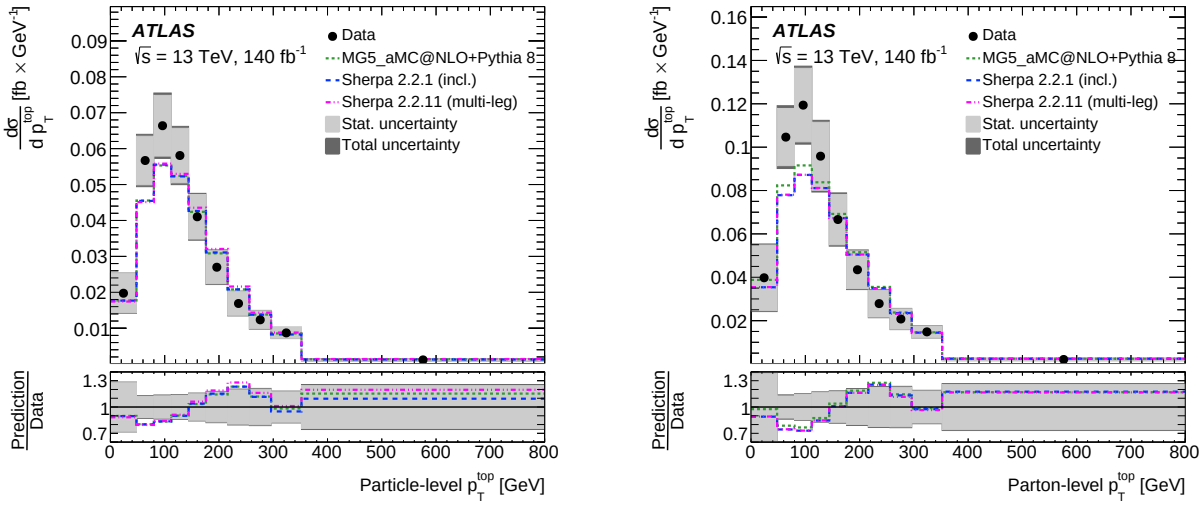

(a) (b)

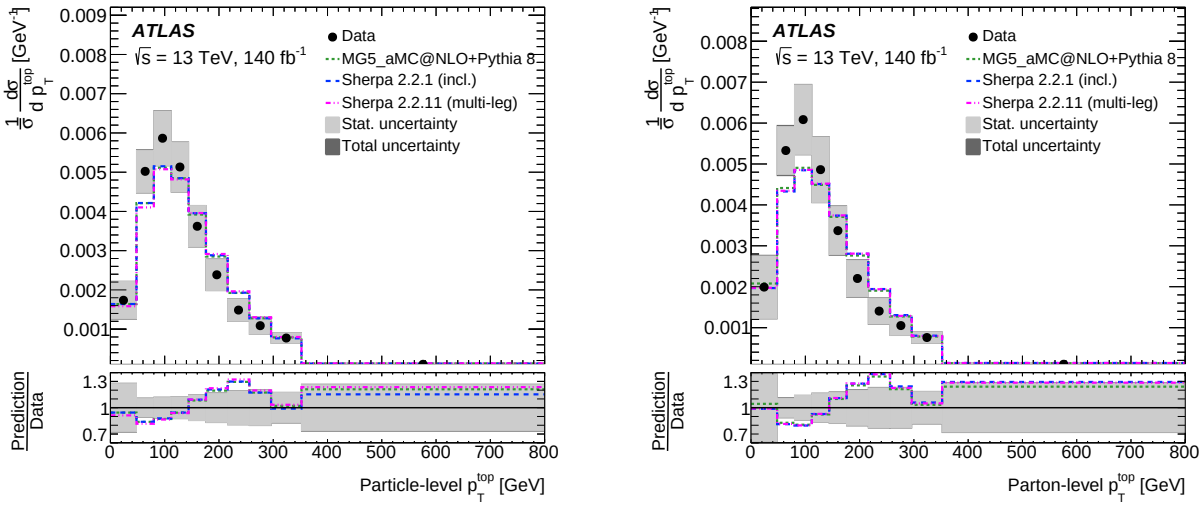

(c) (d)

Figure 18: Cross-section measurement of the p_{T}^{t} observable in the combination of the 3ℓ and 4ℓ channels, absolute and normalised, unfolded to particle level (a,c) and parton level (b,d).

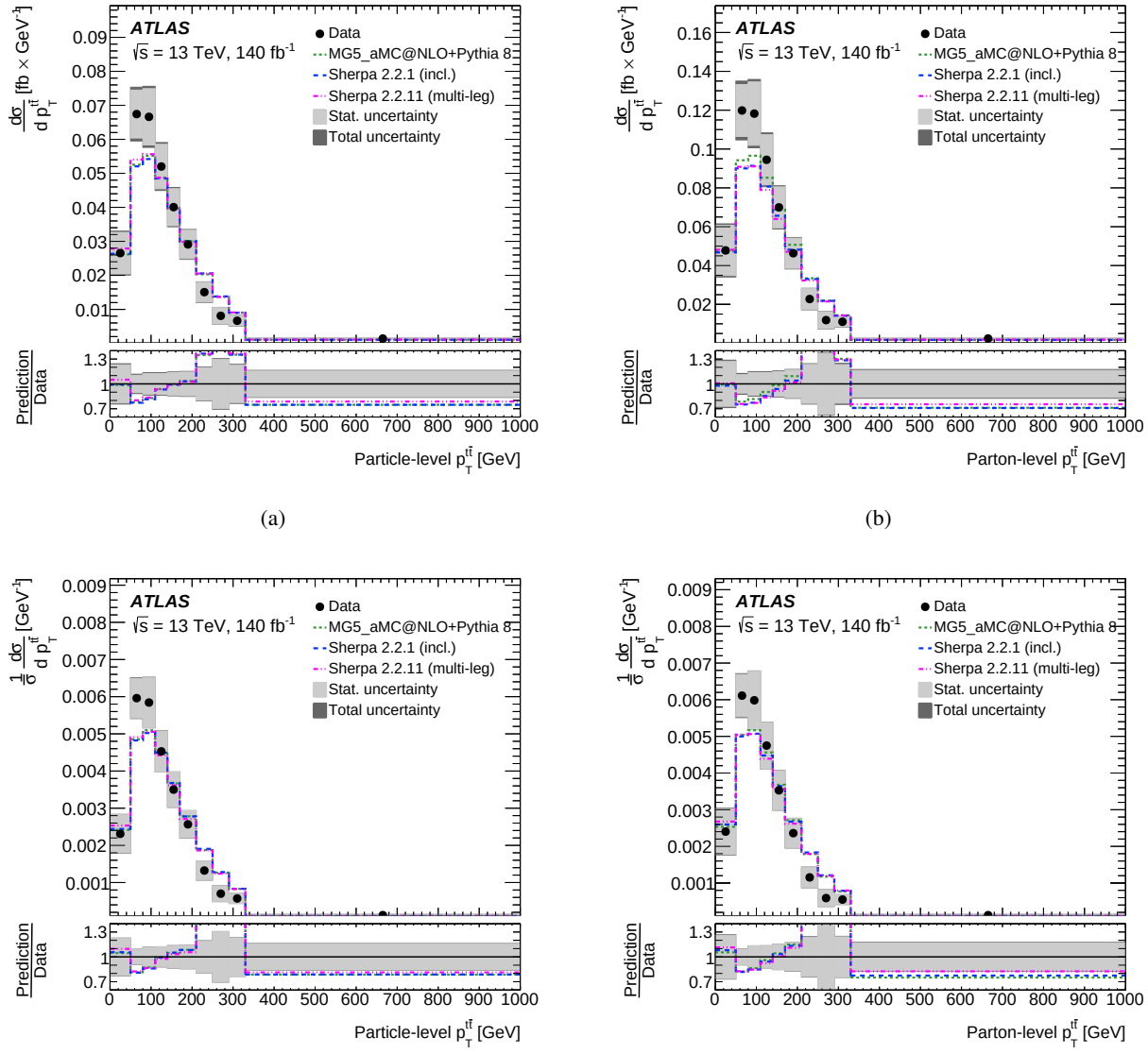

Figure 19: Cross-section measurement of the $p_{\mathrm{T}}^{t\bar{t}}$ observable in the combination of the 3ℓ and 4ℓ channels, absolute and normalised, unfolded to particle level (a,c) and parton level (b,d).

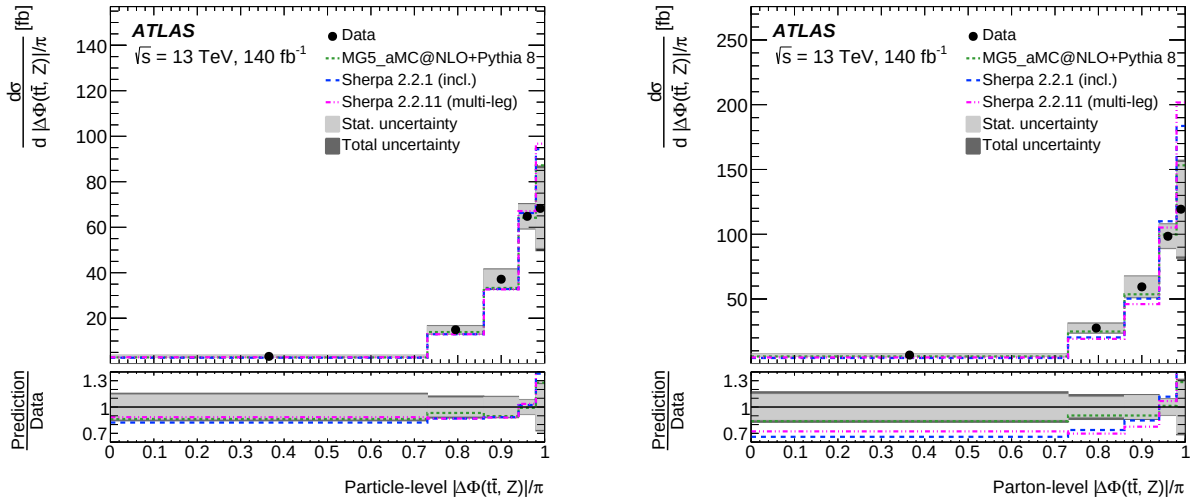

(a) (b)

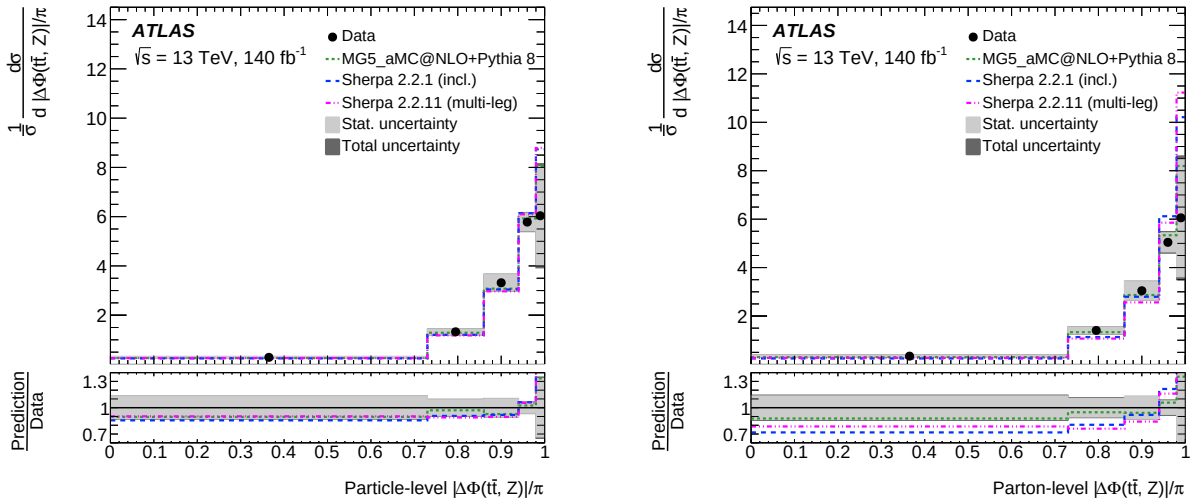

(c) (d)

Figure 20: Cross-section measurement of the $|\Delta\Phi(t\bar{t}, Z)|/\pi$ observable in the combination of the 3ℓ and 4ℓ channels, absolute and normalised, unfolded to particle level (a,c) and parton level (b,d).

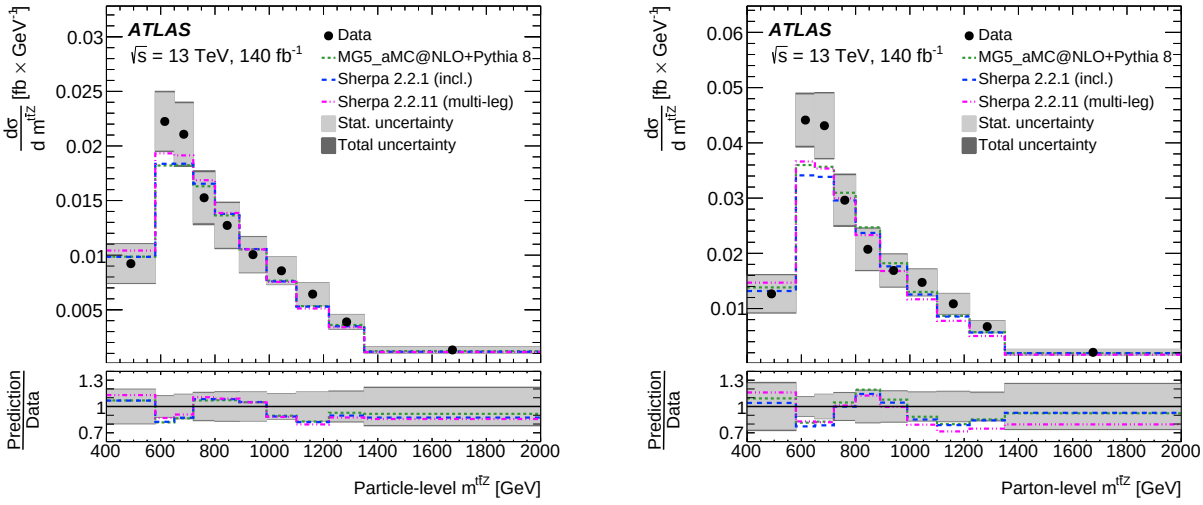

(a) (b)

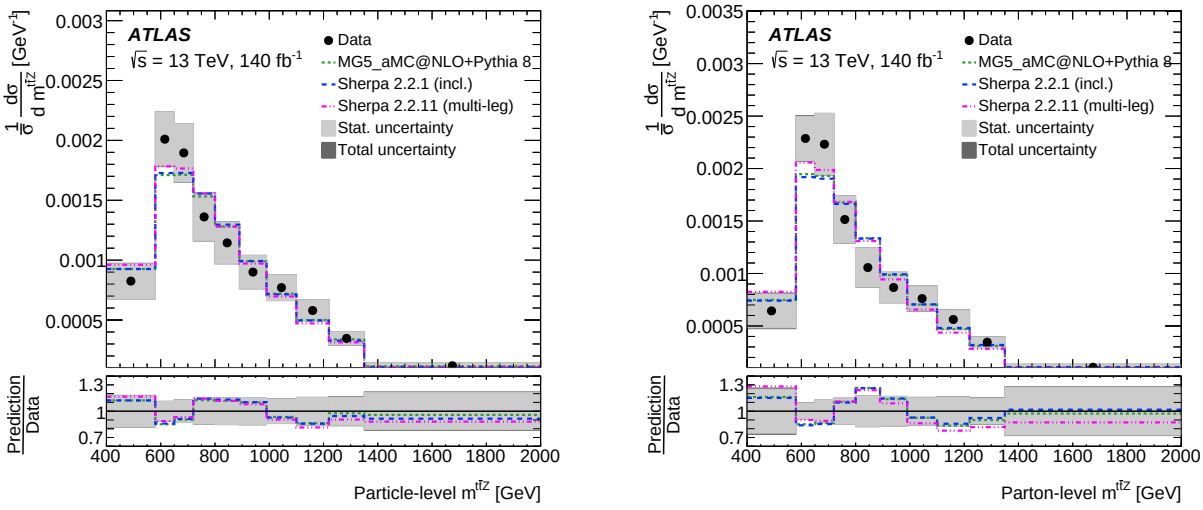

(c) (d)

Figure 21: Cross-section measurement of the $m^{t\bar{t}Z}$ observable in the combination of the 3ℓ and 4ℓ channels, absolute and normalised, unfolded to particle level (a,c) and parton level (b,d).

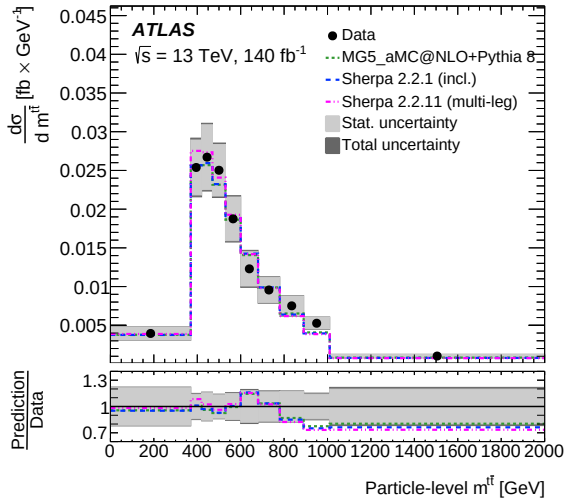

(a)

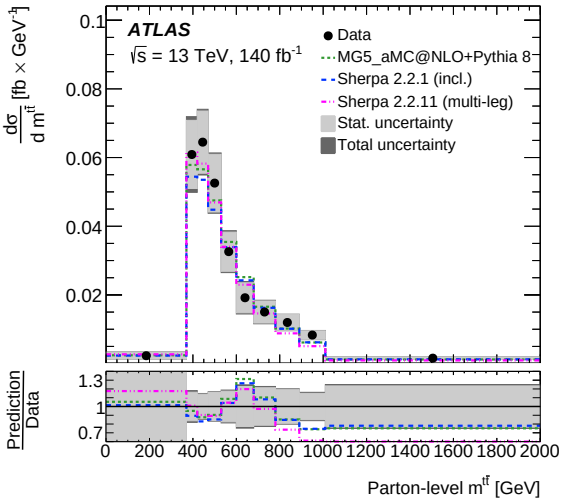

(b)

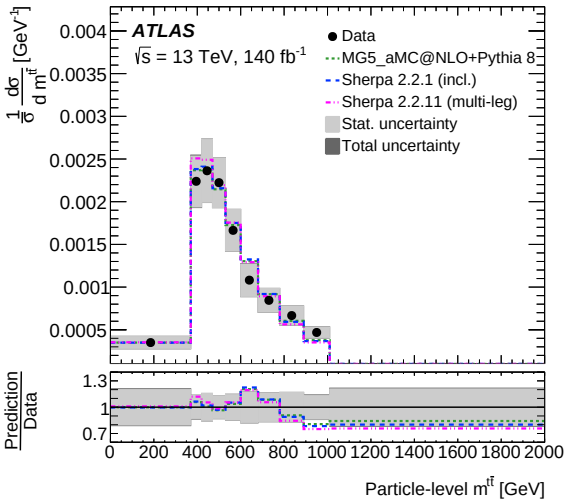

(c)

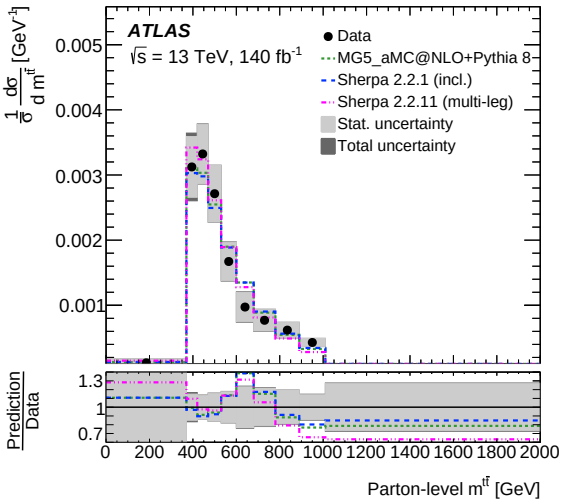

(d)

Figure 22: Cross-section measurement of the $m^{t\bar{t}}$ observable in the combination of the 3ℓ and 4ℓ channels, absolute and normalised, unfolded to particle level (a,c) and parton level (b,d).

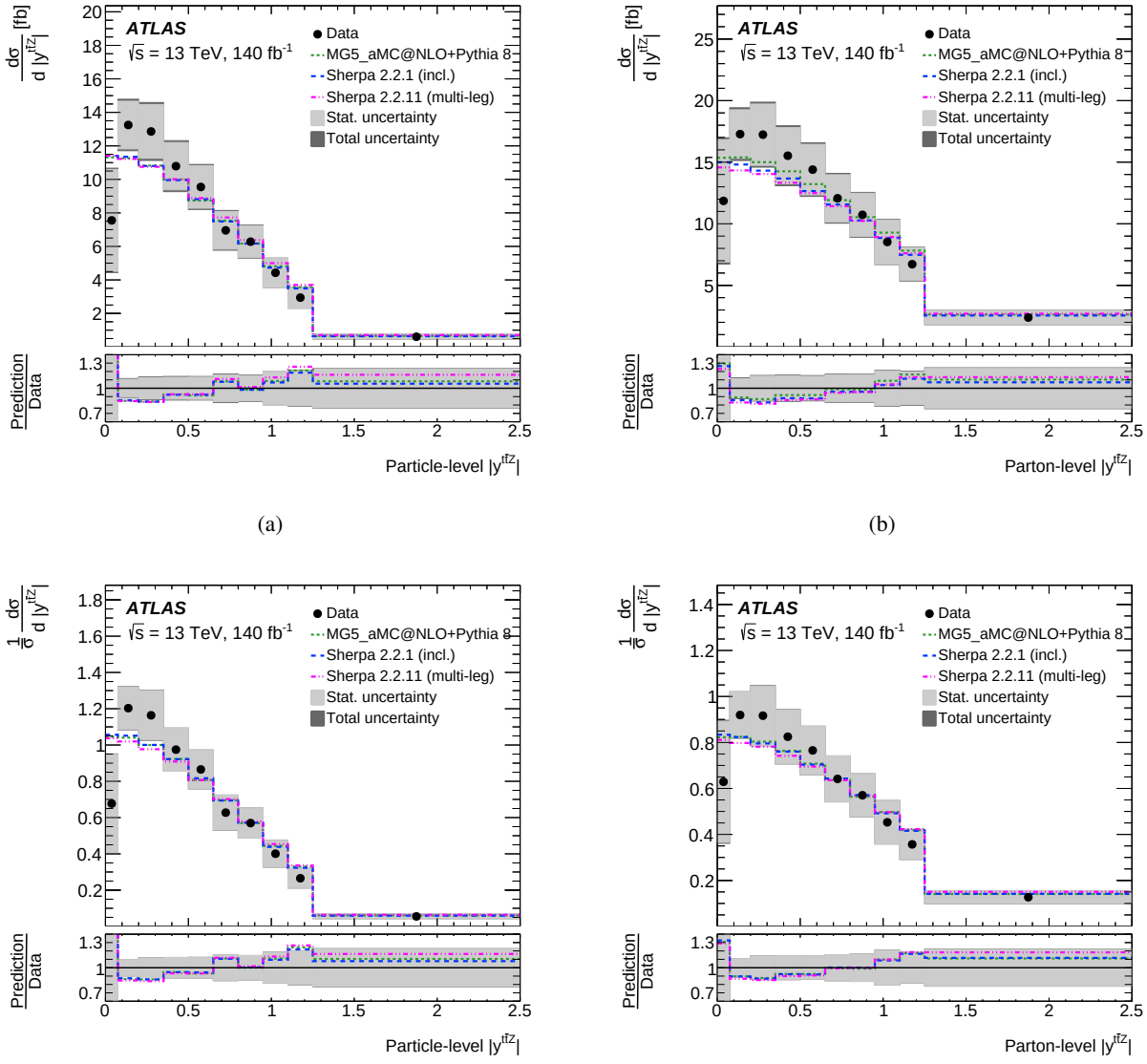

Figure 23: Cross-section measurement of the $|y^{t\bar{t}Z}|$ observable in the combination of the 3ℓ and 4ℓ channels, absolute and normalised, unfolded to particle level (a,c) and parton level (b,d).

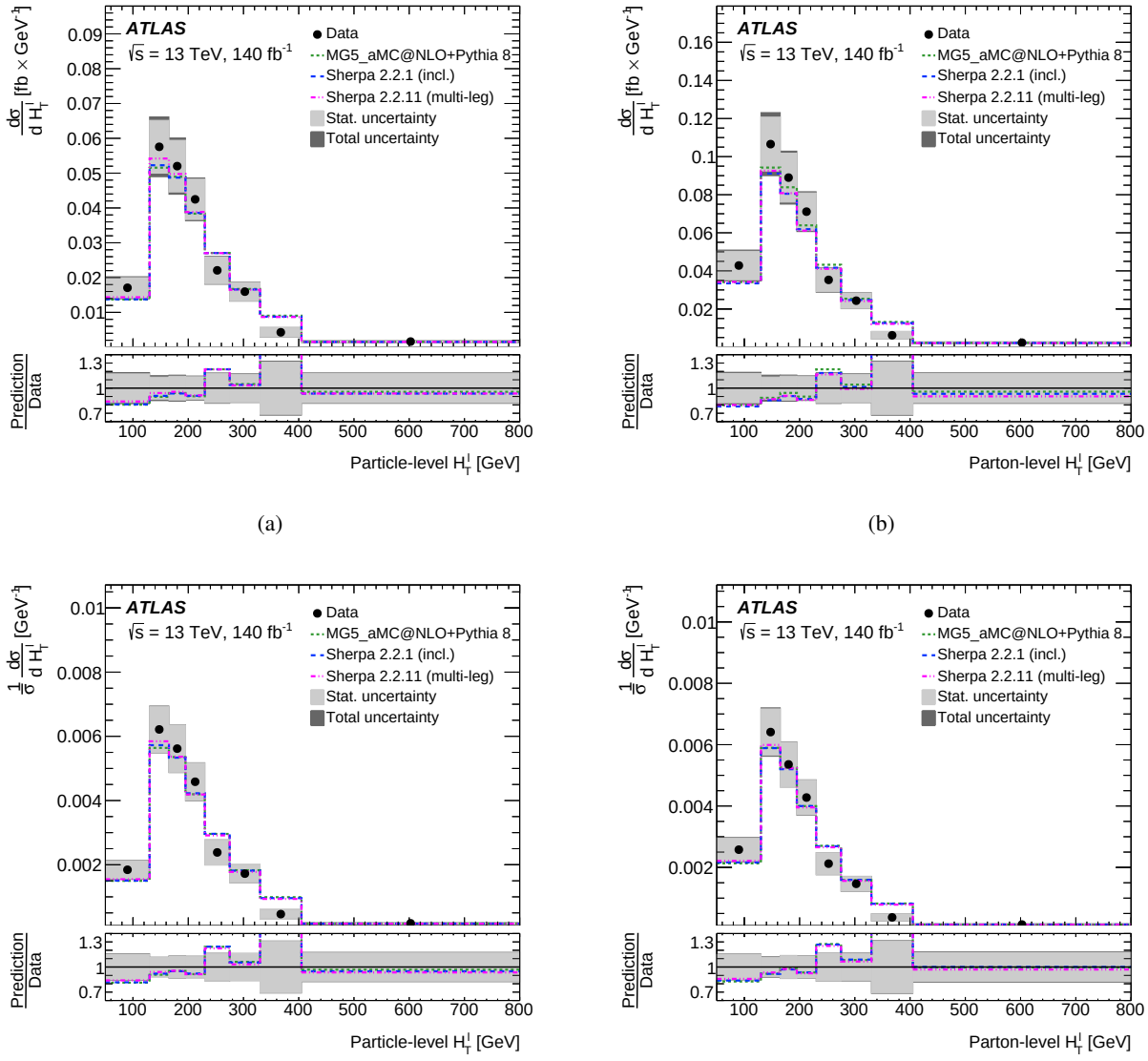

Figure 24: Cross-section measurement of the H_{T}^{ℓ} observable in the 3ℓ channel, absolute and normalised, unfolded to particle level (a,c) and parton level (b,d).

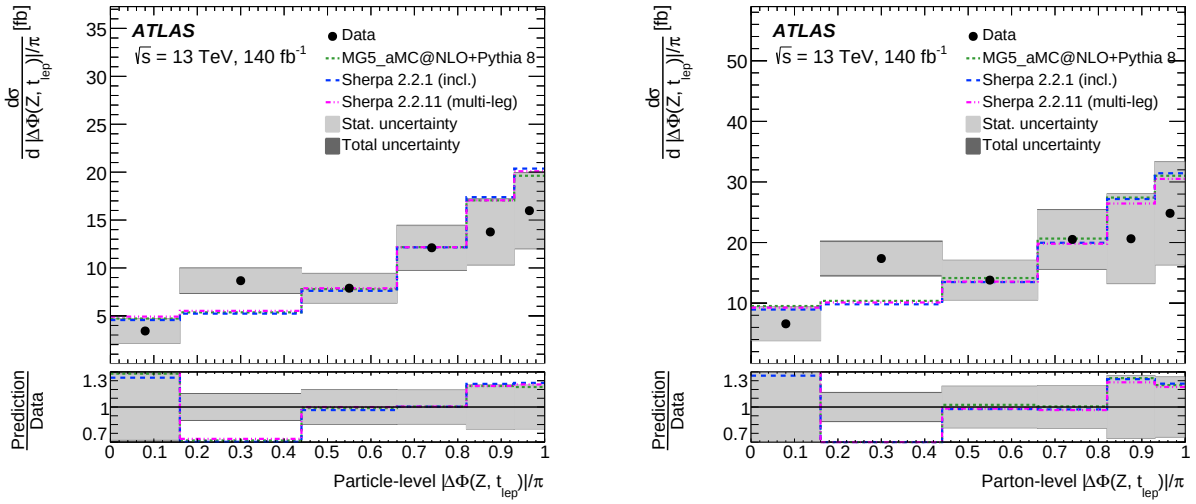

(a) (b)

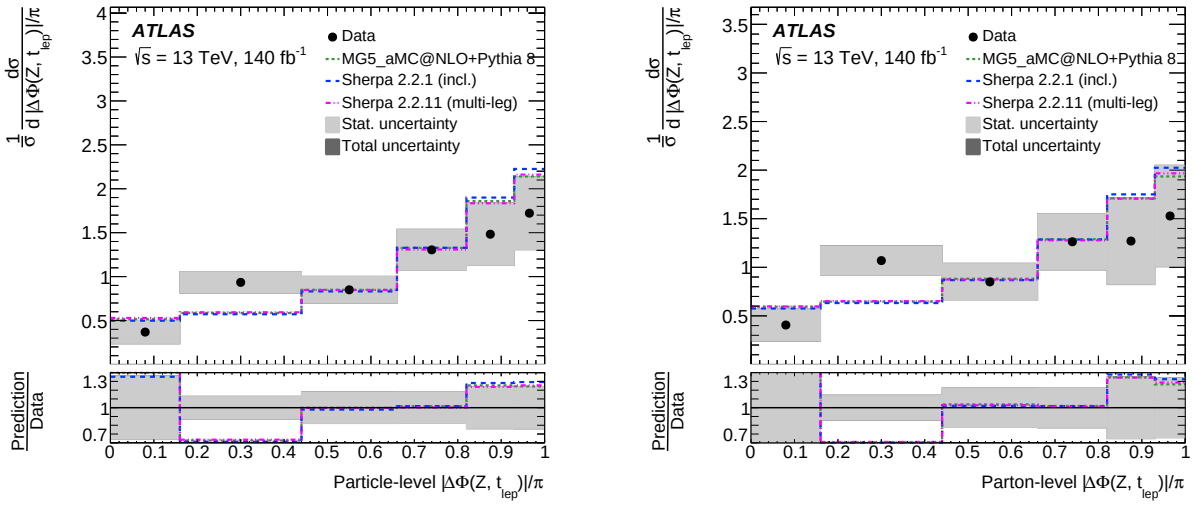

(c) (d)

Figure 25: Cross-section measurement of the $|\Delta\Phi(Z, t_{\text{lep}})|/\pi$ observable in the 3ℓ channel, absolute and normalised, unfolded to particle level (a,c) and parton level (b,d).

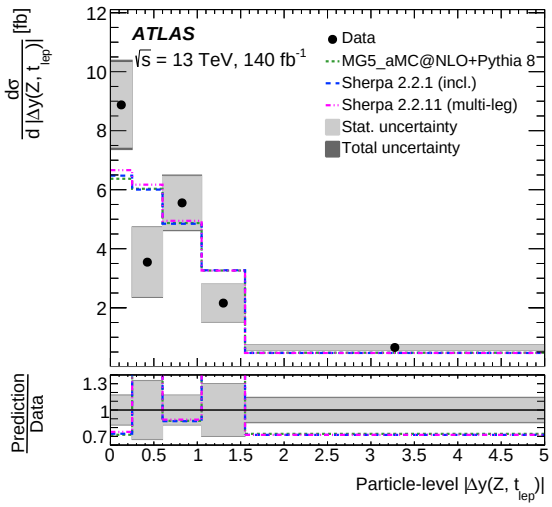

(a)

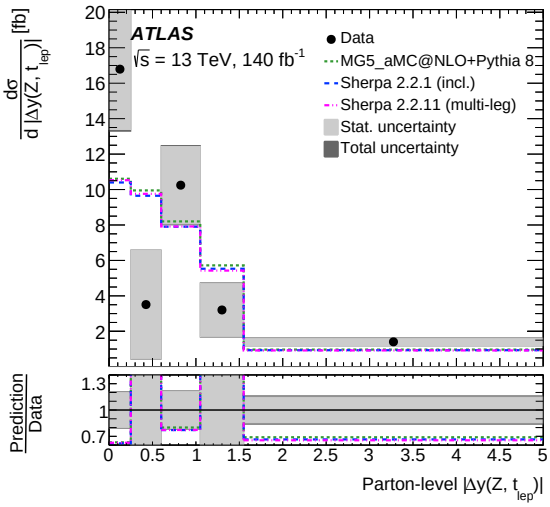

(b)

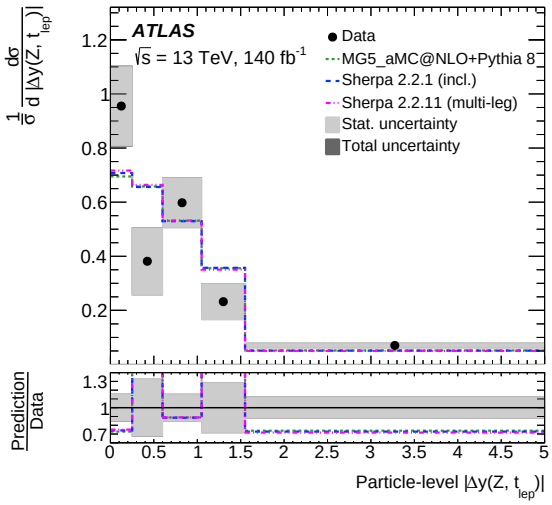

(c)

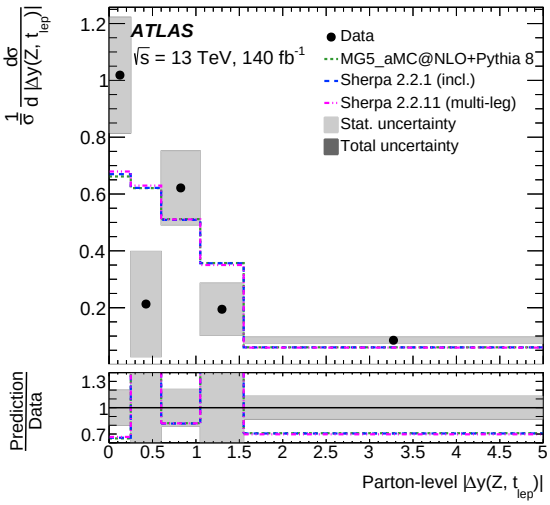

(d)

Figure 26: Cross-section measurement of the $|\Delta y(Z, t_{\text{lep}})|$ observable in the 3ℓ channel, absolute and normalised, unfolded to particle level (a,c) and parton level (b,d).

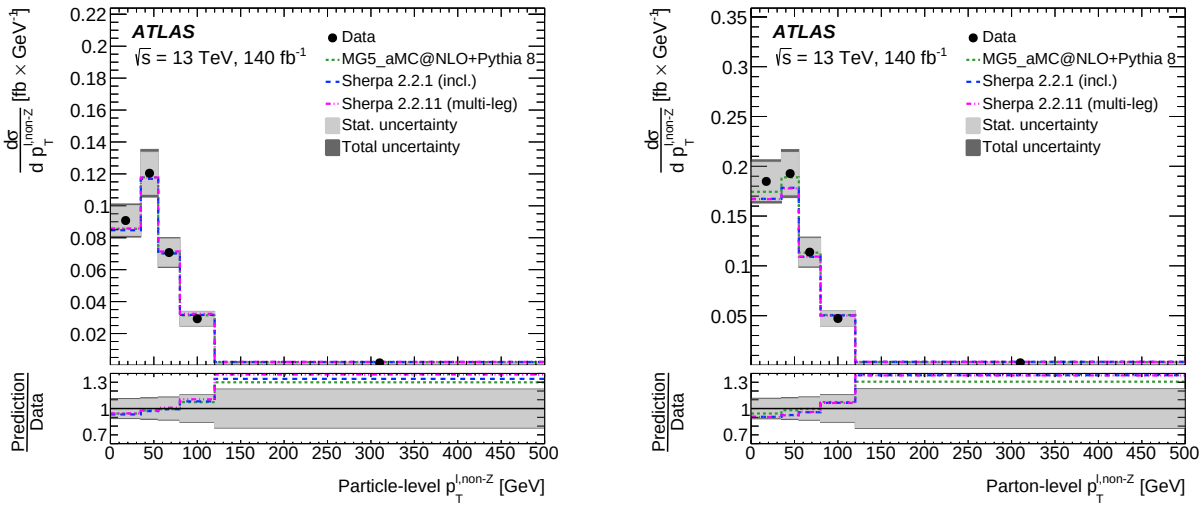

(a) (b)

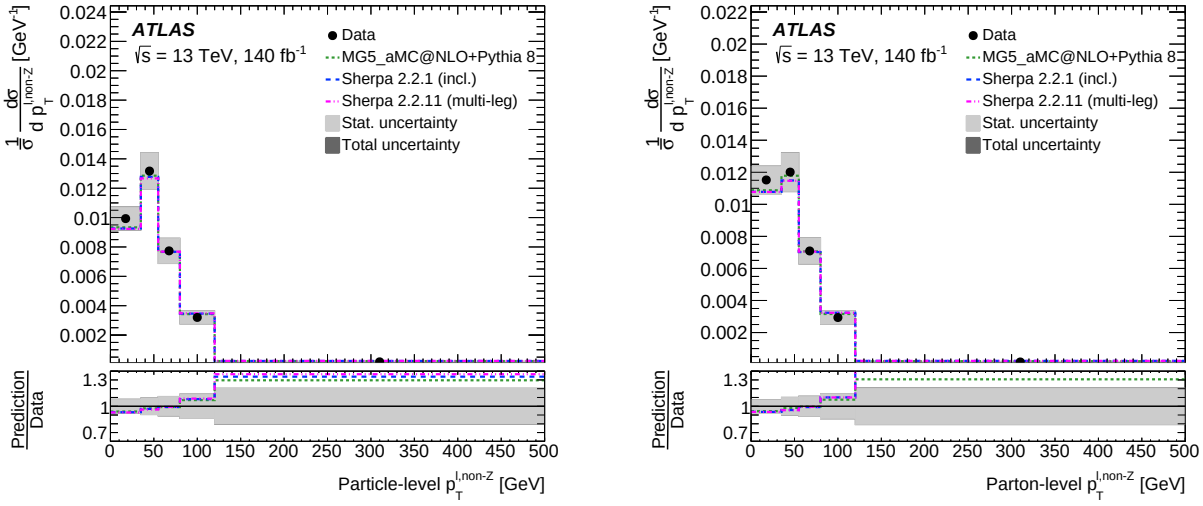

(c) (d)

Figure 27: Cross-section measurement of the $p_{\mathrm{T}}^{\ell,\text{non-}Z}$ observable in the 3ℓ channel, absolute and normalised, unfolded to particle level (a,c) and parton level (b,d).

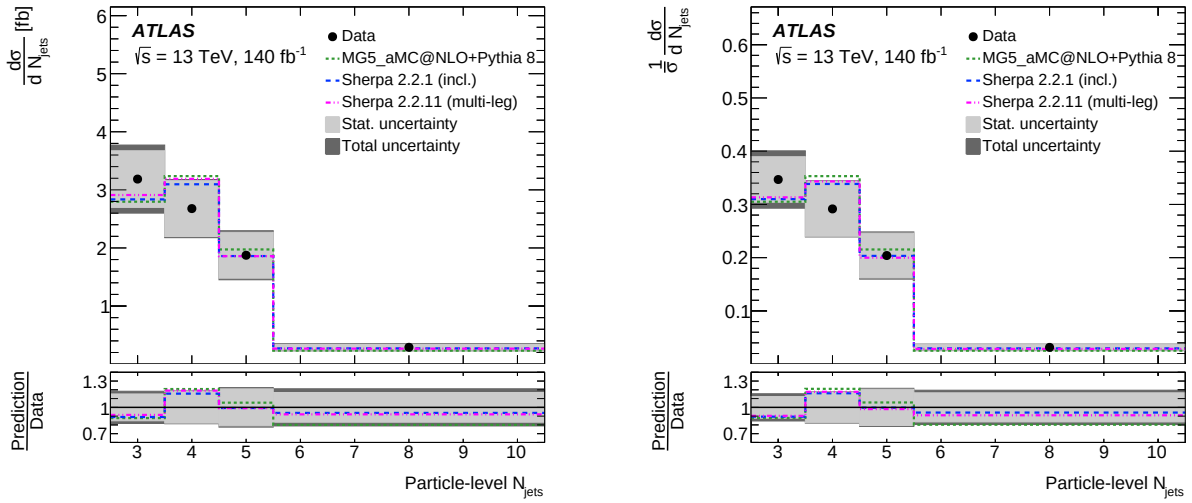

(a) (b)

Figure 28: Cross-section measurement of the N_{jets} observable in the 3ℓ channel, unfolded to particle level, absolute (a) and normalised (b).

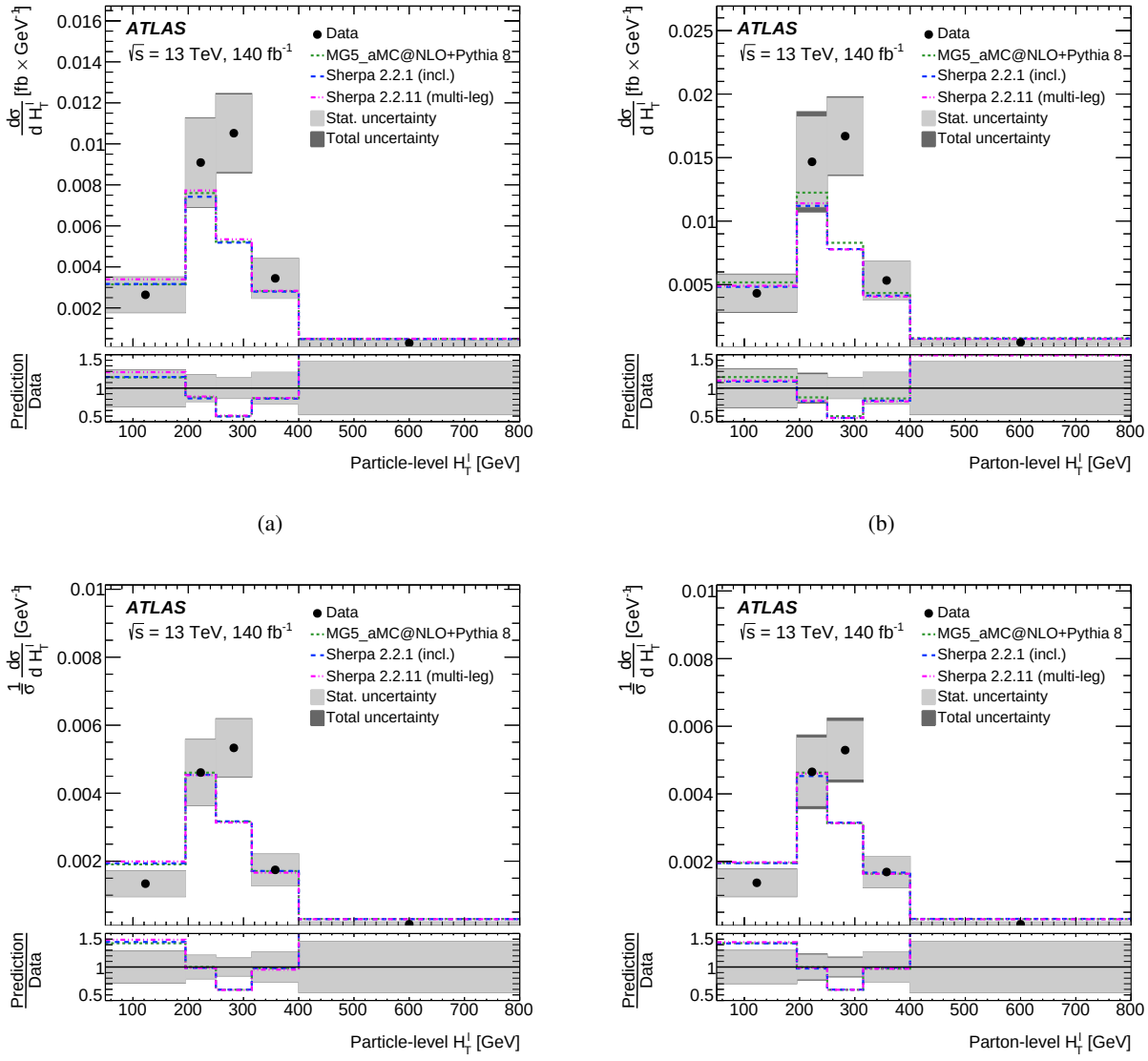

Figure 29: Cross-section measurement of the H_{T}^{ℓ} observable in the 4ℓ channel, absolute and normalised, unfolded to particle level (a,c) and parton level (b,d).

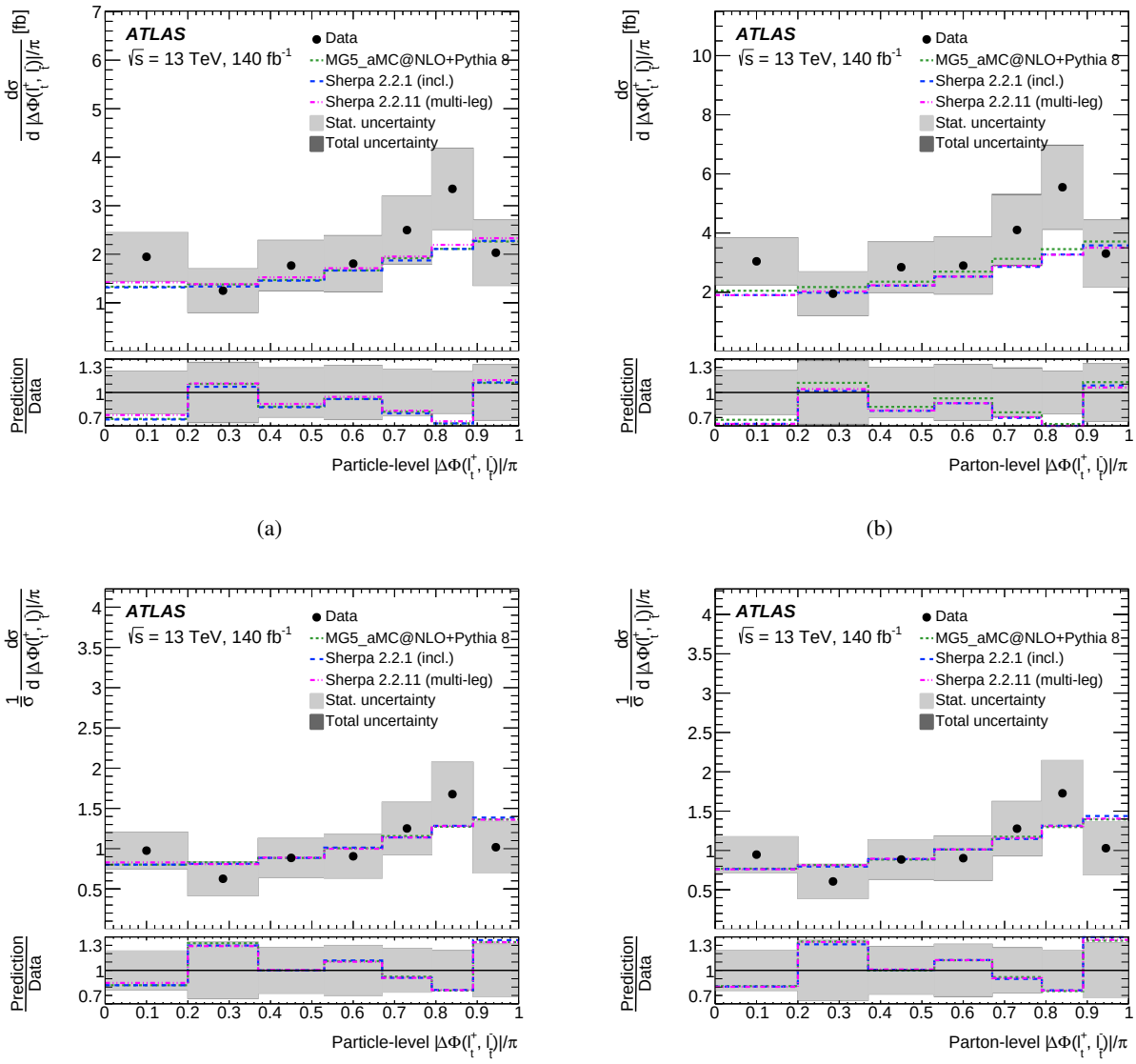

Figure 30: Cross-section measurement of the $|\Delta\Phi(\ell_t^+, \ell_{\bar{t}}^-)|$ observable in the 4ℓ channel, absolute and normalised, unfolded to particle level (a,c) and parton level (b,d).

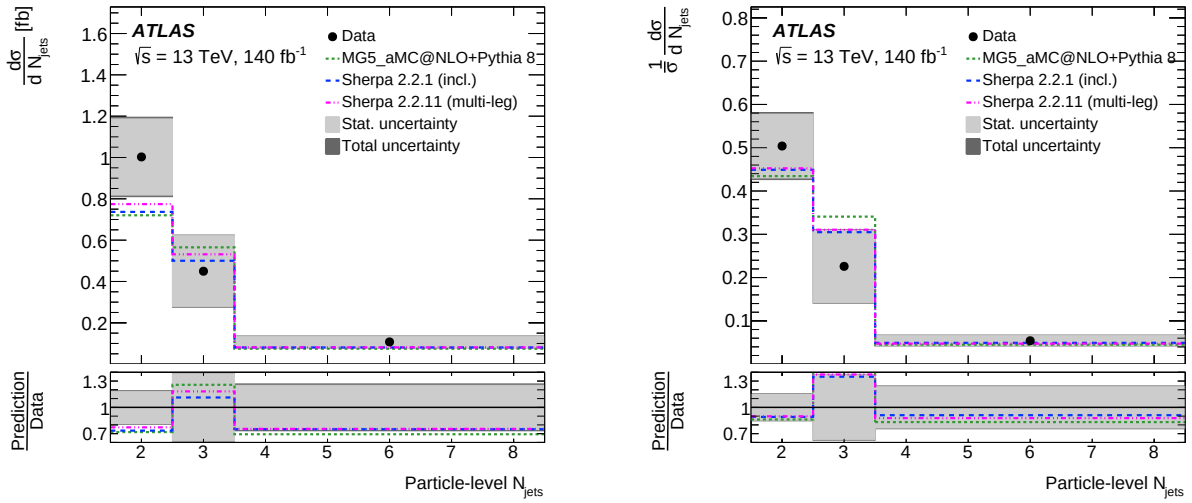

(a) (b)

Figure 31: Cross-section measurement of the N_{jets} observable in the 4ℓ channel, unfolded to particle level, absolute (a) and normalised (b).

Table 26: Summary of the compatibility tests, i.e. p-values, between the unfolded absolute differential spectra and the various predictions, in the 3ℓ and 4ℓ channels as well as in their combination, at particle-level and parton-level.

		aMC@NLO+Pythia 8		Sherpa 2.2.1 (incl.)		Sherpa 2.2.11 (multi-leg)	
	Variable	parton	particle	parton	particle	parton	particle
3ℓ	$\lvert\Delta\Phi(Z, t_{\text{lep}})\rvert/\pi$	0.12	0.09	0.09	0.05	0.14	0.09
	$\lvert\Delta y(Z, t_{\text{lep}})\rvert$	0.08	0.05	0.09	0.05	0.08	0.04
	H_{T}^{ℓ}	0.04	0.04	0.06	0.07	0.11	0.1
	$p_{\text{T}}^{\ell,\text{non-}Z}$	0.75	0.75	0.44	0.63	0.44	0.51
	N_{jets}	-	0.55	-	0.9	-	0.82
4ℓ	N_{jets}	-	0.36	-	0.43	-	0.55
	$\lvert\Delta\Phi(\ell_t^+, \ell_{\bar{t}}^-)\rvert/\pi$	0.68	0.67	0.52	0.65	0.52	0.77
	H_{T}^{ℓ}	0.04	0.04	0.02	0.04	0.03	0.04
$3\ell + 4\ell$	$\lvert y^Z\rvert$	0.77	0.78	0.70	0.77	0.64	0.77
	p_{T}^Z	0.09	0.08	0.13	0.13	0.22	0.23
	$\cos\theta_Z^*$	0.20	0.17	0.21	0.19	0.24	0.22
	$\lvert\Delta\Phi(t\bar{t}, Z)\rvert/\pi$	0.84	0.82	0.08	0.53	0.07	0.56
	$m^{t\bar{t}}$	0.89	0.97	0.8	0.92	0.49	0.83
	$m^{t\bar{t}Z}$	0.86	0.93	0.64	0.91	0.58	0.91
	p_{T}^t	0.45	0.56	0.2	0.59	0.22	0.39
	$p_{\text{T}}^{t\bar{t}}$	0.09	0.07	0.05	0.05	0.07	0.1
	$\lvert y^{t\bar{t}Z}\rvert$	0.95	0.8	0.86	0.85	0.66	0.65

Table 27: Summary of the compatibility tests, i.e. p-values, between the unfolded normalised differential spectra and the various predictions, in the 3ℓ and 4ℓ channels as well as in their combination, at particle-level and parton-level.

		aMC@NLO+Pythia 8		Sherpa 2.2.1 (incl.)		Sherpa 2.2.11 (multi-leg)	
	Variable	parton	particle	parton	particle	parton	particle
3ℓ	$\lvert\Delta\Phi(Z, t_{\text{lep}})\rvert/\pi$	0.07	0.05	0.04	0.02	0.07	0.06
	$\lvert\Delta y(Z, t_{\text{lep}})\rvert$	0.03	0.03	0.03	0.02	0.03	0.02
	H_{T}^{ℓ}	0.02	0.02	0.02	0.04	0.05	0.07
	$p_{\text{T}}^{\ell,\text{non-}Z}$	0.63	0.63	0.29	0.5	0.29	0.41
	N_{jets}	-	0.42	-	0.81	-	0.75
4ℓ	N_{jets}	-	0.40	-	0.65	-	0.61
	$\lvert\Delta\Phi(\ell_t^+, \ell_{\bar{t}}^-)\rvert/\pi$	0.75	0.76	0.73	0.75	0.74	0.80
	H_{T}^{ℓ}	0.03	0.02	0.03	0.02	0.03	0.02
$3\ell + 4\ell$	$\lvert y^Z\rvert$	0.71	0.72	0.71	0.71	0.70	0.69
	p_{T}^Z	0.04	0.03	0.06	0.06	0.13	0.14
	$\cos\theta_Z^*$	0.11	0.11	0.12	0.12	0.15	0.15
	$\lvert\Delta\Phi(t\bar{t}, Z)\rvert/\pi$	0.74	0.71	0.02	0.36	0.02	0.39
	$m^{t\bar{t}}$	0.79	0.88	0.87	0.73	0.27	0.43
	$m^{t\bar{t}Z}$	0.84	0.93	0.8	0.91	0.81	0.89
	p_{T}^t	0.03	0.23	0.01	0.29	0.01	0.1
	$p_{\text{T}}^{t\bar{t}}$	0.02	0.01	0.01	0.01	0.02	0.03
	$\lvert y^{t\bar{t}Z}\rvert$	0.87	0.52	0.85	0.64	0.59	0.28

References

[1] ATLAS Collaboration, *Measurement of the top quark mass in the $t\bar{t} \to$ lepton+jets channel from $\sqrt{s} = 8$ TeV ATLAS data and combination with previous results*, Eur. Phys. J. C **79** (2019) 290, arXiv: 1810.01772 [hep-ex].

[2] R. S. Chivukula, S. B. Selipsky and E. H. Simmons, *Nonoblique effects in the $Zb\bar{b}$ vertex from extended technicolor dynamics*, Phys. Rev. Lett. **69** (1992) 575, arXiv: hep-ph/9204214.

[3] R. S. Chivukula, E. H. Simmons and J. Terning, *A heavy top quark and the Zbb vertex in non-commuting extended technicolor*, Phys. Lett. B **331** (1994) 383, arXiv: hep-ph/9404209.

[4] K. Hagiwara and N. Kitazawa, *Extended technicolor contribution to the Zbb vertex*, Phys. Rev. D **52** (1995) 5374, arXiv: hep-ph/9504332.

[5] U. Mahanta, *Noncommuting ETC corrections to $Zt\bar{t}$ vertex*, Phys. Rev. D **55** (1997) 5848, arXiv: hep-ph/9611289.

[6] U. Mahanta,
Probing noncommuting extended technicolor effects by $e^+e^- \to t\bar{t}$ at the Next Linear Collider,
Phys. Rev. D **56** (1997) 402.

[7] M. Perelstein, *Little Higgs models and their phenomenology*,
Prog. Part. Nucl. Phys. **58** (2007) 247, arXiv: hep-ph/0512128.

[8] ATLAS Collaboration,
Observation of four-top-quark production in the multilepton final state with the ATLAS detector,
Eur. Phys. J. C **83** (2023) 496, arXiv: 2303.15061 [hep-ex].

[9] CMS Collaboration,
Observation of four top quark production in proton–proton collisions at $\sqrt{s} = 13$ TeV,
Phys. Lett. B **847** (2023) 138290, arXiv: 2305.13439 [hep-ex].

[10] ATLAS Collaboration, *Search for direct top squark pair production in events with a Higgs or Z boson, and missing transverse momentum in $\sqrt{s} = 13$ TeV pp collisions with the ATLAS detector*,
JHEP **08** (2017) 006, arXiv: 1706.03986 [hep-ex].

[11] ATLAS Collaboration, *Search for new phenomena in events with same-charge leptons and b-jets in pp collisions at $\sqrt{s} = 13$ TeV with the ATLAS detector*, JHEP **12** (2018) 039,
arXiv: 1807.11883 [hep-ex].

[12] ATLAS Collaboration, *Search for squarks and gluinos in final states with same-sign leptons and jets using 139 fb^{-1} of data collected with the ATLAS detector*, JHEP **06** (2020) 046,
arXiv: 1909.08457 [hep-ex].

[13] CMS Collaboration, *Search for physics beyond the standard model in events with two leptons of same sign, missing transverse momentum, and jets in proton–proton collisions at $\sqrt{s} = 13$ TeV*,
Eur. Phys. J. C **77** (2017) 578, arXiv: 1704.07323 [hep-ex].

[14] ATLAS Collaboration, *Evidence for the associated production of the Higgs boson and a top quark pair with the ATLAS detector*, Phys. Rev. D **97** (2018) 072003, arXiv: 1712.08891 [hep-ex].

[15] ATLAS Collaboration, *Observation of Higgs boson production in association with a top quark pair at the LHC with the ATLAS detector*, Phys. Lett. B **784** (2018) 173,
arXiv: 1806.00425 [hep-ex].

[16] CMS Collaboration, *Measurement of the Higgs boson production rate in association with top quarks in final states with electrons, muons, and hadronically decaying tau leptons at $\sqrt{s} = 13$ TeV*,
Eur. Phys. J. C **81** (2021) 378, arXiv: 2011.03652 [hep-ex].

[17] ATLAS Collaboration, *Observation of the associated production of a top quark and a Z boson in pp collisions at $\sqrt{s} = 13$ TeV with the ATLAS detector*, JHEP **07** (2020) 124,
arXiv: 2002.07546 [hep-ex].

[18] CMS Collaboration, *Inclusive and differential cross section measurements of single top quark production in association with a Z boson in proton–proton collisions at $\sqrt{s} = 13$ TeV*,
JHEP **02** (2022) 107, arXiv: 2111.02860 [hep-ex].

[19] D. de Florian et al.,
Handbook of LHC Higgs Cross Sections: 4. Deciphering the Nature of the Higgs Sector, (2016),
arXiv: 1610.07922 [hep-ph].

[20] S. Frixione, V. Hirschi, D. Pagani, H.-S. Shao and M. Zaro,
Electroweak and QCD corrections to top-pair hadroproduction in association with heavy bosons,
JHEP **06** (2015) 184, arXiv: 1504.03446 [hep-ph].

[21] A. Kulesza, L. Motyka, D. Schwartländer, T. Stebel and V. Theeuwes, *Associated production of a top quark pair with a heavy electroweak gauge boson at NLO+NNLL accuracy*, Eur. Phys. J. C **79** (2019) 249, arXiv: 1812.08622 [hep-ph].

[22] A. Broggio et al., *Top-quark pair hadroproduction in association with a heavy boson at NLO+NNLL including EW corrections*, JHEP **08** (2019) 039, arXiv: 1907.04343 [hep-ph].

[23] CMS Collaboration, *Measurement of top quark pair production in association with a Z boson in proton-proton collisions at $\sqrt{s}$ = 13 TeV*, JHEP **03** (2020) 056, arXiv: 1907.11270 [hep-ex].

[24] ATLAS Collaboration, *Measurements of the inclusive and differential production cross sections of a top-quark-antiquark pair in association with a Z boson at $\sqrt{s}$ = 13 TeV with the ATLAS detector*, Eur. Phys. J. C **81** (2021) 737, arXiv: 2103.12603 [hep-ex].

[25] I. Brivio and M. Trott, *The Standard Model as an Effective Field Theory*, Phys. Rept. **793** (2019) 1, arXiv: 1706.08945 [hep-ph].

[26] I. Brivio, *SMEFTsim 3.0 — a practical guide*, JHEP **04** (2021) 073, arXiv: 2012.11343 [hep-ph].

[27] B. Ravina, E. Simpson and J. Howarth, *Observing $t\bar{t}Z$ spin correlations at the LHC*, Eur. Phys. J. C **81** (2021) 809, arXiv: 2106.09690 [hep-ph].

[28] ATLAS Collaboration, *The ATLAS Experiment at the CERN Large Hadron Collider*, JINST **3** (2008) S08003.

[29] ATLAS Collaboration, *ATLAS Insertable B-Layer: Technical Design Report*, ATLAS-TDR-19; CERN-LHCC-2010-013, 2010, URL: https://cds.cern.ch/record/1291633, Addendum: ATLAS-TDR-19-ADD-1; CERN-LHCC-2012-009, 2012, URL: https://cds.cern.ch/record/1451888.

[30] B. Abbott et al., *Production and integration of the ATLAS Insertable B-Layer*, JINST **13** (2018) T05008, arXiv: 1803.00844 [physics.ins-det].

[31] ATLAS Collaboration, *Performance of the ATLAS trigger system in 2015*, Eur. Phys. J. C **77** (2017) 317, arXiv: 1611.09661 [hep-ex].

[32] ATLAS Collaboration, *The ATLAS Collaboration Software and Firmware*, ATL-SOFT-PUB-2021-001, 2021, URL: https://cds.cern.ch/record/2767187.

[33] ATLAS Collaboration, *Luminosity determination in pp collisions at $\sqrt{s}$ = 13 TeV using the ATLAS detector at the LHC*, Eur. Phys. J. C **83** (2023) 982, arXiv: 2212.09379 [hep-ex].

[34] G. Avoni et al., *The new LUCID-2 detector for luminosity measurement and monitoring in ATLAS*, JINST **13** (2018) P07017.

[35] ATLAS Collaboration, *Performance of electron and photon triggers in ATLAS during LHC Run 2*, Eur. Phys. J. C **80** (2020) 47, arXiv: 1909.00761 [hep-ex].

[36] ATLAS Collaboration, *Performance of the ATLAS muon triggers in Run 2*, JINST **15** (2020) P09015, arXiv: 2004.13447 [physics.ins-det].

[37] ATLAS Collaboration, *2015 start-up trigger menu and initial performance assessment of the ATLAS trigger using Run-2 data*, ATL-DAQ-PUB-2016-001, 2016, URL: https://cds.cern.ch/record/2136007.

[38] ATLAS Collaboration, *Trigger Menu in 2016*, ATL-DAQ-PUB-2017-001, 2017, URL: https://cds.cern.ch/record/2242069.

[39] ATLAS Collaboration, *Trigger Menu in 2017*, ATL-DAQ-PUB-2018-002, 2018, URL: https://cds.cern.ch/record/2625986.

[40] T. Sjöstrand, S. Mrenna and P. Skands, *A brief introduction to PYTHIA 8.1*, Comput. Phys. Commun. **178** (2008) 852, arXiv: 0710.3820 [hep-ph].

[41] NNPDF Collaboration, *Parton distributions with LHC data*, Nucl. Phys. B **867** (2013) 244, arXiv: 1207.1303 [hep-ph].

[42] ATLAS Collaboration, *The Pythia 8 A3 tune description of ATLAS minimum bias and inelastic measurements incorporating the Donnachie–Landshoff diffractive model*, ATL-PHYS-PUB-2016-017, 2016, URL: https://cds.cern.ch/record/2206965.

[43] ATLAS Collaboration, *The ATLAS Simulation Infrastructure*, Eur. Phys. J. C **70** (2010) 823, arXiv: 1005.4568 [physics.ins-det].

[44] S. Agostinelli et al., *GEANT4 — a simulation toolkit*, Nucl. Instr. Meth. **A 506** (2003) 250.

[45] ATLAS Collaboration, *The simulation principle and performance of the ATLAS fast calorimeter simulation FastCaloSim*, ATL-PHYS-PUB-2010-013, 2010, URL: https://cds.cern.ch/record/1300517.

[46] ATLAS Collaboration, *The new Fast Calorimeter Simulation in ATLAS*, ATL-SOFT-PUB-2018-002, 2018, URL: https://cds.cern.ch/record/2630434.

[47] J. Alwall et al., *The automated computation of tree-level and next-to-leading order differential cross sections, and their matching to parton shower simulations*, JHEP **07** (2014) 079, arXiv: 1405.0301 [hep-ph].

[48] NNPDF Collaboration, *Parton distributions for the LHC run II*, JHEP **04** (2015) 040, arXiv: 1410.8849 [hep-ph].

[49] S. Frixione, E. Laenen, P. Motylinski and B. R. Webber, *Angular correlations of lepton pairs from vector boson and top quark decays in Monte Carlo simulations*, JHEP **04** (2007) 081, arXiv: hep-ph/0702198.

[50] P. Artoisenet, R. Frederix, O. Mattelaer and R. Rietkerk, *Automatic spin-entangled decays of heavy resonances in Monte Carlo simulations*, JHEP **03** (2013) 015, arXiv: 1212.3460 [hep-ph].

[51] T. Sjöstrand et al., *An introduction to PYTHIA 8.2*, Comput. Phys. Commun. **191** (2015) 159, arXiv: 1410.3012 [hep-ph].

[52] ATLAS Collaboration, *ATLAS Pythia 8 tunes to 7 TeV data*, ATL-PHYS-PUB-2014-021, 2014, URL: https://cds.cern.ch/record/1966419.

[53] D. J. Lange, *The EvtGen particle decay simulation package*, Nucl. Instrum. Meth. A **462** (2001) 152.

[54] M. Bähr et al., *Herwig++ physics and manual*, Eur. Phys. J. C **58** (2008) 639, arXiv: 0803.0883 [hep-ph].

[55] J. Bellm et al., *Herwig 7.0/Herwig++ 3.0 release note*, Eur. Phys. J. C **76** (2016) 196, arXiv: 1512.01178 [hep-ph].

[56] ATLAS Collaboration, *Modelling of the $t\bar{t}H$ and $t\bar{t}V(V = W, Z)$ processes for $\sqrt{s} = 13$ TeV ATLAS analyses*, ATL-PHYS-PUB-2016-005, 2016, URL: https://cds.cern.ch/record/2120826.

[57] E. Bothmann et al., *Event generation with Sherpa 2.2*, SciPost Phys. **7** (2019) 034, arXiv: 1905.09127 [hep-ph].

[58] S. Catani, F. Krauss, B. R. Webber and R. Kuhn, *QCD Matrix Elements + Parton Showers*, JHEP **11** (2001) 063, arXiv: hep-ph/0109231.

[59] S. Höche, F. Krauss, S. Schumann and F. Siegert, *QCD matrix elements and truncated showers*, JHEP **05** (2009) 053, arXiv: 0903.1219 [hep-ph].

[60] S. Höche, F. Krauss, M. Schönherr and F. Siegert, *QCD matrix elements + parton showers. The NLO case*, JHEP **04** (2013) 027, arXiv: 1207.5030 [hep-ph].

[61] F. Demartin, B. Maier, F. Maltoni, K. Mawatari and M. Zaro, *tWH associated production at the LHC*, Eur. Phys. J. C **77** (2017) 34, arXiv: 1607.05862 [hep-ph].

[62] S. Alioli, P. Nason, C. Oleari and E. Re, *A general framework for implementing NLO calculations in shower Monte Carlo programs: the POWHEG BOX*, JHEP **06** (2010) 043, arXiv: 1002.2581 [hep-ph].

[63] T. Gleisberg and S. Höche, *Comix, a new matrix element generator*, JHEP **12** (2008) 039, arXiv: 0808.3674 [hep-ph].

[64] S. Schumann and F. Krauss, *A parton shower algorithm based on Catani–Seymour dipole factorisation*, JHEP **03** (2008) 038, arXiv: 0709.1027 [hep-ph].

[65] S. Höche, F. Krauss, M. Schönherr and F. Siegert, *A critical appraisal of NLO+PS matching methods*, JHEP **09** (2012) 049, arXiv: 1111.1220 [hep-ph].

[66] F. Cascioli, P. Maierhöfer and S. Pozzorini, *Scattering Amplitudes with Open Loops*, Phys. Rev. Lett. **108** (2012) 111601, arXiv: 1111.5206 [hep-ph].

[67] A. Denner, S. Dittmaier and L. Hofer, *Collier: A fortran-based complex one-loop library in extended regularizations*, Comput. Phys. Commun. **212** (2017) 220, arXiv: 1604.06792 [hep-ph].

[68] F. Buccioni et al., *OpenLoops 2*, Eur. Phys. J. C **79** (2019) 866, arXiv: 1907.13071 [hep-ph].

[69] C. Anastasiou, L. Dixon, K. Melnikov and F. Petriello, *High-precision QCD at hadron colliders: Electroweak gauge boson rapidity distributions at next-to-next-to leading order*, Phys. Rev. D **69** (2004) 094008, arXiv: hep-ph/0312266.

[70] R. Frederix and I. Tsinikos, *On improving NLO merging for* $\mathrm{t\bar{t}W}$ *production*, JHEP **11** (2021) 029, arXiv: 2108.07826 [hep-ph].

[71] LHCTopWG, *NNLO+NNLL top-quark-pair cross sections*, 2015, URL: https://twiki.cern.ch/twiki/bin/view/LHCPhysics/TtbarNNLO.

[72] R. Frederix, D. Pagani and M. Zaro, *Large NLO corrections in* $t\bar{t}W^{\pm}$ *and* $t\bar{t}t\bar{t}$ *hadroproduction from supposedly subleading EW contributions*, JHEP **02** (2018) 031, arXiv: 1711.02116 [hep-ph].

[73] M. L. Ciccolini, S. Dittmaier and M. Krämer, *Electroweak radiative corrections to associated WH and ZH production at hadron colliders*, Phys. Rev. D **68** (2003) 073003, arXiv: hep-ph/0306234 [hep-ph].

[74] O. Brein, A. Djouadi and R. Harlander,
NNLO QCD corrections to the Higgs-strahlung processes at hadron colliders,
Phys. Lett. B **579** (2004) 149, arXiv: hep-ph/0307206.

[75] O. Brein, R. V. Harlander, M. Wiesemann and T. Zirke,
Top-quark mediated effects in hadronic Higgs-Strahlung, Eur. Phys. J. C **72** (2012) 1868,
arXiv: 1111.0761 [hep-ph].

[76] L. Altenkamp, S. Dittmaier, R. V. Harlander, H. Rzehak and T. J. E. Zirke,
Gluon-induced Higgs-strahlung at next-to-leading order QCD, JHEP **02** (2013) 078,
arXiv: 1211.5015 [hep-ph].

[77] A. Denner, S. Dittmaier, S. Kallweit and A. Mück, *HAWK 2.0: A Monte Carlo program for Higgs production in vector-boson fusion and Higgs strahlung at hadron colliders*,
Comput. Phys. Commun. **195** (2015) 161, arXiv: 1412.5390 [hep-ph].

[78] O. Brein, R. V. Harlander and T. J. E. Zirke, *vh@nnlo – Higgs Strahlung at hadron colliders*,
Comput. Phys. Commun. **184** (2013) 998, arXiv: 1210.5347 [hep-ph].

[79] R. V. Harlander, A. Kulesza, V. Theeuwes and T. Zirke,
Soft gluon resummation for gluon-induced Higgs Strahlung, JHEP **11** (2014) 082,
arXiv: 1410.0217 [hep-ph].

[80] C. Degrande et al., *UFO - The Universal FeynRules Output*,
Comput. Phys. Commun. **183** (2012) 1201, arXiv: 1108.2040 [hep-ph].

[81] A. Alloul, N. D. Christensen, C. Degrande, C. Duhr and B. Fuks,
FeynRules 2.0 - A complete toolbox for tree-level phenomenology,
Comput. Phys. Commun. **185** (2014) 2250, arXiv: 1310.1921 [hep-ph].

[82] I. Brivio et al., *Electroweak input parameters*, (2021), arXiv: 2111.12515 [hep-ph].

[83] ATLAS Collaboration, *Electron reconstruction and identification in the ATLAS experiment using the 2015 and 2016 LHC proton–proton collision data at* $\sqrt{s} = 13$ *TeV*,
Eur. Phys. J. C **79** (2019) 639, arXiv: 1902.04655 [physics.ins-det].

[84] ATLAS Collaboration, *Electron and photon performance measurements with the ATLAS detector using the 2015–2017 LHC proton–proton collision data*, JINST **14** (2019) P12006,
arXiv: 1908.00005 [hep-ex].

[85] ATLAS Collaboration, *Studies of the muon momentum calibration and performance of the ATLAS detector with pp collisions at* $\sqrt{s} = 13$ *TeV*, Eur. Phys. J. C **83** (2022) 686,
arXiv: 2212.07338 [hep-ex].

[86] ATLAS Collaboration, *Muon reconstruction and identification efficiency in ATLAS using the full Run 2 pp collision data set at* $\sqrt{s} = 13$ *TeV*, Eur. Phys. J. C **81** (2021) 578,
arXiv: 2012.00578 [hep-ex].

[87] M. Cacciari, G. P. Salam and G. Soyez, *The anti-k_t jet clustering algorithm*, JHEP **04** (2008) 063,
arXiv: 0802.1189 [hep-ph].

[88] M. Cacciari, G. P. Salam and G. Soyez, *FastJet user manual*, Eur. Phys. J. C **72** (2012) 1896,
arXiv: 1111.6097 [hep-ph].

[89] ATLAS Collaboration,
Jet reconstruction and performance using particle flow with the ATLAS Detector,
Eur. Phys. J. C **77** (2017) 466, arXiv: 1703.10485 [hep-ex].

[90] ATLAS Collaboration, *Jet energy scale and resolution measured in proton–proton collisions at $\sqrt{s}$ = 13 TeV with the ATLAS detector*, Eur. Phys. J. C **81** (2021) 689, arXiv: 2007.02645 [hep-ex].

[91] ATLAS Collaboration, *Performance of pile-up mitigation techniques for jets in pp collisions at $\sqrt{s}$ = 8 TeV using the ATLAS detector*, Eur. Phys. J. C **76** (2016) 581, arXiv: 1510.03823 [hep-ex].

[92] ATLAS Collaboration, *ATLAS b-jet identification performance and efficiency measurement with $t\bar{t}$ events in pp collisions at $\sqrt{s}$ = 13 TeV*, Eur. Phys. J. C **79** (2019) 970, arXiv: 1907.05120 [hep-ex].

[93] ATLAS Collaboration, *ATLAS flavour-tagging algorithms for the LHC Run 2 pp collision dataset*, Eur. Phys. J. C **83** (2023) 681, arXiv: 2211.16345 [physics.data-an].

[94] ATLAS Collaboration, *Performance of missing transverse momentum reconstruction with the ATLAS detector using proton–proton collisions at $\sqrt{s}$ = 13 TeV*, Eur. Phys. J. C **78** (2018) 903, arXiv: 1802.08168 [hep-ex].

[95] M. Cacciari, G. P. Salam and G. Soyez, *The catchment area of jets*, JHEP **04** (2008) 005, arXiv: 0802.1188 [hep-ph].

[96] F. Chollet et al., *Keras*, 2015, URL: https://keras.io.

[97] M. Abadi et al., *TensorFlow: Large-Scale Machine Learning on Heterogeneous Systems*, 2015, URL: https://www.tensorflow.org/.

[98] M. Stone, *Cross-Validatory Choice and Assessment of Statistical Predictions*, J. R. Stat. Soc. Ser. A Stat. Soc. **36** (1974) 111.

[99] Particle Data Group, *Review of Particle Physics*, PTEP **8** (2020) 083C01.

[100] A. Shmakov et al., *SPANet: Generalized permutationless set assignment for particle physics using symmetry preserving attention*, SciPost Phys. **12** (2022) 178, URL: https://arxiv.org/abs/2106.03898.

[101] ATLAS Collaboration, *Measurement of the c-jet mistagging efficiency in $t\bar{t}$ events using pp collision data at $\sqrt{s}$ = 13 TeV collected with the ATLAS detector*, Eur. Phys. J. C **82** (2022) 95, arXiv: 2109.10627 [hep-ex].

[102] ATLAS Collaboration, *Calibration of the light-flavour jet mistagging efficiency of the b-tagging algorithms with Z+jets events using 139 fb^{-1} of ATLAS proton–proton collision data at $\sqrt{s}$ = 13 TeV*, Eur. Phys. J. C **83** (2023) 728, arXiv: 2301.06319 [hep-ex].

[103] ATLAS Collaboration, *E_T^{miss} performance in the ATLAS detector using 2015–2016 LHC pp collisions*, ATLAS-CONF-2018-023, 2018, URL: https://cds.cern.ch/record/2625233.

[104] J. Butterworth et al., *PDF4LHC recommendations for LHC Run II*, J. Phys. G **43** (2016) 023001, arXiv: 1510.03865 [hep-ph].

[105] ATLAS Collaboration, *Measurements of the production cross section of a Z boson in association with jets in pp collisions at $\sqrt{s}$ = 13 TeV with the ATLAS detector*, Eur. Phys. J. C **77** (2017) 361, arXiv: 1702.05725 [hep-ex].

[106] G. Cowan, K. Cranmer, E. Gross and O. Vitells,
Asymptotic formulae for likelihood-based tests of new physics, Eur. Phys. J. C **71** (2011) 1554, arXiv: 1007.1727 [physics.data-an], Erratum: Eur. Phys. J. C **73** (2013) 2501.

[107] R. Barlow and C. Beeston, *Fitting using finite Monte Carlo samples*, Comput. Phys. Commun. **77** (1993) 219.

[108] D. L. Phillips,
A Technique for the Numerical Solution of Certain Integral Equations of the First Kind, J. ACM **9** (1962) 84.

[109] A. N. Tikhonov, *On the solution of improperly posed problems and the method of regularization*, Sov. Math. **5** (1963) 1035.

[110] R. A. Willoughby, *Solutions of Ill-Posed Problems (A. N. Tikhonov and V. Y. Arsenin)*, SIAM Review **21** (1979) 266.

[111] G. Cowan, *Statistical data analysis*, 1998, ISBN: 978-0-19-850156-5.

[112] I. Brivio et al., *O new physics, where art thou? A global search in the top sector*, JHEP **02** (2020) 131, arXiv: 1910.03606 [hep-ph].

[113] J. A. Aguilar-Saavedra et al.,
Interpreting top-quark LHC measurements in the standard-model effective field theory, (2018), arXiv: 1802.07237 [hep-ph].

[114] CMS Collaboration, *Search for physics beyond the standard model in top quark production with additional leptons in the context of effective field theory*, (2023), arXiv: 2307.15761 [hep-ex].

[115] J. Brehmer, K. Cranmer, F. Kling and T. Plehn,
Better Higgs boson measurements through information geometry, Phys. Rev. D **95** (2017) 073002, arXiv: 1612.05261 [hep-ph].

[116] N. Castro, J. Erdmann, C. Grunwald, K. Kröninger and N.-A. Rosien,
EFTfitter—A tool for interpreting measurements in the context of effective field theories, Eur. Phys. J. C **76** (2016) 432, arXiv: 1605.05585 [hep-ex].

[117] O. Schulz et al., *BAT.jl: A Julia-Based Tool for Bayesian Inference*, SN Comput. Sci. **2** (2021) 1, arXiv: 2008.03132 [stat.CO].

[118] O. B. Bylund, F. Maltoni, I. Tsinikos, E. Vryonidou and C. Zhang,
Probing top quark neutral couplings in the Standard Model Effective Field Theory at NLO in QCD, JHEP **05** (2016) 052, arXiv: 1601.08193 [hep-ph].

[119] ATLAS Collaboration, *ATLAS Computing Acknowledgements*, ATL-SOFT-PUB-2023-001, 2023, URL: https://cds.cern.ch/record/2869272.

The ATLAS Collaboration

G. Aad [102], B. Abbott [120], K. Abeling [55], N.J. Abicht [49], S.H. Abidi [29], A. Aboulhorma [35e], H. Abramowicz [151], H. Abreu [150], Y. Abulaiti [117], B.S. Acharya [69a,69b,m], C. Adam Bourdarios [4], L. Adamczyk [86a], S.V. Addepalli [26], M.J. Addison [101], J. Adelman [115], A. Adiguzel [21c], T. Adye [134], A.A. Affolder [136], Y. Afik [39], M.N. Agaras [13], J. Agarwala [73a,73b], A. Aggarwal [100], C. Agheorghiesei [27c], A. Ahmad [36], F. Ahmadov [38,z], W.S. Ahmed [104], S. Ahuja [95], X. Ai [62e], G. Aielli [76a,76b], A. Aikot [163], M. Ait Tamlihat [35e], B. Aitbenchikh [35a], I. Aizenberg [169], M. Akbiyik [100], T.P.A. Åkesson [98], A.V. Akimov [37], D. Akiyama [168], N.N. Akolkar [24], S. Aktas [21a], K. Al Khoury [41], G.L. Alberghi [23b], J. Albert [165], P. Albicocco [53], G.L. Albouy [60], S. Alderweireldt [52], Z.L. Alegria [121], M. Aleksa [36], I.N. Aleksandrov [38], C. Alexa [27b], T. Alexopoulos [10], F. Alfonsi [23b], M. Algren [56], M. Alhroob [120], B. Ali [132], H.M.J. Ali [91], S. Ali [148], S.W. Alibocus [92], M. Aliev [145], G. Alimonti [71a], W. Alkakhi [55], C. Allaire [66], B.M.M. Allbrooke [146], J.F. Allen [52], C.A. Allendes Flores [137f], P.P. Allport [20], A. Aloisio [72a,72b], F. Alonso [90], C. Alpigiani [138], M. Alvarez Estevez [99], A. Alvarez Fernandez [100], M. Alves Cardoso [56], M.G. Alviggi [72a,72b], M. Aly [101], Y. Amaral Coutinho [83b], A. Ambler [104], C. Amelung[36], M. Amerl [101], C.G. Ames [109], D. Amidei [106], S.P. Amor Dos Santos [130a], K.R. Amos [163], V. Ananiev [125], C. Anastopoulos [139], T. Andeen [11], J.K. Anders [36], S.Y. Andrean [47a,47b], A. Andreazza [71a,71b], S. Angelidakis [9], A. Angerami [41,ac], A.V. Anisenkov [37], A. Annovi [74a], C. Antel [56], M.T. Anthony [139], E. Antipov [145], M. Antonelli [53], F. Anulli [75a], M. Aoki [84], T. Aoki [153], J.A. Aparisi Pozo [163], M.A. Aparo [146], L. Aperio Bella [48], C. Appelt [18], A. Apyan [26], N. Aranzabal [36], S.J. Arbiol Val [87], C. Arcangeletti [53], A.T.H. Arce [51], E. Arena [92], J-F. Arguin [108], S. Argyropoulos [54], J.-H. Arling [48], O. Arnaez [4], H. Arnold [114], G. Artoni [75a,75b], H. Asada [111], K. Asai [118], S. Asai [153], N.A. Asbah [61], J. Assahsah [35d], K. Assamagan [29], R. Astalos [28a], S. Atashi [159], R.J. Atkin [33a], M. Atkinson[162], H. Atmani[35f], P.A. Atmasiddha [128], K. Augsten [132], S. Auricchio [72a,72b], A.D. Auriol [20], V.A. Austrup [101], G. Avolio [36], K. Axiotis [56], G. Azuelos [108,ag], D. Babal [28b], H. Bachacou [135], K. Bachas [152,q], A. Bachiu [34], F. Backman [47a,47b], A. Badea [61], T.M. Baer [106], P. Bagnaia [75a,75b], M. Bahmani [18], D. Bahner [54], A.J. Bailey [163], V.R. Bailey [162], J.T. Baines [134], L. Baines [94], O.K. Baker [172], E. Bakos [15], D. Bakshi Gupta [8], V. Balakrishnan [120], R. Balasubramanian [114], E.M. Baldin [37], P. Balek [86a], E. Ballabene [23b,23a], F. Balli [135], L.M. Baltes [63a], W.K. Balunas [32], J. Balz [100], E. Banas [87], M. Bandieramonte [129], A. Bandyopadhyay [24], S. Bansal [24], L. Barak [151], M. Barakat [48], E.L. Barberio [105], D. Barberis [57b,57a], M. Barbero [102], M.Z. Barel [114], K.N. Barends [33a], T. Barillari [110], M-S. Barisits [36], T. Barklow [143], P. Baron [122], D.A. Baron Moreno [101], A. Baroncelli [62a], G. Barone [29], A.J. Barr [126], J.D. Barr [96], L. Barranco Navarro [47a,47b], F. Barreiro [99], J. Barreiro Guimarães da Costa [14a], U. Barron [151], M.G. Barros Teixeira [130a], S. Barsov [37], F. Bartels [63a], R. Bartoldus [143], A.E. Barton [91], P. Bartos [28a], A. Basan [100], M. Baselga [49], A. Bassalat [66,b], M.J. Basso [156a], C.R. Basson [101], R.L. Bates [59], S. Batlamous[35e], J.R. Batley [32], B. Batool [141], M. Battaglia [136], D. Battulga [18], M. Bauce [75a,75b], M. Bauer [36], P. Bauer [24], L.T. Bazzano Hurrell [30], J.B. Beacham [51], T. Beau [127], J.Y. Beaucamp [90], P.H. Beauchemin [158], P. Bechtle [24], H.P. Beck [19,p], K. Becker [167], A.J. Beddall [82], V.A. Bednyakov [38], C.P. Bee [145], L.J. Beemster [15], T.A. Beermann [36], M. Begalli [83d], M. Begel [29], A. Behera [145], J.K. Behr [48], J.F. Beirer [36], F. Beisiegel [24], M. Belfkir [116b], G. Bella [151], L. Bellagamba [23b], A. Bellerive [34], P. Bellos [20], K. Beloborodov [37], D. Benchekroun [35a], F. Bendebba [35a], Y. Benhammou [151], M. Benoit [29],

J.R. Bensinger[26], S. Bentvelsen[114], L. Beresford[48], M. Beretta[53], E. Bergeaas Kuutmann[161], N. Berger[4], B. Bergmann[132], J. Beringer[17a], G. Bernardi[5], C. Bernius[143], F.U. Bernlochner[24], F. Bernon[36,102], A. Berrocal Guardia[13], T. Berry[95], P. Berta[133], A. Berthold[50], I.A. Bertram[91], S. Bethke[110], A. Betti[75a,75b], A.J. Bevan[94], N.K. Bhalla[54], M. Bhamjee[33c], S. Bhatta[145], D.S. Bhattacharya[166], P. Bhattarai[143], V.S. Bhopatkar[121], R. Bi[29,aj], R.M. Bianchi[129], G. Bianco[23b,23a], O. Biebel[109], R. Bielski[123], M. Biglietti[77a], M. Bindi[55], A. Bingul[21b], C. Bini[75a,75b], A. Biondini[92], C.J. Birch-sykes[101], G.A. Bird[20,134], M. Birman[169], M. Biros[133], S. Biryukov[146], T. Bisanz[49], E. Bisceglie[43b,43a], J.P. Biswal[134], D. Biswas[141], A. Bitadze[101], K. Bjørke[125], I. Bloch[48], A. Blue[59], U. Blumenschein[94], J. Blumenthal[100], G.J. Bobbink[114], V.S. Bobrovnikov[37], M. Boehler[54], B. Boehm[166], D. Bogavac[36], A.G. Bogdanchikov[37], C. Bohm[47a], V. Boisvert[95], P. Bokan[48], T. Bold[86a], M. Bomben[5], M. Bona[94], M. Boonekamp[135], C.D. Booth[95], A.G. Borbély[59], I.S. Bordulev[37], H.M. Borecka-Bielska[108], G. Borissov[91], D. Bortoletto[126], D. Boscherini[23b], M. Bosman[13], J.D. Bossio Sola[36], K. Bouaouda[35a], N. Bouchhar[163], J. Boudreau[129], E.V. Bouhova-Thacker[91], D. Boumediene[40], R. Bouquet[165], A. Boveia[119], J. Boyd[36], D. Boye[29], I.R. Boyko[38], J. Bracinik[20], N. Brahimi[62d], G. Brandt[171], O. Brandt[32], F. Braren[48], B. Brau[103], J.E. Brau[123], R. Brener[169], L. Brenner[114], R. Brenner[161], S. Bressler[169], D. Britton[59], D. Britzger[110], I. Brock[24], G. Brooijmans[41], W.K. Brooks[137f], E. Brost[29], L.M. Brown[165], L.E. Bruce[61], T.L. Bruckler[126], P.A. Bruckman de Renstrom[87], B. Brüers[48], A. Bruni[23b], G. Bruni[23b], M. Bruschi[23b], N. Bruscino[75a,75b], T. Buanes[16], Q. Buat[138], D. Buchin[110], A.G. Buckley[59], O. Bulekov[37], B.A. Bullard[143], S. Burdin[92], C.D. Burgard[49], A.M. Burger[40], B. Burghgrave[8], O. Burlayenko[54], J.T.P. Burr[32], C.D. Burton[11], J.C. Burzynski[142], E.L. Busch[41], V. Büscher[100], P.J. Bussey[59], J.M. Butler[25], C.M. Buttar[59], J.M. Butterworth[96], W. Buttinger[134], C.J. Buxo Vazquez[107], A.R. Buzykaev[37], S. Cabrera Urbán[163], L. Cadamuro[66], D. Caforio[58], H. Cai[129], Y. Cai[14a,14e], Y. Cai[14c], V.M.M. Cairo[36], O. Cakir[3a], N. Calace[36], P. Calafiura[17a], G. Calderini[127], P. Calfayan[68], G. Callea[59], L.P. Caloba[83b], D. Calvet[40], S. Calvet[40], M. Calvetti[74a,74b], R. Camacho Toro[127], S. Camarda[36], D. Camarero Munoz[26], P. Camarri[76a,76b], M.T. Camerlingo[72a,72b], D. Cameron[36], C. Camincher[165], M. Campanelli[96], A. Camplani[42], V. Canale[72a,72b], A. Canesse[104], J. Cantero[163], Y. Cao[162], F. Capocasa[26], M. Capua[43b,43a], A. Carbone[71a,71b], R. Cardarelli[76a], J.C.J. Cardenas[8], F. Cardillo[163], G. Carducci[43b,43a], T. Carli[36], G. Carlino[72a], J.I. Carlotto[13], B.T. Carlson[129,r], E.M. Carlson[165,156a], L. Carminati[71a,71b], A. Carnelli[135], M. Carnesale[75a,75b], S. Caron[113], E. Carquin[137f], S. Carrá[71a], G. Carratta[23b,23a], F. Carrio Argos[33g], J.W.S. Carter[155], T.M. Carter[52], M.P. Casado[13,i], M. Caspar[48], F.L. Castillo[4], L. Castillo Garcia[13], V. Castillo Gimenez[163], N.F. Castro[130a,130e], A. Catinaccio[36], J.R. Catmore[125], V. Cavaliere[29], N. Cavalli[23b,23a], V. Cavasinni[74a,74b], Y.C. Cekmecelioglu[48], E. Celebi[21a], F. Celli[126], M.S. Centonze[70a,70b], V. Cepaitis[56], K. Cerny[122], A.S. Cerqueira[83a], A. Cerri[146], L. Cerrito[76a,76b], F. Cerutti[17a], B. Cervato[141], A. Cervelli[23b], G. Cesarini[53], S.A. Cetin[82], D. Chakraborty[115], J. Chan[170], W.Y. Chan[153], J.D. Chapman[32], E. Chapon[135], B. Chargeishvili[149b], D.G. Charlton[20], M. Chatterjee[19], C. Chauhan[133], S. Chekanov[6], S.V. Chekulaev[156a], G.A. Chelkov[38,a], A. Chen[106], B. Chen[151], B. Chen[165], H. Chen[14c], H. Chen[29], J. Chen[62c], J. Chen[142], M. Chen[126], S. Chen[153], S.J. Chen[14c], X. Chen[62c,135], X. Chen[14b,af], Y. Chen[62a], C.L. Cheng[170], H.C. Cheng[64a], S. Cheong[143], A. Cheplakov[38], E. Cheremushkina[48], E. Cherepanova[114], R. Cherkaoui El Moursli[35e], E. Cheu[7], K. Cheung[65], L. Chevalier[135], V. Chiarella[53], G. Chiarelli[74a], N. Chiedde[102], G. Chiodini[70a], A.S. Chisholm[20], A. Chitan[27b], M. Chitishvili[163], M.V. Chizhov[38], K. Choi[11], A.R. Chomont[75a,75b], Y. Chou[103],

E.Y.S. Chow [113], T. Chowdhury [33g], K.L. Chu[169], M.C. Chu [64a], X. Chu [14a,14e], J. Chudoba [131], J.J. Chwastowski [87], D. Cieri [110], K.M. Ciesla [86a], V. Cindro [93], A. Ciocio [17a], F. Cirotto [72a,72b], Z.H. Citron [169,k], M. Citterio [71a], D.A. Ciubotaru[27b], A. Clark [56], P.J. Clark [52], C. Clarry [155], J.M. Clavijo Columbie [48], S.E. Clawson [48], C. Clement [47a,47b], J. Clercx [48], Y. Coadou [102], M. Cobal [69a,69c], A. Coccaro [57b], R.F. Coelho Barrue [130a], R. Coelho Lopes De Sa [103], S. Coelli [71a], A.E.C. Coimbra [71a,71b], B. Cole [41], J. Collot [60], P. Conde Muiño [130a,130g], M.P. Connell [33c], S.H. Connell [33c], I.A. Connelly [59], E.I. Conroy [126], F. Conventi [72a,ah], H.G. Cooke [20], A.M. Cooper-Sarkar [126], A. Cordeiro Oudot Choi [127], L.D. Corpe [40], M. Corradi [75a,75b], F. Corriveau [104,x], A. Cortes-Gonzalez [18], M.J. Costa [163], F. Costanza [4], D. Costanzo [139], B.M. Cote [119], G. Cowan [95], K. Cranmer [170], D. Cremonini [23b,23a], S. Crépé-Renaudin [60], F. Crescioli [127], M. Cristinziani [141], M. Cristoforetti [78a,78b], V. Croft [114], J.E. Crosby [121], G. Crosetti [43b,43a], A. Cueto [99], T. Cuhadar Donszelmann [159], H. Cui [14a,14e], Z. Cui [7], W.R. Cunningham [59], F. Curcio [43b,43a], P. Czodrowski [36], M.M. Czurylo [63b], M.J. Da Cunha Sargedas De Sousa [57b,57a], J.V. Da Fonseca Pinto [83b], C. Da Via [101], W. Dabrowski [86a], T. Dado [49], S. Dahbi [33g], T. Dai [106], D. Dal Santo [19], C. Dallapiccola [103], M. Dam [42], G. D'amen [29], V. D'Amico [109], J. Damp [100], J.R. Dandoy [34], M. Danninger [142], V. Dao [36], G. Darbo [57b], S. Darmora [6], S.J. Das [29,aj], S. D'Auria [71a,71b], C. David [156b], T. Davidek [133], B. Davis-Purcell [34], I. Dawson [94], H.A. Day-hall [132], K. De [8], R. De Asmundis [72a], N. De Biase [48], S. De Castro [23b,23a], N. De Groot [113], P. de Jong [114], H. De la Torre [115], A. De Maria [14c], A. De Salvo [75a], U. De Sanctis [76a,76b], F. De Santis [70a,70b], A. De Santo [146], J.B. De Vivie De Regie [60], D.V. Dedovich[38], J. Degens [114], A.M. Deiana [44], F. Del Corso [23b,23a], J. Del Peso [99], F. Del Rio [63a], L. Delagrange [127], F. Deliot [135], C.M. Delitzsch [49], M. Della Pietra [72a,72b], D. Della Volpe [56], A. Dell'Acqua [36], L. Dell'Asta [71a,71b], M. Delmastro [4], P.A. Delsart [60], S. Demers [172], M. Demichev [38], S.P. Denisov [37], L. D'Eramo [40], D. Derendarz [87], F. Derue [127], P. Dervan [92], K. Desch [24], C. Deutsch [24], F.A. Di Bello [57b,57a], A. Di Ciaccio [76a,76b], L. Di Ciaccio [4], A. Di Domenico [75a,75b], C. Di Donato [72a,72b], A. Di Girolamo [36], G. Di Gregorio [36], A. Di Luca [78a,78b], B. Di Micco [77a,77b], R. Di Nardo [77a,77b], C. Diaconu [102], M. Diamantopoulou [34], F.A. Dias [114], T. Dias Do Vale [142], M.A. Diaz [137a,137b], F.G. Diaz Capriles [24], M. Didenko [163], E.B. Diehl [106], L. Diehl [54], S. Díez Cornell [48], C. Diez Pardos [141], C. Dimitriadi [161,24], A. Dimitrievska [17a], J. Dingfelder [24], I-M. Dinu [27b], S.J. Dittmeier [63b], F. Dittus [36], F. Djama [102], T. Djobava [149b], C. Doglioni [101,98], A. Dohnalova [28a], J. Dolejsi [133], Z. Dolezal [133], K.M. Dona [39], M. Donadelli [83c], B. Dong [107], J. Donini [40], A. D'Onofrio [72a,72b], M. D'Onofrio [92], J. Dopke [134], A. Doria [72a], N. Dos Santos Fernandes [130a], P. Dougan [101], M.T. Dova [90], A.T. Doyle [59], M.A. Draguet [126], E. Dreyer [169], I. Drivas-koulouris [10], M. Drnevich [117], A.S. Drobac [158], M. Drozdova [56], D. Du [62a], T.A. du Pree [114], F. Dubinin [37], M. Dubovsky [28a], E. Duchovni [169], G. Duckeck [109], O.A. Ducu [27b], D. Duda [52], A. Dudarev [36], E.R. Duden [26], M. D'uffizi [101], L. Duflot [66], M. Dührssen [36], A.E. Dumitriu [27b], M. Dunford [63a], S. Dungs [49], K. Dunne [47a,47b], A. Duperrin [102], H. Duran Yildiz [3a], M. Düren [58], A. Durglishvili [149b], B.L. Dwyer [115], G.I. Dyckes [17a], M. Dyndal [86a], B.S. Dziedzic [87], Z.O. Earnshaw [146], G.H. Eberwein [126], B. Eckerova [28a], S. Eggebrecht [55], E. Egidio Purcino De Souza [127], L.F. Ehrke [56], G. Eigen [16], K. Einsweiler [17a], T. Ekelof [161], P.A. Ekman [98], S. El Farkh [35b], Y. El Ghazali [35b], H. El Jarrari [36], A. El Moussaouy [108], V. Ellajosyula [161], M. Ellert [161], F. Ellinghaus [171], N. Ellis [36], J. Elmsheuser [29], M. Elsing [36], D. Emeliyanov [134], Y. Enari [153], I. Ene [17a], S. Epari [13], P.A. Erland [87], M. Errenst [171], M. Escalier [66], C. Escobar [163], E. Etzion [151], G. Evans [130a], H. Evans [68], L.S. Evans [95], M.O. Evans [146], A. Ezhilov [37], S. Ezzarqtouni [35a],

F. Fabbri [59], L. Fabbri [23b,23a], G. Facini [96], V. Fadeyev [136], R.M. Fakhrutdinov [37], D. Fakoudis [100], S. Falciano [75a], L.F. Falda Ulhoa Coelho [36], P.J. Falke [24], J. Faltova [133], C. Fan [162], Y. Fan [14a], Y. Fang [14a,14e], M. Fanti [71a,71b], M. Faraj [69a,69b], Z. Farazpay [97], A. Farbin [8], A. Farilla [77a], T. Farooque [107], S.M. Farrington [52], F. Fassi [35e], D. Fassouliotis [9], M. Faucci Giannelli [76a,76b], W.J. Fawcett [32], L. Fayard [66], P. Federic [133], P. Federicova [131], O.L. Fedin [37,a], G. Fedotov [37], M. Feickert [170], L. Feligioni [102], D.E. Fellers [123], C. Feng [62b], M. Feng [14b], Z. Feng [114], M.J. Fenton [159], A.B. Fenyuk[37], L. Ferencz [48], R.A.M. Ferguson [91], S.I. Fernandez Luengo [137f], P. Fernandez Martinez [13], M.J.V. Fernoux [102], J. Ferrando [91], A. Ferrari [161], P. Ferrari [114,113], R. Ferrari [73a], D. Ferrere [56], C. Ferretti [106], F. Fiedler [100], P. Fiedler [132], A. Filipčič [93], E.K. Filmer [1], F. Filthaut [113], M.C.N. Fiolhais [130a,130c,c], L. Fiorini [163], W.C. Fisher [107], T. Fitschen [101], P.M. Fitzhugh[135], I. Fleck [141], P. Fleischmann [106], T. Flick [171], M. Flores [33d,ad], L.R. Flores Castillo [64a], L. Flores Sanz De Acedo [36], F.M. Follega [78a,78b], N. Fomin [16], J.H. Foo [155], A. Formica [135], A.C. Forti [101], E. Fortin [36], A.W. Fortman [61], M.G. Foti [17a], L. Fountas [9,j], D. Fournier [66], H. Fox [91], P. Francavilla [74a,74b], S. Francescato [61], S. Franchellucci [56], M. Franchini [23b,23a], S. Franchino [63a], D. Francis[36], L. Franco [113], V. Franco Lima [36], L. Franconi [48], M. Franklin [61], G. Frattari [26], A.C. Freegard [94], W.S. Freund [83b], Y.Y. Frid [151], J. Friend [59], N. Fritzsche [50], A. Froch [54], D. Froidevaux [36], J.A. Frost [126], Y. Fu [62a], S. Fuenzalida Garrido [137f], M. Fujimoto [102], K.Y. Fung [64a], E. Furtado De Simas Filho [83b], M. Furukawa [153], J. Fuster [163], A. Gabrielli [23b,23a], A. Gabrielli [155], P. Gadow [36], G. Gagliardi [57b,57a], L.G. Gagnon [17a], E.J. Gallas [126], B.J. Gallop [134], K.K. Gan [119], S. Ganguly [153], Y. Gao [52], F.M. Garay Walls [137a,137b], B. Garcia[29], C. García [163], A. Garcia Alonso [114], A.G. Garcia Caffaro [172], J.E. García Navarro [163], M. Garcia-Sciveres [17a], G.L. Gardner [128], R.W. Gardner [39], N. Garelli [158], D. Garg [80], R.B. Garg [143,n], J.M. Gargan[52], C.A. Garner[155], C.M. Garvey [33a], P. Gaspar [83b], V.K. Gassmann[158], G. Gaudio [73a], V. Gautam[13], P. Gauzzi [75a,75b], I.L. Gavrilenko [37], A. Gavrilyuk [37], C. Gay [164], G. Gaycken [48], E.N. Gazis [10], A.A. Geanta [27b], C.M. Gee [136], A. Gekow[119], C. Gemme [57b], M.H. Genest [60], S. Gentile [75a,75b], A.D. Gentry [112], S. George [95], W.F. George [20], T. Geralis [46], P. Gessinger-Befurt [36], M.E. Geyik [171], M. Ghani [167], M. Ghneimat [141], K. Ghorbanian [94], A. Ghosal [141], A. Ghosh [159], A. Ghosh [7], B. Giacobbe [23b], S. Giagu [75a,75b], T. Giani [114], P. Giannetti [74a], A. Giannini [62a], S.M. Gibson [95], M. Gignac [136], D.T. Gil [86b], A.K. Gilbert [86a], B.J. Gilbert [41], D. Gillberg [34], G. Gilles [114], N.E.K. Gillwald [48], L. Ginabat [127], D.M. Gingrich [2,ag], M.P. Giordani [69a,69c], P.F. Giraud [135], G. Giugliarelli [69a,69c], D. Giugni [71a], F. Giuli [36], I. Gkialas [9,j], L.K. Gladilin [37], C. Glasman [99], G.R. Gledhill [123], G. Glemža [48], M. Glisic[123], I. Gnesi [43b,f], Y. Go [29], M. Goblirsch-Kolb [36], B. Gocke [49], D. Godin[108], B. Gokturk [21a], S. Goldfarb [105], T. Golling [56], M.G.D. Gololo[33g], D. Golubkov [37], J.P. Gombas [107], A. Gomes [130a,130b], G. Gomes Da Silva [141], A.J. Gomez Delegido [163], R. Gonçalo [130a,130c], G. Gonella [123], L. Gonella [20], A. Gongadze [149c], F. Gonnella [20], J.L. Gonski [41], R.Y. González Andana [52], S. González de la Hoz [163], R. Gonzalez Lopez [92], C. Gonzalez Renteria [17a], M.V. Gonzalez Rodrigues [48], R. Gonzalez Suarez [161], S. Gonzalez-Sevilla [56], G.R. Gonzalvo Rodriguez [163], L. Goossens [36], B. Gorini [36], E. Gorini [70a,70b], A. Gorišek [93], T.C. Gosart [128], A.T. Goshaw [51], M.I. Gostkin [38], S. Goswami [121], C.A. Gottardo [36], S.A. Gotz [109], M. Gouighri [35b], V. Goumarre [48], A.G. Goussiou [138], N. Govender [33c], I. Grabowska-Bold [86a], K. Graham [34], E. Gramstad [125], S. Grancagnolo [70a,70b], M. Grandi [146], C.M. Grant[1,135], P.M. Gravila [27f], F.G. Gravili [70a,70b], H.M. Gray [17a], M. Greco [70a,70b], C. Grefe [24], I.M. Gregor [48], P. Grenier [143], S.G. Grewe[110], C. Grieco [13], A.A. Grillo [136], K. Grimm [31], S. Grinstein [13,t], J.-F. Grivaz [66], E. Gross [169], J. Grosse-Knetter [55], C. Grud[106], J.C. Grundy [126], L. Guan [106], W. Guan [29], C. Gubbels [164],

J.G.R. Guerrero Rojas[163], G. Guerrieri[69a,69c], F. Guescini[110], R. Gugel[100], J.A.M. Guhit[106], A. Guida[18], E. Guilloton[167,134], S. Guindon[36], F. Guo[14a,14e], J. Guo[62c], L. Guo[48], Y. Guo[106], R. Gupta[48], R. Gupta[129], S. Gurbuz[24], S.S. Gurdasani[54], G. Gustavino[36], M. Guth[56], P. Gutierrez[120], L.F. Gutierrez Zagazeta[128], M. Gutsche[50], C. Gutschow[96], C. Gwenlan[126], C.B. Gwilliam[92], E.S. Haaland[125], A. Haas[117], M. Habedank[48], C. Haber[17a], H.K. Hadavand[8], A. Hadef[50], S. Hadzic[110], A.I. Hagan[91], J.J. Hahn[141], E.H. Haines[96], M. Haleem[166], J. Haley[121], J.J. Hall[139], G.D. Hallewell[102], L. Halser[19], K. Hamano[165], M. Hamer[24], G.N. Hamity[52], E.J. Hampshire[95], J. Han[62b], K. Han[62a], L. Han[14c], L. Han[62a], S. Han[17a], Y.F. Han[155], K. Hanagaki[84], M. Hance[136], D.A. Hangal[41,ac], H. Hanif[142], M.D. Hank[128], J.B. Hansen[42], P.H. Hansen[42], K. Hara[157], D. Harada[56], T. Harenberg[171], S. Harkusha[37], M.L. Harris[103], Y.T. Harris[126], J. Harrison[13], N.M. Harrison[119], P.F. Harrison[167], N.M. Hartman[110], N.M. Hartmann[109], Y. Hasegawa[140], R. Hauser[107], C.M. Hawkes[20], R.J. Hawkings[36], Y. Hayashi[153], S. Hayashida[111], D. Hayden[107], C. Hayes[106], R.L. Hayes[114], C.P. Hays[126], J.M. Hays[94], H.S. Hayward[92], F. He[62a], M. He[14a,14e], Y. He[154], Y. He[48], N.B. Heatley[94], V. Hedberg[98], A.L. Heggelund[125], N.D. Hehir[94], C. Heidegger[54], K.K. Heidegger[54], W.D. Heidorn[81], J. Heilman[34], S. Heim[48], T. Heim[17a], J.G. Heinlein[128], J.J. Heinrich[123], L. Heinrich[110,ae], J. Hejbal[131], L. Helary[48], A. Held[170], S. Hellesund[16], C.M. Helling[164], S. Hellman[47a,47b], R.C.W. Henderson[91], L. Henkelmann[32], A.M. Henriques Correia[36], H. Herde[98], Y. Hernández Jiménez[145], L.M. Herrmann[24], T. Herrmann[50], G. Herten[54], R. Hertenberger[109], L. Hervas[36], M.E. Hesping[100], N.P. Hessey[156a], H. Hibi[85], E. Hill[155], S.J. Hillier[20], J.R. Hinds[107], F. Hinterkeuser[24], M. Hirose[124], S. Hirose[157], D. Hirschbuehl[171], T.G. Hitchings[101], B. Hiti[93], J. Hobbs[145], R. Hobincu[27e], N. Hod[169], M.C. Hodgkinson[139], B.H. Hodkinson[32], A. Hoecker[36], D.D. Hofer[106], J. Hofer[48], T. Holm[24], M. Holzbock[110], L.B.A.H. Hommels[32], B.P. Honan[101], J. Hong[62c], T.M. Hong[129], B.H. Hooberman[162], W.H. Hopkins[6], Y. Horii[111], S. Hou[148], A.S. Howard[93], J. Howarth[59], J. Hoya[6], M. Hrabovsky[122], A. Hrynevich[48], T. Hryn'ova[4], P.J. Hsu[65], S.-C. Hsu[138], Q. Hu[62a], Y.F. Hu[14a,14e], S. Huang[64b], X. Huang[14c], X. Huang[14a,14e], Y. Huang[139], Y. Huang[14a], Z. Huang[101], Z. Hubacek[132], M. Huebner[24], F. Huegging[24], T.B. Huffman[126], C.A. Hugli[48], M. Huhtinen[36], S.K. Huiberts[16], R. Hulsken[104], N. Huseynov[12], J. Huston[107], J. Huth[61], R. Hyneman[143], G. Iacobucci[56], G. Iakovidis[29], I. Ibragimov[141], L. Iconomidou-Fayard[66], J.P. Iddon[36], P. Iengo[72a,72b], R. Iguchi[153], T. Iizawa[126], Y. Ikegami[84], N. Ilic[155], H. Imam[35a], M. Ince Lezki[56], T. Ingebretsen Carlson[47a,47b], G. Introzzi[73a,73b], M. Iodice[77a], V. Ippolito[75a,75b], R.K. Irwin[92], M. Ishino[153], W. Islam[170], C. Issever[18,48], S. Istin[21a,al], H. Ito[168], J.M. Iturbe Ponce[64a], R. Iuppa[78a,78b], A. Ivina[169], J.M. Izen[45], V. Izzo[72a], P. Jacka[131,132], P. Jackson[1], R.M. Jacobs[48], B.P. Jaeger[142], C.S. Jagfeld[109], G. Jain[156a], P. Jain[54], K. Jakobs[54], T. Jakoubek[169], J. Jamieson[59], K.W. Janas[86a], M. Javurkova[103], F. Jeanneau[135], L. Jeanty[123], J. Jejelava[149a,aa], P. Jenni[54,g], C.E. Jessiman[34], S. Jézéquel[4], C. Jia[62b], J. Jia[145], X. Jia[61], X. Jia[14a,14e], Z. Jia[14c], S. Jiggins[48], J. Jimenez Pena[13], S. Jin[14c], A. Jinaru[27b], O. Jinnouchi[154], P. Johansson[139], K.A. Johns[7], J.W. Johnson[136], D.M. Jones[32], E. Jones[48], P. Jones[32], R.W.L. Jones[91], T.J. Jones[92], H.L. Joos[55,36], R. Joshi[119], J. Jovicevic[15], X. Ju[17a], J.J. Junggeburth[103], T. Junkermann[63a], A. Juste Rozas[13,t], M.K. Juzek[87], S. Kabana[137e], A. Kaczmarska[87], M. Kado[110], H. Kagan[119], M. Kagan[143], A. Kahn[41], A. Kahn[128], C. Kahra[100], T. Kaji[153], E. Kajomovitz[150], N. Kakati[169], I. Kalaitzidou[54], C.W. Kalderon[29], A. Kamenshchikov[155], N.J. Kang[136], D. Kar[33g], K. Karava[126], M.J. Kareem[156b], E. Karentzos[54], I. Karkanias[152], O. Karkout[114], S.N. Karpov[38], Z.M. Karpova[38], V. Kartvelishvili[91], A.N. Karyukhin[37],

E. Kasimi[152], J. Katzy[48], S. Kaur[34], K. Kawade[140], M.P. Kawale[120], C. Kawamoto[88], T. Kawamoto[62a], E.F. Kay[36], F.I. Kaya[158], S. Kazakos[107], V.F. Kazanin[37], Y. Ke[145], J.M. Keaveney[33a], R. Keeler[165], G.V. Kehris[61], J.S. Keller[34], A.S. Kelly[96], J.J. Kempster[146], K.E. Kennedy[41], P.D. Kennedy[100], O. Kepka[131], B.P. Kerridge[167], S. Kersten[171], B.P. Kerševan[93], S. Keshri[66], L. Keszeghova[28a], S. Ketabchi Haghighat[155], R.A. Khan[129], A. Khanov[121], A.G. Kharlamov[37], T. Kharlamova[37], E.E. Khoda[138], M. Kholodenko[37], T.J. Khoo[18], G. Khoriauli[166], J. Khubua[149b], Y.A.R. Khwaira[66], A. Kilgallon[123], D.W. Kim[47a,47b], Y.K. Kim[39], N. Kimura[96], M.K. Kingston[55], A. Kirchhoff[55], C. Kirfel[24], F. Kirfel[24], J. Kirk[134], A.E. Kiryunin[110], C. Kitsaki[10], O. Kivernyk[24], M. Klassen[63a], C. Klein[34], L. Klein[166], M.H. Klein[44], M. Klein[92], S.B. Klein[56], U. Klein[92], P. Klimek[36], A. Klimentov[29], T. Klioutchnikova[36], P. Kluit[114], S. Kluth[110], E. Kneringer[79], T.M. Knight[155], A. Knue[49], R. Kobayashi[88], D. Kobylianskii[169], S.F. Koch[126], M. Kocian[143], P. Kodyš[133], D.M. Koeck[123], P.T. Koenig[24], T. Koffas[34], O. Kolay[50], I. Koletsou[4], T. Komarek[122], K. Köneke[54], A.X.Y. Kong[1], T. Kono[118], N. Konstantinidis[96], P. Kontaxakis[56], B. Konya[98], R. Kopeliansky[68], S. Koperny[86a], K. Korcyl[87], K. Kordas[152,e], A. Korn[96], S. Korn[55], I. Korolkov[13], N. Korotkova[37], B. Kortman[114], O. Kortner[110], S. Kortner[110], W.H. Kostecka[115], V.V. Kostyukhin[141], A. Kotsokechagia[135], A. Kotwal[51], A. Koulouris[36], A. Kourkoumeli-Charalampidi[73a,73b], C. Kourkoumelis[9], E. Kourlitis[110,ae], O. Kovanda[146], R. Kowalewski[165], W. Kozanecki[135], A.S. Kozhin[37], V.A. Kramarenko[37], G. Kramberger[93], P. Kramer[100], M.W. Krasny[127], A. Krasznahorkay[36], J.W. Kraus[171], J.A. Kremer[48], T. Kresse[50], J. Kretzschmar[92], K. Kreul[18], P. Krieger[155], S. Krishnamurthy[103], M. Krivos[133], K. Krizka[20], K. Kroeninger[49], H. Kroha[110], J. Kroll[131], J. Kroll[128], K.S. Krowpman[107], U. Kruchonak[38], H. Krüger[24], N. Krumnack[81], M.C. Kruse[51], O. Kuchinskaia[37], S. Kuday[3a], S. Kuehn[36], R. Kuesters[54], T. Kuhl[48], V. Kukhtin[38], Y. Kulchitsky[37,a], S. Kuleshov[137d,137b], M. Kumar[33g], N. Kumari[48], P. Kumari[156b], A. Kupco[131], T. Kupfer[49], A. Kupich[37], O. Kuprash[54], H. Kurashige[85], L.L. Kurchaninov[156a], O. Kurdysh[66], Y.A. Kurochkin[37], A. Kurova[37], M. Kuze[154], A.K. Kvam[103], J. Kvita[122], T. Kwan[104], N.G. Kyriacou[106], L.A.O. Laatu[102], C. Lacasta[163], F. Lacava[75a,75b], H. Lacker[18], D. Lacour[127], N.N. Lad[96], E. Ladygin[38], B. Laforge[127], T. Lagouri[137e], F.Z. Lahbabi[35a], S. Lai[55], I.K. Lakomiec[86a], N. Lalloue[60], J.E. Lambert[165], S. Lammers[68], W. Lampl[7], C. Lampoudis[152,e], A.N. Lancaster[115], E. Lançon[29], U. Landgraf[54], M.P.J. Landon[94], V.S. Lang[54], R.J. Langenberg[103], O.K.B. Langrekken[125], A.J. Lankford[159], F. Lanni[36], K. Lantzsch[24], A. Lanza[73a], A. Lapertosa[57b,57a], J.F. Laporte[135], T. Lari[71a], F. Lasagni Manghi[23b], M. Lassnig[36], V. Latonova[131], A. Laudrain[100], A. Laurier[150], S.D. Lawlor[139], Z. Lawrence[101], R. Lazaridou[167], M. Lazzaroni[71a,71b], B. Le[101], E.M. Le Boulicaut[51], B. Leban[93], A. Lebedev[81], M. LeBlanc[101], F. Ledroit-Guillon[60], A.C.A. Lee[96], S.C. Lee[148], S. Lee[47a,47b], T.F. Lee[92], L.L. Leeuw[33c], H.P. Lefebvre[95], M. Lefebvre[165], C. Leggett[17a], G. Lehmann Miotto[36], M. Leigh[56], W.A. Leight[103], W. Leinonen[113], A. Leisos[152,s], M.A.L. Leite[83c], C.E. Leitgeb[18], R. Leitner[133], K.J.C. Leney[44], T. Lenz[24], S. Leone[74a], C. Leonidopoulos[52], A. Leopold[144], C. Leroy[108], R. Les[107], C.G. Lester[32], M. Levchenko[37], J. Levêque[4], D. Levin[106], L.J. Levinson[169], M.P. Lewicki[87], D.J. Lewis[4], A. Li[5], B. Li[62b], C. Li[62a], C-Q. Li[110], H. Li[62a], H. Li[62b], H. Li[14c], H. Li[14b], H. Li[62b], J. Li[62c], K. Li[138], L. Li[62c], M. Li[14a,14e], Q.Y. Li[62a], S. Li[14a,14e], S. Li[62d,62c,d], T. Li[5], X. Li[104], Z. Li[126], Z. Li[104], Z. Li[14a,14e], S. Liang[14a,14e], Z. Liang[14a], M. Liberatore[135], B. Liberti[76a], K. Lie[64c], J. Lieber Marin[83b], H. Lien[68], K. Lin[107], R.E. Lindley[7], J.H. Lindon[2], E. Lipeles[128], A. Lipniacka[16], A. Lister[164], J.D. Little[4], B. Liu[14a], B.X. Liu[142], D. Liu[62d,62c], J.B. Liu[62a], J.K.K. Liu[32], K. Liu[62d,62c],

M. Liu [62a], M.Y. Liu [62a], P. Liu [14a], Q. Liu [62d,138,62c], X. Liu [62a], X. Liu [62b], Y. Liu [14d,14e], Y.L. Liu [62b], Y.W. Liu [62a], J. Llorente Merino [142], S.L. Lloyd [94], E.M. Lobodzinska [48], P. Loch [7], T. Lohse [18], K. Lohwasser [139], E. Loiacono [48], M. Lokajicek [131,*], J.D. Lomas [20], J.D. Long [162], I. Longarini [159], L. Longo [70a,70b], R. Longo [162], I. Lopez Paz [67], A. Lopez Solis [48], N. Lorenzo Martinez [4], A.M. Lory [109], G. Löschcke Centeno [146], O. Loseva [37], X. Lou [47a,47b], X. Lou [14a,14e], A. Lounis [66], J. Love [6], P.A. Love [91], G. Lu [14a,14e], M. Lu [80], S. Lu [128], Y.J. Lu [65], H.J. Lubatti [138], C. Luci [75a,75b], F.L. Lucio Alves [14c], A. Lucotte [60], F. Luehring [68], I. Luise [145], O. Lukianchuk [66], O. Lundberg [144], B. Lund-Jensen [144], N.A. Luongo [6], M.S. Lutz [151], A.B. Lux [25], D. Lynn [29], H. Lyons[92], R. Lysak [131], E. Lytken [98], V. Lyubushkin [38], T. Lyubushkina [38], M.M. Lyukova [145], H. Ma [29], K. Ma[62a], L.L. Ma [62b], W. Ma [62a], Y. Ma [121], D.M. Mac Donell [165], G. Maccarrone [53], J.C. MacDonald [100], P.C. Machado De Abreu Farias [83b], R. Madar [40], W.F. Mader [50], T. Madula [96], J. Maeda [85], T. Maeno [29], H. Maguire [139], V. Maiboroda [135], A. Maio [130a,130b,130d], K. Maj [86a], O. Majersky [48], S. Majewski [123], N. Makovec [66], V. Maksimovic [15], B. Malaescu [127], Pa. Malecki [87], V.P. Maleev [37], F. Malek [60,o], M. Mali [93], D. Malito [95], U. Mallik [80], S. Maltezos[10], S. Malyukov[38], J. Mamuzic [13], G. Mancini [53], G. Manco [73a,73b], J.P. Mandalia [94], I. Mandić [93], L. Manhaes de Andrade Filho [83a], I.M. Maniatis [169], J. Manjarres Ramos [102,ab], D.C. Mankad [169], A. Mann [109], B. Mansoulie [135], S. Manzoni [36], L. Mao [62c], X. Mapekula [33c], A. Marantis [152,s], G. Marchiori [5], M. Marcisovsky [131], C. Marcon [71a], M. Marinescu [20], S. Marium [48], M. Marjanovic [120], E.J. Marshall [91], Z. Marshall [17a], S. Marti-Garcia [163], T.A. Martin [167], V.J. Martin [52], B. Martin dit Latour [16], L. Martinelli [75a,75b], M. Martinez [13,t], P. Martinez Agullo [163], V.I. Martinez Outschoorn [103], P. Martinez Suarez [13], S. Martin-Haugh [134], V.S. Martoiu [27b], A.C. Martyniuk [96], A. Marzin [36], D. Mascione [78a,78b], L. Masetti [100], T. Mashimo [153], J. Masik [101], A.L. Maslennikov [37], P. Massarotti [72a,72b], P. Mastrandrea [74a,74b], A. Mastroberardino [43b,43a], T. Masubuchi [153], T. Mathisen [161], J. Matousek [133], N. Matsuzawa[153], J. Maurer [27b], B. Maček [93], D.A. Maximov [37], R. Mazini [148], I. Maznas [152], M. Mazza [107], S.M. Mazza [136], E. Mazzeo [71a,71b], C. Mc Ginn [29], J.P. Mc Gowan [104], S.P. Mc Kee [106], C.C. McCracken [164], E.F. McDonald [105], A.E. McDougall [114], J.A. Mcfayden [146], R.P. McGovern [128], G. Mchedlidze [149b], R.P. Mckenzie [33g], T.C. Mclachlan [48], D.J. Mclaughlin [96], S.J. McMahon [134], C.M. Mcpartland [92], R.A. McPherson [165,x], S. Mehlhase [109], A. Mehta [92], D. Melini [163], B.R. Mellado Garcia [33g], A.H. Melo [55], F. Meloni [48], A.M. Mendes Jacques Da Costa [101], H.Y. Meng [155], L. Meng [91], S. Menke [110], M. Mentink [36], E. Meoni [43b,43a], G. Mercado [115], C. Merlassino [69a,69c], L. Merola [72a,72b], C. Meroni [71a,71b], J. Metcalfe [6], A.S. Mete [6], C. Meyer [68], J-P. Meyer [135], R.P. Middleton [134], L. Mijović [52], G. Mikenberg [169], M. Mikestikova [131], M. Mikuž [93], H. Mildner [100], A. Milic [36], C.D. Milke [44], D.W. Miller [39], E.H. Miller [143], L.S. Miller [34], A. Milov [169], D.A. Milstead[47a,47b], T. Min[14c], A.A. Minaenko [37], I.A. Minashvili [149b], L. Mince [59], A.I. Mincer [117], B. Mindur [86a], M. Mineev [38], Y. Mino [88], L.M. Mir [13], M. Miralles Lopez [163], M. Mironova [17a], A. Mishima[153], M.C. Missio [113], A. Mitra [167], V.A. Mitsou [163], Y. Mitsumori [111], O. Miu [155], P.S. Miyagawa [94], T. Mkrtchyan [63a], M. Mlinarevic [96], T. Mlinarevic [96], M. Mlynarikova [36], S. Mobius [19], P. Moder [48], P. Mogg [109], M.H. Mohamed Farook [112], A.F. Mohammed [14a,14e], S. Mohapatra [41], G. Mokgatitswane [33g], L. Moleri [169], B. Mondal [141], S. Mondal [132], K. Mönig [48], E. Monnier [102], L. Monsonis Romero[163], J. Montejo Berlingen [13], M. Montella [119], F. Montereali [77a,77b], F. Monticelli [90], S. Monzani [69a,69c], N. Morange [66], A.L. Moreira De Carvalho [130a], M. Moreno Llácer [163], C. Moreno Martinez [56], P. Morettini [57b], S. Morgenstern [36], M. Morii [61], M. Morinaga [153], A.K. Morley [36], F. Morodei [75a,75b], L. Morvaj [36], P. Moschovakos [36], B. Moser [36], M. Mosidze[149b], T. Moskalets [54],

P. Moskvitina [113], J. Moss [31,l], E.J.W. Moyse [103], O. Mtintsilana [33g], S. Muanza [102], J. Mueller [129], D. Muenstermann [91], R. Müller [19], G.A. Mullier [161], A.J. Mullin[32], J.J. Mullin[128], D.P. Mungo [155], D. Munoz Perez [163], F.J. Munoz Sanchez [101], M. Murin [101], W.J. Murray [167,134], A. Murrone [71a,71b], M. Muškinja [17a], C. Mwewa [29], A.G. Myagkov [37,a], A.J. Myers [8], G. Myers [68], M. Myska [132], B.P. Nachman [17a], O. Nackenhorst [49], A. Nag [50], K. Nagai [126], K. Nagano [84], J.L. Nagle [29,aj], E. Nagy [102], A.M. Nairz [36], Y. Nakahama [84], K. Nakamura [84], K. Nakkalil [5], H. Nanjo [124], R. Narayan [44], E.A. Narayanan [112], I. Naryshkin [37], M. Naseri [34], S. Nasri [116b], C. Nass [24], G. Navarro [22a], J. Navarro-Gonzalez [163], R. Nayak [151], A. Nayaz [18], P.Y. Nechaeva [37], F. Nechansky [48], L. Nedic [126], T.J. Neep [20], A. Negri [73a,73b], M. Negrini [23b], C. Nellist [114], C. Nelson [104], K. Nelson [106], S. Nemecek [131], M. Nessi [36,h], M.S. Neubauer [162], F. Neuhaus [100], J. Neundorf [48], R. Newhouse [164], P.R. Newman [20], C.W. Ng [129], Y.W.Y. Ng [48], B. Ngair [116a], H.D.N. Nguyen [108], R.B. Nickerson [126], R. Nicolaidou [135], J. Nielsen [136], M. Niemeyer [55], J. Niermann [55,36], N. Nikiforou [36], V. Nikolaenko [37,a], I. Nikolic-Audit [127], K. Nikolopoulos [20], P. Nilsson [29], I. Ninca [48], H.R. Nindhito [56], G. Ninio [151], A. Nisati [75a], N. Nishu [2], R. Nisius [110], J-E. Nitschke [50], E.K. Nkadimeng [33g], T. Nobe [153], D.L. Noel [32], T. Nommensen [147], M.B. Norfolk [139], R.R.B. Norisam [96], B.J. Norman [34], M. Noury [35a], J. Novak [93], T. Novak [48], L. Novotny [132], R. Novotny [112], L. Nozka [122], K. Ntekas [159], N.M.J. Nunes De Moura Junior [83b], E. Nurse[96], J. Ocariz [127], A. Ochi [85], I. Ochoa [130a], S. Oerdek [48], J.T. Offermann [39], A. Ogrodnik [133], A. Oh [101], C.C. Ohm [144], H. Oide [84], R. Oishi [153], M.L. Ojeda [48], Y. Okumura [153], L.F. Oleiro Seabra [130a], S.A. Olivares Pino [137d], D. Oliveira Damazio [29], D. Oliveira Goncalves [83a], J.L. Oliver [159], Ö.O. Öncel [54], A.P. O'Neill [19], A. Onofre [130a,130e], P.U.E. Onyisi [11], M.J. Oreglia [39], G.E. Orellana [90], D. Orestano [77a,77b], N. Orlando [13], R.S. Orr [155], V. O'Shea [59], L.M. Osojnak [128], R. Ospanov [62a], G. Otero y Garzon [30], H. Otono [89], P.S. Ott [63a], G.J. Ottino [17a], M. Ouchrif [35d], J. Ouellette [29], F. Ould-Saada [125], M. Owen [59], R.E. Owen [134], K.Y. Oyulmaz [21a], V.E. Ozcan [21a], F. Ozturk [87], N. Ozturk [8], S. Ozturk [82], H.A. Pacey [126], A. Pacheco Pages [13], C. Padilla Aranda [13], G. Padovano [75a,75b], S. Pagan Griso [17a], G. Palacino [68], A. Palazzo [70a,70b], J. Pan [172], T. Pan [64a], D.K. Panchal [11], C.E. Pandini [114], J.G. Panduro Vazquez [95], H.D. Pandya [1], H. Pang [14b], P. Pani [48], G. Panizzo [69a,69c], L. Paolozzi [56], C. Papadatos [108], S. Parajuli [162], A. Paramonov [6], C. Paraskevopoulos [10], D. Paredes Hernandez [64b], K.R. Park [41], T.H. Park [155], M.A. Parker [32], F. Parodi [57b,57a], E.W. Parrish [115], V.A. Parrish [52], J.A. Parsons [41], U. Parzefall [54], B. Pascual Dias [108], L. Pascual Dominguez [151], E. Pasqualucci [75a], S. Passaggio [57b], F. Pastore [95], P. Pasuwan [47a,47b], P. Patel [87], U.M. Patel [51], J.R. Pater [101], T. Pauly [36], J. Pearkes [143], M. Pedersen [125], R. Pedro [130a], S.V. Peleganchuk [37], O. Penc [36], E.A. Pender [52], K.E. Penski [109], M. Penzin [37], B.S. Peralva [83d], A.P. Pereira Peixoto [60], L. Pereira Sanchez [47a,47b], D.V. Perepelitsa [29,aj], E. Perez Codina [156a], M. Perganti [10], L. Perini [71a,71b,*], H. Pernegger [36], O. Perrin [40], K. Peters [48], R.F.Y. Peters [101], B.A. Petersen [36], T.C. Petersen [42], E. Petit [102], V. Petousis [132], C. Petridou [152,e], A. Petrukhin [141], M. Pettee [17a], N.E. Pettersson [36], A. Petukhov [37], K. Petukhova [133], R. Pezoa [137f], L. Pezzotti [36], G. Pezzullo [172], T.M. Pham [170], T. Pham [105], P.W. Phillips [134], G. Piacquadio [145], E. Pianori [17a], F. Piazza [123], R. Piegaia [30], D. Pietreanu [27b], A.D. Pilkington [101], M. Pinamonti [69a,69c], J.L. Pinfold [2], B.C. Pinheiro Pereira [130a], A.E. Pinto Pinoargote [100,135], L. Pintucci [69a,69c], K.M. Piper [146], A. Pirttikoski [56], D.A. Pizzi [34], L. Pizzimento [64b], A. Pizzini [114], M.-A. Pleier [29], V. Plesanovs[54], V. Pleskot [133], E. Plotnikova[38], G. Poddar [4], R. Poettgen [98], L. Poggioli [127], I. Pokharel [55], S. Polacek [133], G. Polesello [73a], A. Poley [142,156a], R. Polifka [132], A. Polini [23b], C.S. Pollard [167], Z.B. Pollock [119], V. Polychronakos [29], E. Pompa Pacchi [75a,75b], D. Ponomarenko [113], L. Pontecorvo [36], S. Popa [27a], G.A. Popeneciu [27d], A. Poreba [36], D.M. Portillo Quintero [156a],

S. Pospisil[132], M.A. Postill[139], P. Postolache[27c], K. Potamianos[167], P.A. Potepa[86a], I.N. Potrap[38], C.J. Potter[32], H. Potti[1], T. Poulsen[48], J. Poveda[163], M.E. Pozo Astigarraga[36], A. Prades Ibanez[163], J. Pretel[54], D. Price[101], M. Primavera[70a], M.A. Principe Martin[99], R. Privara[122], T. Procter[59], M.L. Proffitt[138], N. Proklova[128], K. Prokofiev[64c], G. Proto[110], S. Protopopescu[29], J. Proudfoot[6], M. Przybycien[86a], W.W. Przygoda[86b], A. Psallidas[46], J.E. Puddefoot[139], D. Pudzha[37], D. Pyatiizbyantseva[37], J. Qian[106], D. Qichen[101], Y. Qin[101], T. Qiu[52], A. Quadt[55], M. Queitsch-Maitland[101], G. Quetant[56], R.P. Quinn[164], G. Rabanal Bolanos[61], D. Rafanoharana[54], F. Ragusa[71a,71b], J.L. Rainbolt[39], J.A. Raine[56], S. Rajagopalan[29], E. Ramakoti[37], I.A. Ramirez-Berend[34], K. Ran[48,14e], N.P. Rapheeha[33g], H. Rasheed[27b], V. Raskina[127], D.F. Rassloff[63a], A. Rastogi[17a], S. Rave[100], B. Ravina[55], I. Ravinovich[169], M. Raymond[36], A.L. Read[125], N.P. Readioff[139], D.M. Rebuzzi[73a,73b], G. Redlinger[29], A.S. Reed[110], K. Reeves[26], J.A. Reidelsturz[171], D. Reikher[151], A. Rej[49], C. Rembser[36], A. Renardi[48], M. Renda[27b], M.B. Rendel[110], F. Renner[48], A.G. Rennie[159], A.L. Rescia[48], S. Resconi[71a], M. Ressegotti[57b,57a], S. Rettie[36], J.G. Reyes Rivera[107], E. Reynolds[17a], O.L. Rezanova[37], P. Reznicek[133], N. Ribaric[91], E. Ricci[78a,78b], R. Richter[110], S. Richter[47a,47b], E. Richter-Was[86b], M. Ridel[127], S. Ridouani[35d], P. Rieck[117], P. Riedler[36], E.M. Riefel[47a,47b], J.O. Rieger[114], M. Rijssenbeek[145], A. Rimoldi[73a,73b], M. Rimoldi[36], L. Rinaldi[23b,23a], T.T. Rinn[29], M.P. Rinnagel[109], G. Ripellino[161], I. Riu[13], P. Rivadeneira[48], J.C. Rivera Vergara[165], F. Rizatdinova[121], E. Rizvi[94], B.A. Roberts[167], B.R. Roberts[17a], S.H. Robertson[104,x], D. Robinson[32], C.M. Robles Gajardo[137f], M. Robles Manzano[100], A. Robson[59], A. Rocchi[76a,76b], C. Roda[74a,74b], S. Rodriguez Bosca[63a], Y. Rodriguez Garcia[22a], A. Rodriguez Rodriguez[54], A.M. Rodríguez Vera[156b], S. Roe[36], J.T. Roemer[159], A.R. Roepe-Gier[136], J. Roggel[171], O. Røhne[125], R.A. Rojas[103], C.P.A. Roland[127], J. Roloff[29], A. Romaniouk[37], E. Romano[73a,73b], M. Romano[23b], A.C. Romero Hernandez[162], N. Rompotis[92], L. Roos[127], S. Rosati[75a], B.J. Rosser[39], E. Rossi[126], E. Rossi[72a,72b], L.P. Rossi[57b], L. Rossini[54], R. Rosten[119], M. Rotaru[27b], B. Rottler[54], C. Rougier[102,ab], D. Rousseau[66], D. Rousso[32], A. Roy[162], S. Roy-Garand[155], A. Rozanov[102], Z.M.A. Rozario[59], Y. Rozen[150], X. Ruan[33g], A. Rubio Jimenez[163], A.J. Ruby[92], V.H. Ruelas Rivera[18], T.A. Ruggeri[1], A. Ruggiero[126], A. Ruiz-Martinez[163], A. Rummler[36], Z. Rurikova[54], N.A. Rusakovich[38], H.L. Russell[165], G. Russo[75a,75b], J.P. Rutherfoord[7], S. Rutherford Colmenares[32], K. Rybacki[91], M. Rybar[133], E.B. Rye[125], A. Ryzhov[44], J.A. Sabater Iglesias[56], P. Sabatini[163], H.F-W. Sadrozinski[136], F. Safai Tehrani[75a], B. Safarzadeh Samani[134], M. Safdari[143], S. Saha[165], M. Sahinsoy[110], A. Saibel[163], M. Saimpert[135], M. Saito[153], T. Saito[153], D. Salamani[36], A. Salnikov[143], J. Salt[163], A. Salvador Salas[151], D. Salvatore[43b,43a], F. Salvatore[146], A. Salzburger[36], D. Sammel[54], D. Sampsonidis[152,e], D. Sampsonidou[123], J. Sánchez[163], A. Sanchez Pineda[4], V. Sanchez Sebastian[163], H. Sandaker[125], C.O. Sander[48], J.A. Sandesara[103], M. Sandhoff[171], C. Sandoval[22b], D.P.C. Sankey[134], T. Sano[88], A. Sansoni[53], L. Santi[75a,75b], C. Santoni[40], H. Santos[130a,130b], A. Santra[169], K.A. Saoucha[160], J.G. Saraiva[130a,130d], J. Sardain[7], O. Sasaki[84], K. Sato[157], C. Sauer[63b], F. Sauerburger[54], E. Sauvan[4], P. Savard[155,ag], R. Sawada[153], C. Sawyer[134], L. Sawyer[97], I. Sayago Galvan[163], C. Sbarra[23b], A. Sbrizzi[23b,23a], T. Scanlon[96], J. Schaarschmidt[138], U. Schäfer[100], A.C. Schaffer[66,44], D. Schaile[109], R.D. Schamberger[145], C. Scharf[18], M.M. Schefer[19], V.A. Schegelsky[37], D. Scheirich[133], F. Schenck[18], M. Schernau[159], C. Scheulen[55], C. Schiavi[57b,57a], E.J. Schioppa[70a,70b], M. Schioppa[43b,43a], B. Schlag[143,n], K.E. Schleicher[54], S. Schlenker[36], J. Schmeing[171], M.A. Schmidt[171], K. Schmieden[100], C. Schmitt[100], N. Schmitt[100], S. Schmitt[48], L. Schoeffel[135], A. Schoening[63b], P.G. Scholer[54], E. Schopf[126], M. Schott[100],

J. Schovancova [36], S. Schramm [56], F. Schroeder [171], T. Schroer [56], H-C. Schultz-Coulon [63a], M. Schumacher [54], B.A. Schumm [136], Ph. Schune [135], A.J. Schuy [138], H.R. Schwartz [136], A. Schwartzman [143], T.A. Schwarz [106], Ph. Schwemling [135], R. Schwienhorst [107], A. Sciandra [136], G. Sciolla [26], F. Scuri [74a], C.D. Sebastiani [92], K. Sedlaczek [115], P. Seema [18], S.C. Seidel [112], A. Seiden [136], B.D. Seidlitz [41], C. Seitz [48], J.M. Seixas [83b], G. Sekhniaidze [72a], L. Selem [60], N. Semprini-Cesari [23b,23a], D. Sengupta [56], V. Senthilkumar [163], L. Serin [66], L. Serkin [69a,69b], M. Sessa [76a,76b], H. Severini [120], F. Sforza [57b,57a], A. Sfyrla [56], E. Shabalina [55], R. Shaheen [144], J.D. Shahinian [128], D. Shaked Renous [169], L.Y. Shan [14a], M. Shapiro [17a], A. Sharma [36], A.S. Sharma [164], P. Sharma [80], S. Sharma [48], P.B. Shatalov [37], K. Shaw [146], S.M. Shaw [101], A. Shcherbakova [37], Q. Shen [62c,5], D.J. Sheppard [142], P. Sherwood [96], L. Shi [96], X. Shi [14a], C.O. Shimmin [172], J.D. Shinner [95], I.P.J. Shipsey [126], S. Shirabe [56,h], M. Shiyakova [38,v], J. Shlomi [169], M.J. Shochet [39], J. Shojaii [105], D.R. Shope [125], B. Shrestha [120], S. Shrestha [119,ak], E.M. Shrif [33g], M.J. Shroff [165], P. Sicho [131], A.M. Sickles [162], E. Sideras Haddad [33g], A. Sidoti [23b], F. Siegert [50], Dj. Sijacki [15], F. Sili [90], J.M. Silva [20], M.V. Silva Oliveira [29], S.B. Silverstein [47a], S. Simion [66], R. Simoniello [36], E.L. Simpson [59], H. Simpson [146], L.R. Simpson [106], N.D. Simpson [98], S. Simsek [82], S. Sindhu [55], P. Sinervo [155], S. Singh [155], S. Sinha [48], S. Sinha [101], M. Sioli [23b,23a], I. Siral [36], E. Sitnikova [48], S.Yu. Sivoklokov [37,*], J. Sjölin [47a,47b], A. Skaf [55], E. Skorda [20], P. Skubic [120], M. Slawinska [87], V. Smakhtin [169], B.H. Smart [134], S.Yu. Smirnov [37], Y. Smirnov [37], L.N. Smirnova [37,a], O. Smirnova [98], A.C. Smith [41], E.A. Smith [39], H.A. Smith [126], J.L. Smith [92], R. Smith [143], M. Smizanska [91], K. Smolek [132], A.A. Snesarev [37], S.R. Snider [155], H.L. Snoek [114], S. Snyder [29], R. Sobie [165,x], A. Soffer [151], C.A. Solans Sanchez [36], E.Yu. Soldatov [37], U. Soldevila [163], A.A. Solodkov [37], S. Solomon [26], A. Soloshenko [38], K. Solovieva [54], O.V. Solovyanov [40], V. Solovyev [37], P. Sommer [36], A. Sonay [13], W.Y. Song [156b], J.M. Sonneveld [114], A. Sopczak [132], A.L. Sopio [96], F. Sopkova [28b], J.D. Sorenson [112], I.R. Sotarriva Alvarez [154], V. Sothilingam [63a], O.J. Soto Sandoval [137c,137b], S. Sottocornola [68], R. Soualah [160], Z. Soumaimi [35e], D. South [48], N. Soybelman [169], S. Spagnolo [70a,70b], M. Spalla [110], D. Sperlich [54], G. Spigo [36], S. Spinali [91], D.P. Spiteri [59], M. Spousta [133], E.J. Staats [34], A. Stabile [71a,71b], R. Stamen [63a], A. Stampekis [20], M. Standke [24], E. Stanecka [87], M.V. Stange [50], B. Stanislaus [17a], M.M. Stanitzki [48], B. Stapf [48], E.A. Starchenko [37], G.H. Stark [136], J. Stark [102,ab], P. Staroba [131], P. Starovoitov [63a], S. Stärz [104], R. Staszewski [87], G. Stavropoulos [46], J. Steentoft [161], P. Steinberg [29], B. Stelzer [142,156a], H.J. Stelzer [129], O. Stelzer-Chilton [156a], H. Stenzel [58], T.J. Stevenson [146], G.A. Stewart [36], J.R. Stewart [121], M.C. Stockton [36], G. Stoicea [27b], M. Stolarski [130a], S. Stonjek [110], A. Straessner [50], J. Strandberg [144], S. Strandberg [47a,47b], M. Stratmann [171], M. Strauss [120], T. Strebler [102], P. Strizenec [28b], R. Ströhmer [166], D.M. Strom [123], R. Stroynowski [44], A. Strubig [47a,47b], S.A. Stucci [29], B. Stugu [16], J. Stupak [120], N.A. Styles [48], D. Su [143], S. Su [62a], W. Su [62d], X. Su [62a,66], K. Sugizaki [153], V.V. Sulin [37], M.J. Sullivan [92], D.M.S. Sultan [78a,78b], L. Sultanaliyeva [37], S. Sultansoy [3b], T. Sumida [88], S. Sun [106], S. Sun [170], O. Sunneborn Gudnadottir [161], N. Sur [102], M.R. Sutton [146], H. Suzuki [157], M. Svatos [131], M. Swiatlowski [156a], T. Swirski [166], I. Sykora [28a], M. Sykora [133], T. Sykora [133], D. Ta [100], K. Tackmann [48,u], A. Taffard [159], R. Tafirout [156a], J.S. Tafoya Vargas [66], E.P. Takeva [52], Y. Takubo [84], M. Talby [102], A.A. Talyshev [37], K.C. Tam [64b], N.M. Tamir [151], A. Tanaka [153], J. Tanaka [153], R. Tanaka [66], M. Tanasini [57b,57a], Z. Tao [164], S. Tapia Araya [137f], S. Tapprogge [100], A. Tarek Abouelfadl Mohamed [107], S. Tarem [150], K. Tariq [14a], G. Tarna [102,27b], G.F. Tartarelli [71a], P. Tas [133], M. Tasevsky [131], E. Tassi [43b,43a], A.C. Tate [162], G. Tateno [153], Y. Tayalati [35e,w], G.N. Taylor [105], W. Taylor [156b], A.S. Tee [170], R. Teixeira De Lima [143], P. Teixeira-Dias [95], J.J. Teoh [155], K. Terashi [153], J. Terron [99], S. Terzo [13], M. Testa [53],

R.J. Teuscher[155,x], A. Thaler[79], O. Theiner[56], N. Themistokleous[52], T. Theveneaux-Pelzer[102], O. Thielmann[171], D.W. Thomas[95], J.P. Thomas[20], E.A. Thompson[17a], P.D. Thompson[20], E. Thomson[128], Y. Tian[55], V. Tikhomirov[37,a], Yu.A. Tikhonov[37], S. Timoshenko[37], D. Timoshyn[133], E.X.L. Ting[1], P. Tipton[172], S.H. Tlou[33g], A. Tnourji[40], K. Todome[154], S. Todorova-Nova[133], S. Todt[50], M. Togawa[84], J. Tojo[89], S. Tokár[28a], K. Tokushuku[84], O. Toldaiev[68], R. Tombs[32], M. Tomoto[84,111], L. Tompkins[143,n], K.W. Topolnicki[86b], E. Torrence[123], H. Torres[102,ab], E. Torró Pastor[163], M. Toscani[30], C. Tosciri[39], M. Tost[11], D.R. Tovey[139], A. Traeet[16], I.S. Trandafir[27b], T. Trefzger[166], A. Tricoli[29], I.M. Trigger[156a], S. Trincaz-Duvoid[127], D.A. Trischuk[26], B. Trocmé[60], C. Troncon[71a], L. Truong[33c], M. Trzebinski[87], A. Trzupek[87], F. Tsai[145], M. Tsai[106], A. Tsiamis[152,e], P.V. Tsiareshka[37], S. Tsigaridas[156a], A. Tsirigotis[152,s], V. Tsiskaridze[155], E.G. Tskhadadze[149a], M. Tsopoulou[152,e], Y. Tsujikawa[88], I.I. Tsukerman[37], V. Tsulaia[17a], S. Tsuno[84], K. Tsuri[118], D. Tsybychev[145], Y. Tu[64b], A. Tudorache[27b], V. Tudorache[27b], A.N. Tuna[61], S. Turchikhin[57b,57a], I. Turk Cakir[3a], R. Turra[71a], T. Turtuvshin[38,y], P.M. Tuts[41], S. Tzamarias[152,e], P. Tzanis[10], E. Tzovara[100], F. Ukegawa[157], P.A. Ulloa Poblete[137c,137b], E.N. Umaka[29], G. Unal[36], M. Unal[11], A. Undrus[29], G. Unel[159], J. Urban[28b], P. Urquijo[105], P. Urrejola[137a], G. Usai[8], R. Ushioda[154], M. Usman[108], Z. Uysal[82], V. Vacek[132], B. Vachon[104], K.O.H. Vadla[125], T. Vafeiadis[36], A. Vaitkus[96], C. Valderanis[109], E. Valdes Santurio[47a,47b], M. Valente[156a], S. Valentinetti[23b,23a], A. Valero[163], E. Valiente Moreno[163], A. Vallier[102,ab], J.A. Valls Ferrer[163], D.R. Van Arneman[114], T.R. Van Daalen[138], A. Van Der Graaf[49], P. Van Gemmeren[6], M. Van Rijnbach[125,36], S. Van Stroud[96], I. Van Vulpen[114], M. Vanadia[76a,76b], W. Vandelli[36], M. Vandenbroucke[135], E.R. Vandewall[121], D. Vannicola[151], L. Vannoli[57b,57a], R. Vari[75a], E.W. Varnes[7], C. Varni[17b], T. Varol[148], D. Varouchas[66], L. Varriale[163], K.E. Varvell[147], M.E. Vasile[27b], L. Vaslin[84], G.A. Vasquez[165], A. Vasyukov[38], F. Vazeille[40], T. Vazquez Schroeder[36], J. Veatch[31], V. Vecchio[101], M.J. Veen[103], I. Veliscek[126], L.M. Veloce[155], F. Veloso[130a,130c], S. Veneziano[75a], A. Ventura[70a,70b], S. Ventura Gonzalez[135], A. Verbytskyi[110], M. Verducci[74a,74b], C. Vergis[24], M. Verissimo De Araujo[83b], W. Verkerke[114], J.C. Vermeulen[114], C. Vernieri[143], M. Vessella[103], M.C. Vetterli[142,ag], A. Vgenopoulos[152,e], N. Viaux Maira[137f], T. Vickey[139], O.E. Vickey Boeriu[139], G.H.A. Viehhauser[126], L. Vigani[63b], M. Villa[23b,23a], M. Villaplana Perez[163], E.M. Villhauer[52], E. Vilucchi[53], M.G. Vincter[34], G.S. Virdee[20], A. Vishwakarma[52], A. Visibile[114], C. Vittori[36], I. Vivarelli[146], E. Voevodina[110], F. Vogel[109], J.C. Voigt[50], P. Vokac[132], Yu. Volkotrub[86a], J. Von Ahnen[48], E. Von Toerne[24], B. Vormwald[36], V. Vorobel[133], K. Vorobev[37], M. Vos[163], K. Voss[141], J.H. Vossebeld[92], M. Vozak[114], L. Vozdecky[94], N. Vranjes[15], M. Vranjes Milosavljevic[15], M. Vreeswijk[114], N.K. Vu[62d,62c], R. Vuillermet[36], O. Vujinovic[100], I. Vukotic[39], S. Wada[157], C. Wagner[103], J.M. Wagner[17a], W. Wagner[171], S. Wahdan[171], H. Wahlberg[90], M. Wakida[111], J. Walder[134], R. Walker[109], W. Walkowiak[141], A. Wall[128], T. Wamorkar[6], A.Z. Wang[136], C. Wang[100], C. Wang[62c], H. Wang[17a], J. Wang[64a], R.-J. Wang[100], R. Wang[61], R. Wang[6], S.M. Wang[148], S. Wang[62b], T. Wang[62a], W.T. Wang[80], W. Wang[14a], X. Wang[14c], X. Wang[162], X. Wang[62c], Y. Wang[62d], Y. Wang[14c], Z. Wang[106], Z. Wang[62d,51,62c], Z. Wang[106], A. Warburton[104], R.J. Ward[20], N. Warrack[59], A.T. Watson[20], H. Watson[59], M.F. Watson[20], E. Watton[59,134], G. Watts[138], B.M. Waugh[96], C. Weber[29], H.A. Weber[18], M.S. Weber[19], S.M. Weber[63a], C. Wei[62a], Y. Wei[126], A.R. Weidberg[126], E.J. Weik[117], J. Weingarten[49], M. Weirich[100], C. Weiser[54], C.J. Wells[48], T. Wenaus[29], B. Wendland[49], T. Wengler[36], N.S. Wenke[110], N. Wermes[24], M. Wessels[63a], A.M. Wharton[91], A.S. White[61], A. White[8], M.J. White[1], D. Whiteson[159], L. Wickremasinghe[124],

W. Wiedenmann[170], M. Wielers[134], C. Wiglesworth[42], D.J. Wilbern[120], H.G. Wilkens[36], D.M. Williams[41], H.H. Williams[128], S. Williams[32], S. Willocq[103], B.J. Wilson[101], P.J. Windischhofer[39], F.I. Winkel[30], F. Winklmeier[123], B.T. Winter[54], J.K. Winter[101], M. Wittgen[143], M. Wobisch[97], Z. Wolffs[114], J. Wollrath[159], M.W. Wolter[87], H. Wolters[130a,130c], A.F. Wongel[48], E.L. Woodward[41], S.D. Worm[48], B.K. Wosiek[87], K.W. Woźniak[87], S. Wozniewski[55], K. Wraight[59], C. Wu[20], J. Wu[14a,14e], M. Wu[64a], M. Wu[113], S.L. Wu[170], X. Wu[56], Y. Wu[62a], Z. Wu[135], J. Wuerzinger[110,ae], T.R. Wyatt[101], B.M. Wynne[52], S. Xella[42], L. Xia[14c], M. Xia[14b], J. Xiang[64c], M. Xie[62a], X. Xie[62a], S. Xin[14a,14e], A. Xiong[123], J. Xiong[17a], D. Xu[14a], H. Xu[62a], L. Xu[62a], R. Xu[128], T. Xu[106], Y. Xu[14b], Z. Xu[52], Z. Xu[14c], B. Yabsley[147], S. Yacoob[33a], Y. Yamaguchi[154], E. Yamashita[153], H. Yamauchi[157], T. Yamazaki[17a], Y. Yamazaki[85], J. Yan[62c], S. Yan[126], Z. Yan[25], H.J. Yang[62c,62d], H.T. Yang[62a], S. Yang[62a], T. Yang[64c], X. Yang[36], X. Yang[14a], Y. Yang[44], Y. Yang[62a], Z. Yang[62a], W-M. Yao[17a], Y.C. Yap[48], H. Ye[14c], H. Ye[55], J. Ye[14a], S. Ye[29], X. Ye[62a], Y. Yeh[96], I. Yeletskikh[38], B.K. Yeo[17b], M.R. Yexley[96], P. Yin[41], K. Yorita[168], S. Younas[27b], C.J.S. Young[36], C. Young[143], C. Yu[14a,14e,ai], Y. Yu[62a], M. Yuan[106], R. Yuan[62b], L. Yue[96], M. Zaazoua[62a], B. Zabinski[87], E. Zaid[52], Z.K. Zak[87], T. Zakareishvili[149b], N. Zakharchuk[34], S. Zambito[56], J.A. Zamora Saa[137d,137b], J. Zang[153], D. Zanzi[54], O. Zaplatilek[132], C. Zeitnitz[171], H. Zeng[14a], J.C. Zeng[162], D.T. Zenger Jr[26], O. Zenin[37], T. Ženiš[28a], S. Zenz[94], S. Zerradi[35a], D. Zerwas[66], M. Zhai[14a,14e], B. Zhang[14c], D.F. Zhang[139], J. Zhang[62b], J. Zhang[6], K. Zhang[14a,14e], L. Zhang[14c], P. Zhang[14a,14e], R. Zhang[170], S. Zhang[106], S. Zhang[44], T. Zhang[153], X. Zhang[62c], X. Zhang[62b], Y. Zhang[62c,5], Y. Zhang[96], Y. Zhang[14c], Z. Zhang[17a], Z. Zhang[66], H. Zhao[138], T. Zhao[62b], Y. Zhao[136], Z. Zhao[62a], A. Zhemchugov[38], J. Zheng[14c], K. Zheng[162], X. Zheng[62a], Z. Zheng[143], D. Zhong[162], B. Zhou[106], H. Zhou[7], N. Zhou[62c], Y. Zhou[14c], Y. Zhou[7], C.G. Zhu[62b], J. Zhu[106], Y. Zhu[62c], Y. Zhu[62a], X. Zhuang[14a], K. Zhukov[37], V. Zhulanov[37], N.I. Zimine[38], J. Zinsser[63b], M. Ziolkowski[141], L. Živković[15], A. Zoccoli[23b,23a], K. Zoch[61], T.G. Zorbas[139], O. Zormpa[46], W. Zou[41], L. Zwalinski[36].

[1]Department of Physics, University of Adelaide, Adelaide; Australia.
[2]Department of Physics, University of Alberta, Edmonton AB; Canada.
[3(a)]Department of Physics, Ankara University, Ankara;[(b)]Division of Physics, TOBB University of Economics and Technology, Ankara; Türkiye.
[4]LAPP, Université Savoie Mont Blanc, CNRS/IN2P3, Annecy; France.
[5]APC, Université Paris Cité, CNRS/IN2P3, Paris; France.
[6]High Energy Physics Division, Argonne National Laboratory, Argonne IL; United States of America.
[7]Department of Physics, University of Arizona, Tucson AZ; United States of America.
[8]Department of Physics, University of Texas at Arlington, Arlington TX; United States of America.
[9]Physics Department, National and Kapodistrian University of Athens, Athens; Greece.
[10]Physics Department, National Technical University of Athens, Zografou; Greece.
[11]Department of Physics, University of Texas at Austin, Austin TX; United States of America.
[12]Institute of Physics, Azerbaijan Academy of Sciences, Baku; Azerbaijan.
[13]Institut de Física d'Altes Energies (IFAE), Barcelona Institute of Science and Technology, Barcelona; Spain.
[14(a)]Institute of High Energy Physics, Chinese Academy of Sciences, Beijing;[(b)]Physics Department, Tsinghua University, Beijing;[(c)]Department of Physics, Nanjing University, Nanjing;[(d)]School of Science, Shenzhen Campus of Sun Yat-sen University;[(e)]University of Chinese Academy of Science (UCAS), Beijing; China.

[15]Institute of Physics, University of Belgrade, Belgrade; Serbia.
[16]Department for Physics and Technology, University of Bergen, Bergen; Norway.
[17(a)]Physics Division, Lawrence Berkeley National Laboratory, Berkeley CA;[(b)]University of California, Berkeley CA; United States of America.
[18]Institut für Physik, Humboldt Universität zu Berlin, Berlin; Germany.
[19]Albert Einstein Center for Fundamental Physics and Laboratory for High Energy Physics, University of Bern, Bern; Switzerland.
[20]School of Physics and Astronomy, University of Birmingham, Birmingham; United Kingdom.
[21(a)]Department of Physics, Bogazici University, Istanbul;[(b)]Department of Physics Engineering, Gaziantep University, Gaziantep;[(c)]Department of Physics, Istanbul University, Istanbul; Türkiye.
[22(a)]Facultad de Ciencias y Centro de Investigaciónes, Universidad Antonio Nariño, Bogotá;[(b)]Departamento de Física, Universidad Nacional de Colombia, Bogotá; Colombia.
[23(a)]Dipartimento di Fisica e Astronomia A. Righi, Università di Bologna, Bologna;[(b)]INFN Sezione di Bologna; Italy.
[24]Physikalisches Institut, Universität Bonn, Bonn; Germany.
[25]Department of Physics, Boston University, Boston MA; United States of America.
[26]Department of Physics, Brandeis University, Waltham MA; United States of America.
[27(a)]Transilvania University of Brasov, Brasov;[(b)]Horia Hulubei National Institute of Physics and Nuclear Engineering, Bucharest;[(c)]Department of Physics, Alexandru Ioan Cuza University of Iasi, Iasi;[(d)]National Institute for Research and Development of Isotopic and Molecular Technologies, Physics Department, Cluj-Napoca;[(e)]University Politehnica Bucharest, Bucharest;[(f)]West University in Timisoara, Timisoara;[(g)]Faculty of Physics, University of Bucharest, Bucharest; Romania.
[28(a)]Faculty of Mathematics, Physics and Informatics, Comenius University, Bratislava;[(b)]Department of Subnuclear Physics, Institute of Experimental Physics of the Slovak Academy of Sciences, Kosice; Slovak Republic.
[29]Physics Department, Brookhaven National Laboratory, Upton NY; United States of America.
[30]Universidad de Buenos Aires, Facultad de Ciencias Exactas y Naturales, Departamento de Física, y CONICET, Instituto de Física de Buenos Aires (IFIBA), Buenos Aires; Argentina.
[31]California State University, CA; United States of America.
[32]Cavendish Laboratory, University of Cambridge, Cambridge; United Kingdom.
[33(a)]Department of Physics, University of Cape Town, Cape Town;[(b)]iThemba Labs, Western Cape;[(c)]Department of Mechanical Engineering Science, University of Johannesburg, Johannesburg;[(d)]National Institute of Physics, University of the Philippines Diliman (Philippines);[(e)]University of South Africa, Department of Physics, Pretoria;[(f)]University of Zululand, KwaDlangezwa;[(g)]School of Physics, University of the Witwatersrand, Johannesburg; South Africa.
[34]Department of Physics, Carleton University, Ottawa ON; Canada.
[35(a)]Faculté des Sciences Ain Chock, Réseau Universitaire de Physique des Hautes Energies - Université Hassan II, Casablanca;[(b)]Faculté des Sciences, Université Ibn-Tofail, Kénitra;[(c)]Faculté des Sciences Semlalia, Université Cadi Ayyad, LPHEA-Marrakech;[(d)]LPMR, Faculté des Sciences, Université Mohamed Premier, Oujda;[(e)]Faculté des sciences, Université Mohammed V, Rabat;[(f)]Institute of Applied Physics, Mohammed VI Polytechnic University, Ben Guerir; Morocco.
[36]CERN, Geneva; Switzerland.
[37]Affiliated with an institute covered by a cooperation agreement with CERN.
[38]Affiliated with an international laboratory covered by a cooperation agreement with CERN.
[39]Enrico Fermi Institute, University of Chicago, Chicago IL; United States of America.
[40]LPC, Université Clermont Auvergne, CNRS/IN2P3, Clermont-Ferrand; France.
[41]Nevis Laboratory, Columbia University, Irvington NY; United States of America.

[42]Niels Bohr Institute, University of Copenhagen, Copenhagen; Denmark.
[43(a)]Dipartimento di Fisica, Università della Calabria, Rende;[(b)]INFN Gruppo Collegato di Cosenza, Laboratori Nazionali di Frascati; Italy.
[44]Physics Department, Southern Methodist University, Dallas TX; United States of America.
[45]Physics Department, University of Texas at Dallas, Richardson TX; United States of America.
[46]National Centre for Scientific Research "Demokritos", Agia Paraskevi; Greece.
[47(a)]Department of Physics, Stockholm University;[(b)]Oskar Klein Centre, Stockholm; Sweden.
[48]Deutsches Elektronen-Synchrotron DESY, Hamburg and Zeuthen; Germany.
[49]Fakultät Physik , Technische Universität Dortmund, Dortmund; Germany.
[50]Institut für Kern- und Teilchenphysik, Technische Universität Dresden, Dresden; Germany.
[51]Department of Physics, Duke University, Durham NC; United States of America.
[52]SUPA - School of Physics and Astronomy, University of Edinburgh, Edinburgh; United Kingdom.
[53]INFN e Laboratori Nazionali di Frascati, Frascati; Italy.
[54]Physikalisches Institut, Albert-Ludwigs-Universität Freiburg, Freiburg; Germany.
[55]II. Physikalisches Institut, Georg-August-Universität Göttingen, Göttingen; Germany.
[56]Département de Physique Nucléaire et Corpusculaire, Université de Genève, Genève; Switzerland.
[57(a)]Dipartimento di Fisica, Università di Genova, Genova;[(b)]INFN Sezione di Genova; Italy.
[58]II. Physikalisches Institut, Justus-Liebig-Universität Giessen, Giessen; Germany.
[59]SUPA - School of Physics and Astronomy, University of Glasgow, Glasgow; United Kingdom.
[60]LPSC, Université Grenoble Alpes, CNRS/IN2P3, Grenoble INP, Grenoble; France.
[61]Laboratory for Particle Physics and Cosmology, Harvard University, Cambridge MA; United States of America.
[62(a)]Department of Modern Physics and State Key Laboratory of Particle Detection and Electronics, University of Science and Technology of China, Hefei;[(b)]Institute of Frontier and Interdisciplinary Science and Key Laboratory of Particle Physics and Particle Irradiation (MOE), Shandong University, Qingdao;[(c)]School of Physics and Astronomy, Shanghai Jiao Tong University, Key Laboratory for Particle Astrophysics and Cosmology (MOE), SKLPPC, Shanghai;[(d)]Tsung-Dao Lee Institute, Shanghai;[(e)]School of Physics and Microelectronics, Zhengzhou University; China.
[63(a)]Kirchhoff-Institut für Physik, Ruprecht-Karls-Universität Heidelberg, Heidelberg;[(b)]Physikalisches Institut, Ruprecht-Karls-Universität Heidelberg, Heidelberg; Germany.
[64(a)]Department of Physics, Chinese University of Hong Kong, Shatin, N.T., Hong Kong;[(b)]Department of Physics, University of Hong Kong, Hong Kong;[(c)]Department of Physics and Institute for Advanced Study, Hong Kong University of Science and Technology, Clear Water Bay, Kowloon, Hong Kong; China.
[65]Department of Physics, National Tsing Hua University, Hsinchu; Taiwan.
[66]IJCLab, Université Paris-Saclay, CNRS/IN2P3, 91405, Orsay; France.
[67]Centro Nacional de Microelectrónica (IMB-CNM-CSIC), Barcelona; Spain.
[68]Department of Physics, Indiana University, Bloomington IN; United States of America.
[69(a)]INFN Gruppo Collegato di Udine, Sezione di Trieste, Udine;[(b)]ICTP, Trieste;[(c)]Dipartimento Politecnico di Ingegneria e Architettura, Università di Udine, Udine; Italy.
[70(a)]INFN Sezione di Lecce;[(b)]Dipartimento di Matematica e Fisica, Università del Salento, Lecce; Italy.
[71(a)]INFN Sezione di Milano;[(b)]Dipartimento di Fisica, Università di Milano, Milano; Italy.
[72(a)]INFN Sezione di Napoli;[(b)]Dipartimento di Fisica, Università di Napoli, Napoli; Italy.
[73(a)]INFN Sezione di Pavia;[(b)]Dipartimento di Fisica, Università di Pavia, Pavia; Italy.
[74(a)]INFN Sezione di Pisa;[(b)]Dipartimento di Fisica E. Fermi, Università di Pisa, Pisa; Italy.
[75(a)]INFN Sezione di Roma;[(b)]Dipartimento di Fisica, Sapienza Università di Roma, Roma; Italy.
[76(a)]INFN Sezione di Roma Tor Vergata;[(b)]Dipartimento di Fisica, Università di Roma Tor Vergata, Roma; Italy.

[77](a)INFN Sezione di Roma Tre;(b)Dipartimento di Matematica e Fisica, Università Roma Tre, Roma; Italy.
[78](a)INFN-TIFPA;(b)Università degli Studi di Trento, Trento; Italy.
[79]Universität Innsbruck, Department of Astro and Particle Physics, Innsbruck; Austria.
[80]University of Iowa, Iowa City IA; United States of America.
[81]Department of Physics and Astronomy, Iowa State University, Ames IA; United States of America.
[82]Istinye University, Sariyer, Istanbul; Türkiye.
[83](a)Departamento de Engenharia Elétrica, Universidade Federal de Juiz de Fora (UFJF), Juiz de Fora;(b)Universidade Federal do Rio De Janeiro COPPE/EE/IF, Rio de Janeiro;(c)Instituto de Física, Universidade de São Paulo, São Paulo;(d)Rio de Janeiro State University, Rio de Janeiro; Brazil.
[84]KEK, High Energy Accelerator Research Organization, Tsukuba; Japan.
[85]Graduate School of Science, Kobe University, Kobe; Japan.
[86](a)AGH University of Krakow, Faculty of Physics and Applied Computer Science, Krakow;(b)Marian Smoluchowski Institute of Physics, Jagiellonian University, Krakow; Poland.
[87]Institute of Nuclear Physics Polish Academy of Sciences, Krakow; Poland.
[88]Faculty of Science, Kyoto University, Kyoto; Japan.
[89]Research Center for Advanced Particle Physics and Department of Physics, Kyushu University, Fukuoka ; Japan.
[90]Instituto de Física La Plata, Universidad Nacional de La Plata and CONICET, La Plata; Argentina.
[91]Physics Department, Lancaster University, Lancaster; United Kingdom.
[92]Oliver Lodge Laboratory, University of Liverpool, Liverpool; United Kingdom.
[93]Department of Experimental Particle Physics, Jožef Stefan Institute and Department of Physics, University of Ljubljana, Ljubljana; Slovenia.
[94]School of Physics and Astronomy, Queen Mary University of London, London; United Kingdom.
[95]Department of Physics, Royal Holloway University of London, Egham; United Kingdom.
[96]Department of Physics and Astronomy, University College London, London; United Kingdom.
[97]Louisiana Tech University, Ruston LA; United States of America.
[98]Fysiska institutionen, Lunds universitet, Lund; Sweden.
[99]Departamento de Física Teorica C-15 and CIAFF, Universidad Autónoma de Madrid, Madrid; Spain.
[100]Institut für Physik, Universität Mainz, Mainz; Germany.
[101]School of Physics and Astronomy, University of Manchester, Manchester; United Kingdom.
[102]CPPM, Aix-Marseille Université, CNRS/IN2P3, Marseille; France.
[103]Department of Physics, University of Massachusetts, Amherst MA; United States of America.
[104]Department of Physics, McGill University, Montreal QC; Canada.
[105]School of Physics, University of Melbourne, Victoria; Australia.
[106]Department of Physics, University of Michigan, Ann Arbor MI; United States of America.
[107]Department of Physics and Astronomy, Michigan State University, East Lansing MI; United States of America.
[108]Group of Particle Physics, University of Montreal, Montreal QC; Canada.
[109]Fakultät für Physik, Ludwig-Maximilians-Universität München, München; Germany.
[110]Max-Planck-Institut für Physik (Werner-Heisenberg-Institut), München; Germany.
[111]Graduate School of Science and Kobayashi-Maskawa Institute, Nagoya University, Nagoya; Japan.
[112]Department of Physics and Astronomy, University of New Mexico, Albuquerque NM; United States of America.
[113]Institute for Mathematics, Astrophysics and Particle Physics, Radboud University/Nikhef, Nijmegen; Netherlands.
[114]Nikhef National Institute for Subatomic Physics and University of Amsterdam, Amsterdam;

Netherlands.
[115]Department of Physics, Northern Illinois University, DeKalb IL; United States of America.
[116(a)]New York University Abu Dhabi, Abu Dhabi;[(b)]United Arab Emirates University, Al Ain; United Arab Emirates.
[117]Department of Physics, New York University, New York NY; United States of America.
[118]Ochanomizu University, Otsuka, Bunkyo-ku, Tokyo; Japan.
[119]Ohio State University, Columbus OH; United States of America.
[120]Homer L. Dodge Department of Physics and Astronomy, University of Oklahoma, Norman OK; United States of America.
[121]Department of Physics, Oklahoma State University, Stillwater OK; United States of America.
[122]Palacký University, Joint Laboratory of Optics, Olomouc; Czech Republic.
[123]Institute for Fundamental Science, University of Oregon, Eugene, OR; United States of America.
[124]Graduate School of Science, Osaka University, Osaka; Japan.
[125]Department of Physics, University of Oslo, Oslo; Norway.
[126]Department of Physics, Oxford University, Oxford; United Kingdom.
[127]LPNHE, Sorbonne Université, Université Paris Cité, CNRS/IN2P3, Paris; France.
[128]Department of Physics, University of Pennsylvania, Philadelphia PA; United States of America.
[129]Department of Physics and Astronomy, University of Pittsburgh, Pittsburgh PA; United States of America.
[130(a)]Laboratório de Instrumentação e Física Experimental de Partículas - LIP, Lisboa;[(b)]Departamento de Física, Faculdade de Ciências, Universidade de Lisboa, Lisboa;[(c)]Departamento de Física, Universidade de Coimbra, Coimbra;[(d)]Centro de Física Nuclear da Universidade de Lisboa, Lisboa;[(e)]Departamento de Física, Universidade do Minho, Braga;[(f)]Departamento de Física Teórica y del Cosmos, Universidad de Granada, Granada (Spain);[(g)]Departamento de Física, Instituto Superior Técnico, Universidade de Lisboa, Lisboa; Portugal.
[131]Institute of Physics of the Czech Academy of Sciences, Prague; Czech Republic.
[132]Czech Technical University in Prague, Prague; Czech Republic.
[133]Charles University, Faculty of Mathematics and Physics, Prague; Czech Republic.
[134]Particle Physics Department, Rutherford Appleton Laboratory, Didcot; United Kingdom.
[135]IRFU, CEA, Université Paris-Saclay, Gif-sur-Yvette; France.
[136]Santa Cruz Institute for Particle Physics, University of California Santa Cruz, Santa Cruz CA; United States of America.
[137(a)]Departamento de Física, Pontificia Universidad Católica de Chile, Santiago;[(b)]Millennium Institute for Subatomic physics at high energy frontier (SAPHIR), Santiago;[(c)]Instituto de Investigación Multidisciplinario en Ciencia y Tecnología, y Departamento de Física, Universidad de La Serena;[(d)]Universidad Andres Bello, Department of Physics, Santiago;[(e)]Instituto de Alta Investigación, Universidad de Tarapacá, Arica;[(f)]Departamento de Física, Universidad Técnica Federico Santa María, Valparaíso; Chile.
[138]Department of Physics, University of Washington, Seattle WA; United States of America.
[139]Department of Physics and Astronomy, University of Sheffield, Sheffield; United Kingdom.
[140]Department of Physics, Shinshu University, Nagano; Japan.
[141]Department Physik, Universität Siegen, Siegen; Germany.
[142]Department of Physics, Simon Fraser University, Burnaby BC; Canada.
[143]SLAC National Accelerator Laboratory, Stanford CA; United States of America.
[144]Department of Physics, Royal Institute of Technology, Stockholm; Sweden.
[145]Departments of Physics and Astronomy, Stony Brook University, Stony Brook NY; United States of America.

[146]Department of Physics and Astronomy, University of Sussex, Brighton; United Kingdom.
[147]School of Physics, University of Sydney, Sydney; Australia.
[148]Institute of Physics, Academia Sinica, Taipei; Taiwan.
[149(a)]E. Andronikashvili Institute of Physics, Iv. Javakhishvili Tbilisi State University, Tbilisi;[(b)]High Energy Physics Institute, Tbilisi State University, Tbilisi;[(c)]University of Georgia, Tbilisi; Georgia.
[150]Department of Physics, Technion, Israel Institute of Technology, Haifa; Israel.
[151]Raymond and Beverly Sackler School of Physics and Astronomy, Tel Aviv University, Tel Aviv; Israel.
[152]Department of Physics, Aristotle University of Thessaloniki, Thessaloniki; Greece.
[153]International Center for Elementary Particle Physics and Department of Physics, University of Tokyo, Tokyo; Japan.
[154]Department of Physics, Tokyo Institute of Technology, Tokyo; Japan.
[155]Department of Physics, University of Toronto, Toronto ON; Canada.
[156(a)]TRIUMF, Vancouver BC;[(b)]Department of Physics and Astronomy, York University, Toronto ON; Canada.
[157]Division of Physics and Tomonaga Center for the History of the Universe, Faculty of Pure and Applied Sciences, University of Tsukuba, Tsukuba; Japan.
[158]Department of Physics and Astronomy, Tufts University, Medford MA; United States of America.
[159]Department of Physics and Astronomy, University of California Irvine, Irvine CA; United States of America.
[160]University of Sharjah, Sharjah; United Arab Emirates.
[161]Department of Physics and Astronomy, University of Uppsala, Uppsala; Sweden.
[162]Department of Physics, University of Illinois, Urbana IL; United States of America.
[163]Instituto de Física Corpuscular (IFIC), Centro Mixto Universidad de Valencia - CSIC, Valencia; Spain.
[164]Department of Physics, University of British Columbia, Vancouver BC; Canada.
[165]Department of Physics and Astronomy, University of Victoria, Victoria BC; Canada.
[166]Fakultät für Physik und Astronomie, Julius-Maximilians-Universität Würzburg, Würzburg; Germany.
[167]Department of Physics, University of Warwick, Coventry; United Kingdom.
[168]Waseda University, Tokyo; Japan.
[169]Department of Particle Physics and Astrophysics, Weizmann Institute of Science, Rehovot; Israel.
[170]Department of Physics, University of Wisconsin, Madison WI; United States of America.
[171]Fakultät für Mathematik und Naturwissenschaften, Fachgruppe Physik, Bergische Universität Wuppertal, Wuppertal; Germany.
[172]Department of Physics, Yale University, New Haven CT; United States of America.
[a] Also Affiliated with an institute covered by a cooperation agreement with CERN.
[b] Also at An-Najah National University, Nablus; Palestine.
[c] Also at Borough of Manhattan Community College, City University of New York, New York NY; United States of America.
[d] Also at Center for High Energy Physics, Peking University; China.
[e] Also at Center for Interdisciplinary Research and Innovation (CIRI-AUTH), Thessaloniki; Greece.
[f] Also at Centro Studi e Ricerche Enrico Fermi; Italy.
[g] Also at CERN, Geneva; Switzerland.
[h] Also at Département de Physique Nucléaire et Corpusculaire, Université de Genève, Genève; Switzerland.
[i] Also at Departament de Fisica de la Universitat Autonoma de Barcelona, Barcelona; Spain.
[j] Also at Department of Financial and Management Engineering, University of the Aegean, Chios; Greece.
[k] Also at Department of Physics, Ben Gurion University of the Negev, Beer Sheva; Israel.
[l] Also at Department of Physics, California State University, Sacramento; United States of America.

[m] Also at Department of Physics, King's College London, London; United Kingdom.
[n] Also at Department of Physics, Stanford University, Stanford CA; United States of America.
[o] Also at Department of Physics, Stellenbosch University; South Africa.
[p] Also at Department of Physics, University of Fribourg, Fribourg; Switzerland.
[q] Also at Department of Physics, University of Thessaly; Greece.
[r] Also at Department of Physics, Westmont College, Santa Barbara; United States of America.
[s] Also at Hellenic Open University, Patras; Greece.
[t] Also at Institucio Catalana de Recerca i Estudis Avancats, ICREA, Barcelona; Spain.
[u] Also at Institut für Experimentalphysik, Universität Hamburg, Hamburg; Germany.
[v] Also at Institute for Nuclear Research and Nuclear Energy (INRNE) of the Bulgarian Academy of Sciences, Sofia; Bulgaria.
[w] Also at Institute of Applied Physics, Mohammed VI Polytechnic University, Ben Guerir; Morocco.
[x] Also at Institute of Particle Physics (IPP); Canada.
[y] Also at Institute of Physics and Technology, Ulaanbaatar; Mongolia.
[z] Also at Institute of Physics, Azerbaijan Academy of Sciences, Baku; Azerbaijan.
[aa] Also at Institute of Theoretical Physics, Ilia State University, Tbilisi; Georgia.
[ab] Also at L2IT, Université de Toulouse, CNRS/IN2P3, UPS, Toulouse; France.
[ac] Also at Lawrence Livermore National Laboratory, Livermore; United States of America.
[ad] Also at National Institute of Physics, University of the Philippines Diliman (Philippines); Philippines.
[ae] Also at Technical University of Munich, Munich; Germany.
[af] Also at The Collaborative Innovation Center of Quantum Matter (CICQM), Beijing; China.
[ag] Also at TRIUMF, Vancouver BC; Canada.
[ah] Also at Università di Napoli Parthenope, Napoli; Italy.
[ai] Also at University of Chinese Academy of Sciences (UCAS), Beijing; China.
[aj] Also at University of Colorado Boulder, Department of Physics, Colorado; United States of America.
[ak] Also at Washington College, Chestertown, MD; United States of America.
[al] Also at Yeditepe University, Physics Department, Istanbul; Türkiye.
[*] Deceased